Optical Data Analysis and its Application to Cosmology

Dissertation
zur
Erlangung des Doktorgrades (Dr. rer. nat.)
der
Mathematisch-Naturwissenschaftlichen Fakultät
der
Rheinischen Friedrich-Wilhelms-Universität Bonn

vorgelegt von

Axel Buddendiek

aus
Lahnstein

Bonn, 2015

Angefertigt mit Genehmigung der Mathematisch-Naturwissenschaftlichen Fakultät der Rheinischen Friedrich-Wilhelms-Universität Bonn

1. Gutachter: Prof. Dr. Peter Schneider
2. Gutachter: Prof. Dr. Thomas Reiprich

Tag der Promotion: 11.03.2016
Erscheinungsjahr: 2016

Contents

Preface

Astronomy is the oldest science and it has survived over the ages, because there is always more to discover. Especially the fields of extragalactic astronomy and cosmology combine many disciplines of modern physics and are thus very attractive and active fields of research. Cosmology is the science of the Universe as a whole, where scientists are trying to understand how the Universe evolves, how it started, and what it is made of. Although people have been trying to find out what the Universe is made of, it appears that we still only know about 5 per cent of its content, namely baryonic matter, which for example men are made of. The rest of the Universe is filled with the mysterious and invisible substances of dark matter and dark energy. Dark matter makes up most of the mass in galaxies and clusters of galaxies and is suspected to be a still unknown elementary particle, whereas dark energy appears to accelerate the expansion of the Universe and it is not clear at all what it might be. In order to map the dark matter distribution and investigate the true nature of dark energy, we need to observe the sky using high-tech telescopes and cameras. The raw data products, which derive from such a telescope, are not immediately usable for science. They need to undergo a long process of data reduction and manipulation. The analysis itself is then another complicated, long process during which we build theories and use various statistical methods to test and constrain them.

The title of this thesis, "Optical Data Analysis and its Application to Cosmology", and its meaning are starting to become clear. In order to understand the Universe we need observations of the sky and we need to find suitable methods to analyse them. In this thesis we will focus on observations in the optical. After introducing the basic theoretical concepts of astronomy and cosmology in the Chapters 1, 2, and 3, which we will need to understand this thesis, we will describe various aspects of optical data analysis and its applications in the subsequent chapters. A very technical aspect of astronomy is described in Chapter 4, where we introduce the problem of CCD crosstalk, a problem present in many modern CCD cameras, and a correction for it for the specific example of OmegaCAM. In Chapter 5, which is based on a publication in *Monthly Notices of the Royal Astronomical Society*, we will learn about how archival data can be used to discover new massive galaxy clusters. Furthermore, we describe the process of the analysis of optical imaging and spectroscopic data in order to learn about specific properties of these clusters. Finally, we will combine the optical data with radio data and conduct a cosmology test to find out if the clusters found are in tension with the cosmological standard model. In Chapter 6 we will introduce a new estimator for two-point statistics, an important tool in modern cosmology, and apply it to data from the BOSS and the RCSLenS surveys in order to measure the galaxy bias b. This is an approach that is also promising for cosmological studies.

In the end, this thesis is concerned with three major aspects of modern observational cosmology: technical work, data analysis, and its interpretation. We hope that after reading this thesis the reader will have gained some more insight into the complicated field of cosmology.

CHAPTER 1

Cosmology

This chapter is in great parts based on the following references:

- *Carrol (2004)*
- *Dodelson (2003)*
- *Serjeant (2010)*
- *Mo, van den Bosch & White (2010)*
- *Schneider (2009)*

1.1. Theory of General Relativity

In this section and and Section 1.2 we will make use of natural units where the speed of light is $c = 1$.

The dominant force on large scales in our Universe is gravity, the phenomenon that massive bodies appear to attract each other. For centuries mankind attempted to find a theoretical description for gravity, a way to describe it. The first one to find a proper description was Sir Isaac Newton who in his "Principia Mathematica" first formulated a gravitational law

$$\vec{F_g} = G m_1 m_2 \frac{\vec{r}}{|r|^3} , \tag{1.1}$$

where G is the gravitational constant, m_1 and m_2 the masses of the two bodies and $\vec{r}$ the separation vector between those bodies. This proved adequate to describe most, but not all, of the motions of the planets in the solar system. There were still some small discrepancies between predictions and observations, like the precession of Mercury's perihelion. To explain this, it needed another more advanced theory of gravity, which is Einstein's theory of general relativity. In his theory, Einstein explains gravity not as an attraction of masses but rather as the curvature of space-time. Consequently, the Einstein equation connects the energy content of space-time with the curvature

$$G_{\mu\nu} = R_{\mu\nu} - \frac{1}{2} g_{\mu\nu} R = -8\pi G T_{\mu\nu} \ . \tag{1.2}$$

Here $G_{\mu\nu}$ is the Einstein tensor, which describes the curvature of space-time. It consists of $R_{\mu\nu}$, the Ricci tensor, and R its contraction, the Ricci scalar. Those are derived from derivatives of the metric $g_{\mu\nu}$. $T_{\mu\nu}$ is the energy momentum tensor, which gives the energy-momentum of space-time.

Given a metric that solves Eq. (1.2), we can immediately compute the left hand side of that equation. Since $G_{\mu\nu}$ and $T_{\mu\nu}$ only differ by a constant, this then also gives us the shape of the energy-momentum tensor.

1.2. Friedmann-Robertson-Walker Models

In order to find solutions to Eq. (1.2), namely the metric $g_{\mu\nu}$, one usually has to make some simplifying assumptions. One of the first solutions found was the Friedmann-Robertson-Walker metric, which derives from the cosmological principle:

1. The Universe is homogeneous.
2. The Universe is isotropic.

Homogeneous means that a small part of something is a fair representation of the whole and isotropic that something looks the same in all directions. The Friedmann-Robertson-Walker metric is thus the most homogeneous and isotropic solution to Einstein's equation

$$\mathrm{d}s^2 = \mathrm{d}t^2 - a^2(t) \left[\mathrm{d}w^2 + f_k^2(w)(\mathrm{d}\theta^2 + \sin^2(\theta)\mathrm{d}\phi^2\right] \ . \tag{1.3}$$

Here w is the comoving distance, θ and ϕ are spherical coordinates, $f_k(w)$ the comoving angular diameter distance, and k the curvature parameter. We find that $f_k(w)$ depends on k

$$f_k(w) = \begin{cases} \frac{1}{\sqrt{-k}} \sinh\left(\sqrt{-k}\, w\right) & k < 0\,, \\ w & k = 0\,, \\ \frac{1}{\sqrt{k}} \sin\left(\sqrt{k}\, w\right) & k > 0\,. \end{cases} \tag{1.4}$$

Furthermore, $\mathrm{d}s^2$ is the space-time interval; in case of light rays, this becomes zero and $a(t)$ is the so-called scale factor, which describes the expansion behaviour of the Universe. A static isotropic and homogeneous universe is not stable, which is why all Friedmann-Robertson-Walker models are non-static ones.

For this metric we can immediately compute the left hand side of Eq. (1.2), since the Ricci tensor $R_{\mu\nu}$ and the Ricci scalar R are derivatives of the metric. Given the Einstein tensor, $G_{\mu\nu}$, we then find that the Universe is filled with a perfect fluid and thus use the corresponding energy momentum tensor

$$T_{\mu\nu} = (\rho + p)U_\mu U_\nu + p g_{\mu\nu} \ , \tag{1.5}$$

where ρ is the density, p the pressure, and $U_\mu = (1, 0, 0, 0)$ the four velocity. The time-time component of Eq. (1.2) then yields the following equation

$$\left(\frac{\dot{a}(t)}{a(t)}\right)^2 = \frac{8\pi G}{3}\rho(t) - \frac{k}{a^2(t)} \ , \tag{1.6}$$

which is known as the first Friedmann equation. Due to the isotropy in the Friedmann-Robertson-Walker solution the spatial part yields only one equation

$$\frac{\ddot{a}(t)}{a(t)} = -\frac{4\pi G}{3}\left[3p(t) + \rho(t)\right] \ . \tag{1.7}$$

This is the second Friedmann equation. Those two equations describe the evolution of the expansion factor $a(t)$ of the Universe. Both can also be illustratively derived from Newtonian physics, as we will see now. With this derivation we will follow the one shown in Schneider (2006) closely. We start by considering an expanding sphere with physical radius $R_\mathrm{s}(t) = a(t)r_\mathrm{s}$, where we introduced the comoving radius r_s, which is unaffected by the expansion, and the scale factor $a(t)$ that describes the expansion of the sphere. The density of the sphere is given as $\rho(t) = \rho_0 a^{-3}(t)$ and the mass of the sphere is then

$$M(r_\mathrm{s}) = \frac{4\pi}{3}\rho_0 r_\mathrm{s}^3 \ . \tag{1.8}$$

We can write down the equation of motion for this system

$$\ddot{R}_\mathrm{s}(t) = -\frac{GM(r_\mathrm{s})}{R_\mathrm{s}^2(t)} = -\frac{4\pi G}{3}\frac{\rho_0 r_\mathrm{s}^3}{R_\mathrm{s}^2(t)} \ , \tag{1.9}$$

which yields

$$\ddot{a}(t) = -\frac{4\pi G}{3}\rho(t)a(t) \ . \tag{1.10}$$

Then we divide by $a(t)$ and arrive at the second Friedmann equation,

$$\frac{\ddot{a}(t)}{a(t)} = -\frac{4\pi G}{3}\rho(t) \ . \tag{1.11}$$

This only differs from Eq. (1.7) in one aspect, which is the missing pressure term. In the Newtonian approach we only consider matter, which can be assumed to be pressure free. Finally, we can now multiply this equation with $2\dot{a}a$, which leaves us with

$$2\dot{a}(t)\ddot{a}(t) = -\frac{8\pi G}{3}\rho_0\frac{\dot{a}(t)}{a^2(t)} \ . \tag{1.12}$$

It is known that $\frac{\mathrm{d}}{\mathrm{d}t}\dot{a}^2 = 2\ddot{a}\dot{a}$ and that $\frac{\mathrm{d}}{\mathrm{d}t}\left(-\frac{1}{a}\right) = \frac{\dot{a}}{a^2}$, which we can plug into Eq. (1.12) and then integrate it. This then yields

$$\left(\frac{\dot{a}(t)}{a(t)}\right)^2 = \frac{8\pi G}{3}\rho(t) - \frac{k}{a^2(t)} \ , \tag{1.13}$$

where k is an integration constant. This remarkably resembles the correct full relativistic derivation of Eq. (1.6).

If we now consider the first Friedmann equation again, we can distinguish between three different spatial curvatures of a universe, depending on the sign of the curvature parameter k. In case of $k < 0$ the universe is open. For $k > 0$ the universe is closed, whereas $k = 0$ is the limiting case, called a flat universe. Assuming $k = 0$ for Eq. (1.6) we can define the critical density, which is needed for a flat universe

$$\rho_{\mathrm{crit}}(t) = \frac{3H^2(t)}{8\pi G} \ , \tag{1.14}$$

where we defined $H(t) = \frac{\dot{a}(t)}{a(t)}$ as the expansion rate or the so-called Hubble parameter. Using the critical density ρ_{crit} we can define dimensionless density parameters to describe the energy content of the Universe. For this we use ρ_{crit} at our time now, t_0, which just leads to $H(t) \to H(t_0) = H_0$, the current expansion rate of the Universe, or the so-called Hubble constant. This is sometimes parametrised as $H_0 = h \times 100\,\mathrm{km\,s^{-1}\,Mpc^{-1}}$, where h is the dimensionless Hubble constant. From observations we know that our Universe is filled with matter, radiation, and the so-called dark energy

$$\frac{\rho_{\mathrm{m}}(t)}{\rho_{\mathrm{crit}}(t)} = \Omega_{\mathrm{m}}(t), \qquad \frac{\rho_{\mathrm{r}}(t)}{\rho_{\mathrm{crit}}(t)} = \Omega_{\mathrm{r}}(t), \qquad \frac{\rho_{\Lambda}(t)}{\rho_{\mathrm{crit}}(t)} = \Omega_{\Lambda}(t) \ . \tag{1.15}$$

Due to the expansion of the Universe, the energy densities in general are not constant but change with time. The matter density changes with a^{-3} due to the expansion of the three spatial dimensions. The radiation density also gets diluted by the spatial expansion and additionally, the wavelength of the radiation expands, which results in an extra factor of a, so in total it scales with a^{-4}. The dark energy density is assumed to be constant over time, which means it scales with a^0. When plugging in the definition of the critical density we find, for example in case of the matter density

$$\Omega_{\mathrm{m}}(t) = \frac{\rho_{\mathrm{m}}(t)}{\rho_{\mathrm{crit}}(t)} = \frac{8\pi G}{3H^2(t)}\rho_{\mathrm{m}}(t) = \left(\frac{H_0}{H(t)}\right)^2 \Omega_{\mathrm{m},0}\, a^{-3}(t) \ . \tag{1.16}$$

Consequently, we write

$$\Omega_{\mathrm{r}}(t) = \left(\frac{H_0}{H(t)}\right)^2 \Omega_{\mathrm{r},0}\, a^{-4}(t), \qquad \Omega_{\Lambda}(t) = \left(\frac{H_0}{H(t)}\right)^2 \Omega_{\Lambda,0}\, a^{0}(t) \ . \tag{1.17}$$

So far we have excluded the curvature part of Eq. (1.6). We can replace k with the curvature parameter $\Omega_{\mathrm{k}} = 1 - \sum \Omega_i = 1 - \Omega_0$ as $k = -H_0^2\Omega_k$. Now we can also replace $\rho = \rho_{\mathrm{m}} + \rho_{\mathrm{r}} + \rho_{\Lambda}$

with the density parameters in the first Friedmann equation, which yields a slightly different notation

$$\left(\frac{\dot{a}}{a}\right)^2 = H^2 = H_0^2 \left[\Omega_{\mathrm{m},0}\, a^{-3} + \Omega_{\mathrm{r},0}\, a^{-4} + \Omega_{\Lambda,0}\, a^0 + (1-\Omega_0)\, a^{-2}\right] \ . \tag{1.18}$$

As we can see, the density parameters and the Hubble constant are sufficient to describe the expansion history of the Universe. Given those parameters, one can attempt to solve the first Friedmann equation, which will yield the functional form of the scale factor $a(t)$. In general the first Friedmann equation cannot be solved analytically. Nevertheless, by using simplifying assumptions we can find analytic solutions for it. In a universe with $\Omega_\mathrm{m} = \Omega_0 = 1$ we find $a(t) = \left(\frac{3}{2}H_0 t\right)^{2/3}$. This is called an Einstein-de-Sitter model. A dark energy-dominated universe where $\Omega_\Lambda = \Omega_0 = 1$ has a scale factor of $a(t) = e^{H_0 t}$. In a radiation dominated universe with $\Omega_\mathrm{r} = \Omega_0 = 1$ the Friedmann equation yields $a(t) = \sqrt{2H_0 t}$.

When considering how the radiation density scales with the cosmic scale factor, we already stated that the wavelength of radiation changes due to the expansion of the Universe. Since the wavelength becomes longer, light becomes redder and thus this effect is called the redshift z. In terms of observed and emitted wavelength we define it as follows

$$z = \frac{\lambda_\mathrm{obs} - \lambda_\mathrm{e}}{\lambda_\mathrm{e}} \ . \tag{1.19}$$

We know that $\lambda_\mathrm{e} = a(t_\mathrm{e})\lambda_\mathrm{obs}$, which then yields the relation between redshift z and scale factor a

$$a = \frac{1}{1+z} \ . \tag{1.20}$$

The redshift z is an actual observable, which, as we will see later on, is closely related to several measures of distance. It can be measured in the spectra of galaxies, where known spectroscopic features, like emission or absorption lines are found at wavelengths that are different from the known rest frame ones.

In the 1920's Edwin Hubble measured redshifts for many galaxies and found that the further away those galaxies were, the more redshifted their spectra were or the higher their recession velocity was. He formulated this observation mathematically in the Hubble law

$$v(t) = cz = H_0 r \ , \tag{1.21}$$

where v is the velocity of the galaxy and r its distance. We can also derive this law from the principles of an expanding universe. Again, we consider comoving coordinates $\vec{x} = \frac{\vec{r}(t)}{a(t)}$. From this we find the physical position $\vec{r}(t) = a(t)\vec{x}$ and its derivative

$$\vec{v}(t) = \dot{a}(t)\vec{x} = \frac{\dot{a}(t)}{a(t)}\vec{r}(t) = H(t)\vec{r}(t) \ , \tag{1.22}$$

where in the second step we plugged in the definition of the comoving coordinate again.

1.3. Cosmological Distances

Due to the expansion of the Universe, defining distances in cosmology is a difficult business. Thus, unlike in Euclidean space, there is not one distance definition but several, which are all connected with each other. The distance as we on earth would measure it, for example between the start and finish lines of some kind of race track, is what we call the proper distance d_p. This corresponds to stopping time and using a ruler to find the distance between us and a galaxy, which, of course, is not feasible or better to say impossible. The proper distance is, as we have seen already, closely related to the comoving distance, which is by definition not affected by the expansion of the Universe

$$w = a(t) d_\mathrm{p}(t) \; . \tag{1.23}$$

Comoving and proper distance can be computed using a fixed cosmology and a measured redshift. Apart from the redshift being the observable one can also construct distances, which are connected to different measurements. One such distance is the angular diameter distance. Given the angular size θ and the proper size s of an object one can define the angular diameter distance as

$$d_\mathrm{A} = \frac{s}{\theta} \; . \tag{1.24}$$

A similar approach is to make use of the luminosity and the flux of an object, which results in the luminosity distance

$$d_\mathrm{L} = \sqrt{\frac{L}{4\pi S}} \; . \tag{1.25}$$

Comoving distance, angular diameter distance and luminosity distance are all connected via the redshift or the scale factor

$$d_\mathrm{L} = a^{-2} d_\mathrm{A} = a^{-1} w \; , \tag{1.26}$$

where the last equality is only valid in a flat universe. From Eq. (1.3) follows

$$w = \int_{t(a)}^{t_0} \mathrm{d}t' \frac{c}{a(t')} = \int_a^1 \mathrm{d}a' \frac{c}{a'^2 H(a')} \; . \tag{1.27}$$

In a similar way we can also give the angular diameter distance as a function of the scale factor. Starting with the definition above, for a flat universe we find

$$d_\mathrm{A} = a w \; , \tag{1.28}$$

because in an expanding universe the comoving size is s/a and the angular size is $\frac{s/a}{w(a)}$. For open and closed universes we find

$$d_\mathrm{A} = \begin{cases} \frac{a}{H_0 \sqrt{\Omega_\mathrm{k}}} \sinh\left(\sqrt{\Omega_\mathrm{k}} H_0 w\right) & \Omega_\mathrm{k} > 0 \, , \\ \frac{a}{H_0 \sqrt{|\Omega_\mathrm{k}|}} \sin\left(\sqrt{|\Omega_\mathrm{k}|} H_0 w\right) & \Omega_\mathrm{k} < 0 \, . \end{cases} \tag{1.29}$$

1.4. Thermal History of the Universe

In the middle of the 20th century, astronomers discovered that in every direction on the sky one can measure a background radiation in the microwave regime. Today it is known as the cosmic microwave background (CMB). This radiation is the same in all directions and follows a Planck distribution with a maximum temperature of $T_{\mathrm{CMB}} \approx 2.7\,\mathrm{K}$. In this section we will give a brief history of the Universe starting shortly after the big bang and explain how the CMB was created and why it is important for cosmology today.

Energies can be expressed in terms of the temperature T and Boltzmann's constant k_{B}. We can insert this into the relation between the wavelength λ and the energy E

$$\lambda = \frac{hc}{E} = \frac{hc}{k_{\mathrm{B}}T} \, , \tag{1.30}$$

where h is the Planck constant. This means that, using the temperature of the CMB, we can find the characteristic wavelength of the CMB photons today

$$\lambda_{\mathrm{CMB}} = \frac{hc}{k_{\mathrm{B}}T_{\mathrm{CMB}}} \, . \tag{1.31}$$

Due to the expansion of the Universe the CMB photons get redshifted by a factor of a^{-1}, which also means that their temperature decreased over time. Considering this, it means that the Universe started in a hot and dense state and due to its expansion it cooled down. This hot and dense state in the beginning is called the big bang. Shortly after the big bang the Universe was also very different than it is now; it was filled with a primordial plasma.

Whether a particle species is in equilibrium with the rest of the plasma depends on the expansion rate $H(t)$ and the reaction rate, Γ, of the processes that produce and destroy those particles. Γ depends on the particle density, the reaction cross-section, and the velocity distribution. Since the density decreases with a^{-3} due to the expansion and the cross-sections decrease due to their dependence on the energy and thus the temperature, the reaction rate decreases as well. As long as $\Gamma > H(t)$ particles can still be created sufficiently and the number of particles stays in equilibrium. Knowing these things, we will now briefly go through the thermal history of the Universe. When considering how the density parameters change with the scale factor, we find that in the early Universe the radiation density must have been the dominating ingredient, whereas later on matter and then eventually dark energy will take over.

The very early stages of the Universe are not quite understood yet, because so far we do not know the physics to describe systems at such high energies. Nevertheless, at some point the Universe had cooled down sufficiently for us to be able to describe its further history. At this time the Universe was still too hot for atoms or even molecules to form. They were dissipated immediately by high energy photons. Thus, the plasma contained smaller building blocks of matter, like protons, neutrons, electrons, neutrinos, or photons. Depending on the rest mass and on the rate of the reactions through which they are created the particles will one after another stop being in equilibrium with the rest of the plasma, for reasons mentioned before. At a temperature of a few MeV we will start our description of the thermal history. At those energies, protons and neutrons are already too heavy to be created from photons, so they stayed in equilibrium with other particles through weak interactions, but we will get back to this later. Besides protons and neutrons this leaves photons, electrons, positrons, and neutrinos.

The mass of neutrinos is not yet known but from neutrino oscillations we know that neutrinos are not massless, although their mass must be low, $m_\nu \leq 1\,\mathrm{eV}$. Neutrinos stay in equilibrium via the reaction

$$e^- + e^+ \longleftrightarrow \nu_e + \bar{\nu}_e \ .$$

At a temperature of about $1.4\,\mathrm{MeV}$, the reaction rates for neutrino creation are smaller than $H(t)$ and thus they decouple from the plasma and do not interact with it any more.

Electrons and positrons have a rest mass of $m_e = 511\,\mathrm{keV}$. Consequently, they cannot be created through

$$\gamma + \gamma \longleftrightarrow e^- + e^+$$

reactions any more, when the temperature is smaller than m_e. Thus, at a temperature of about $0.5\,\mathrm{MeV}$, electrons and positrons can no longer be created through the aforementioned reaction but they can still annihilate and produce more photons. This leads to a temperature rise in the photon plasma, which does not affect the neutrinos, since they were already decoupled. One should note that there was a small excess in electrons compared to positrons, which was needed to counterbalance the proton charge. This excess of electrons could thus not be annihilated with positrons.

We already mentioned that protons and neutrons stay in equilibrium through weak interactions, also involving neutrinos. After the neutrino freeze out, those reactions happen only very rarely any more. Due to this and the fact that neutrons are a bit heavier than protons, neutrons start to decay after the neutrino freeze out via

$$n \rightarrow p + e^- + \bar{\nu_\mathrm{e}} \,.$$

We know that there are neutrons in the Universe today and this is because they got bound inside the first atomic nuclei before all of them could decay, which brings us to the era of big bang nucleosynthesis.

Between temperatures of $0.7\,\mathrm{MeV}$ and $0.1\,\mathrm{MeV}$, the Universe was sufficiently cool to not dissipate the first atomic nuclei, but still sufficiently hot and dense to form those. Basically all neutrons got captured in deuterium via

$$p + n \longleftrightarrow D + \gamma \,.$$

The deuterium then gets transformed to He^4. Besides that, also small quantities of He^3 and lithium could be built, but H and He^4 make up almost all of the atomic nuclei in the Universe at the end of big bang nucleosynthesis.

All events described before happened in the radiation dominated era, where the radiation density dominated the expansion compared to the smaller matter and possibly the dark energy density. Some time after big bang nucleosynthesis happened, the Universe had been expanding enough for matter to start being the dominant ingredient. At an energy of about 1eV most of the photons were not energetic enough to ionize hydrogen atoms, which formed out of one electron and one proton. This time is called recombination and happens at a much lower energy than the hydrogen binding energy of 13.6 eV, because of the high energy photons in the Wien tail of their velocity distribution.

Before recombination, the plasma in the Universe consisted of photons and baryons which interacted with each other through various interactions, for example Compton scattering. After recombination, no particle species can still interact with the primordial photons and thus they can travel freely through the Universe. We call this the cosmic microwave background which has been observed and which shows the Universe at the time of the last scattering between photons and matter. It is called microwave background because today we observe the red-shifted photons, which at the time of the last scattering had a much higher energy, in the microwave regime. The CMB indeed is the most perfect black body spectrum observed today with a temperature of $T_{\mathrm{CMB}} \approx 2.73\,\mathrm{K}$.

Now that recombination is over, the Universe is neutral and the primordial photons can travel freely without any interactions with matter. Today, though, we know that the Universe is ionized again as we can observe UV emission from high-redshift ($z > 6$) sources. In a neutral universe, these photons would have been absorbed by neutral hydrogen atoms. Accordingly, there must have been a period in time where the Universe became reionized, which is called the epoch of reionization. Why and when exactly this happened is not clear, yet. This is a very active field of research and so far it is only known that reionization happened between $z \approx 6$ and $z \approx 12$. The sources that are suspected to have reionized the neutral Universe are first stars and active galactic nuclei.

1.5. Cosmological Probes

As we have seen before, a few numbers, the so-called cosmological parameters, are sufficient to describe the evolution of our Universe on large scales, when using the Friedmann-Robertson-Walker metric. Those parameters are the density parameters Ω_i, the Hubble constant H_0 as well as some others, which we will come across later in this chapter. Those are all free parameters that need to be fixed by observations. In this section, we will briefly describe several cosmological probes and corresponding results.

1.5.1. Clusters of Galaxies

At the peaks of the dark matter density distribution we can find large ensembles of galaxies, which are gravitationally bound. This is what we call a cluster of galaxies. Within those, galaxies actually only contribute about one per cent to the total mass content. Most of the mass, roughly 90 per cent, is dark matter. The remaining is the so-called intra cluster medium (ICM), a hot gas, consisting mostly of hydrogen and helium.

Galaxy clusters play an important role in cosmology, which is why we will refer for more detail to Chapter 3 and for an actual application to Chapter 5.

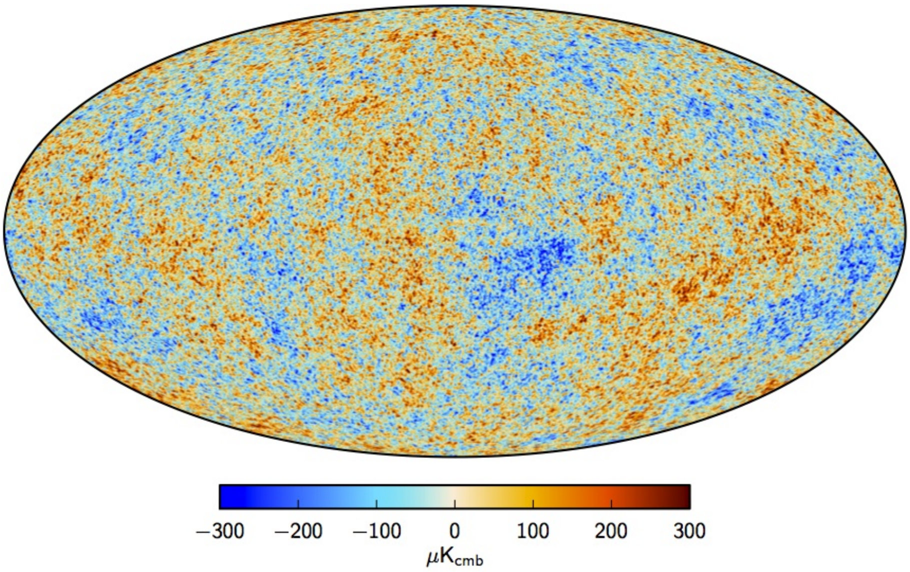

Figure 1.1.: The CMB temperature differences compared to the mean temperature as seen by *Planck* (Planck Collaboration et al., 2015a). Note that the contrast is chosen in order for the small anisotropies to be visible.

1.5.2. The Cosmic Microwave Background

As we will see later on, something called inflation is probably the origin for the structures that were imprinted on the density distribution in the early Universe, which was supposed to be homogeneous and isotropic. Those structures then result in the large scale inhomogeneities that we observe today, like galaxies, galaxy clusters, and voids. Before recombination, those over- and underdensities could only grow in the dark matter density field. Dark matter is not coupled to photons, which wiped out all baryonic structures. Still, due to dark matter there were over- and underdense regions in the Universe and because of gravity the primordial plasma would fall into those overdense regions and contract. Due to the contraction, the photon pressure would rise, which then pushed the plasma out of the potential wells again. This process would then repeat itself and it is what is called baryonic acoustic oscillations (BAO). We call them acoustic oscillations, because those appeared as pressure waves in the primordial plasma. At recombination, the CMB photons start to travel freely and all of them are supposed to have the same energy or wavelength, but due to the over- and underdense regions, some photons are hotter or colder. This is then what can be observed as the CMB, the temperature of the sky in every direction. After subtracting foreground sources, the CMB then indeed looks almost the same regardless of the direction - almost, but not quite. There are temperature differences of the order of 10^{-5} K, which are caused by the aforementioned inhomogeneities in the early Universe. A full sky map of the CMB measured by the *Planck* satellite is displayed in Fig. 1.1.

CMB experiments create temperature maps of the sky by measuring the energy of incoming photons in different directions. From these maps one can then compute the temperature distribution, which follows a black body spectrum and the temperature power spectrum, which tells us about characteristic scales in the temperature differences on the sky. In the temperature power spectrum shown in Fig. 1.2 one can observe peaks in the amplitude of the data points. Those correspond to different modes of the BAO before recombination. The first peak is caused by the mode that until recombination was able to only fall into the wells and then rarefy once. The scale on which this peak appears corresponds to the distance a sound wave could have travelled between the big bang and recombination, the sound horizon. All other peaks are caused by modes which were able to contract and rarefy more often. The location and the ratio of the peak amplitudes are sensitive to several cosmological parameters and today CMB experiments usually have the best constraining power in most parameters. In addition to the temperature, one can also measure the polarisation of the CMB photons, which is affected by gravitational lensing as well as primordial gravitational waves. There have been several experiments so far, starting from ground-based, through balloon experiments ending at space probes. Whereas ground-based and balloon experiments usually only cover a fraction of the sky and are bound to concentrate on small-scale modes in the CMB, space probes can scan the whole extragalactic sky and analyse small as well as large scales. The latest CMB space mission was the European *Planck* satellite (Planck Collaboration et al., 2015a), which carried out an all sky survey of the CMB temperature as well as its polarisation. The accuracy of the results and the best fit power spectra are astonishing (Planck Collaboration et al., 2015c). *Plancks* predecessors were the *COBE* (Mather et al., 1984) and the *WMAP* satellites (Bennett et al., 2003). Ground based experiments are for example the BICEP2 telescope (Ade et al., 2014a), the Atacama Cosmology Telescope (ACT, Swetz et al. 2011), or the South Pole Telescope (SPT, Carlstrom et al. 2011). BICEP focuses on detecting the CMB polarisation, whereas ACT and SPT are by now also capable of that, but were initially designed for the detection of the Sunyaev-Zel'dovich (SZ) effect.

The Sunyaev-Zel'dovich Effect

The CMB photons on their way towards earth are affected by many different phenomena. A particularly interesting one is the Sunyaev-Zel'dovich effect. When CMB photons travel through clusters of galaxies, they can be scattered off the electrons of the ICM. Through this inverse Compton scattering the energy of the photons changes and so does their energy spectrum, as seen in Fig. 1.3. Depending on the frequency of observation, the intensity of CMB photons then either decreases or increases. This means that in the direction of a galaxy cluster a temperature in the CMB will be measured that is different to the average CMB temperature and thus this can be used as a way of cluster detection. This effect has first been described by Sunyaev and Zel'dovich (Sunyaev & Zel'dovich 1970; Sunyaev & Zel'dovich 1980) and it has indeed been used to detect and study galaxy clusters, for example by *Planck* (Planck Collaboration et al., 2015b), ACT (e.g. Hasselfield et al. 2013), or SPT (e.g. Bleem et al. 2015).

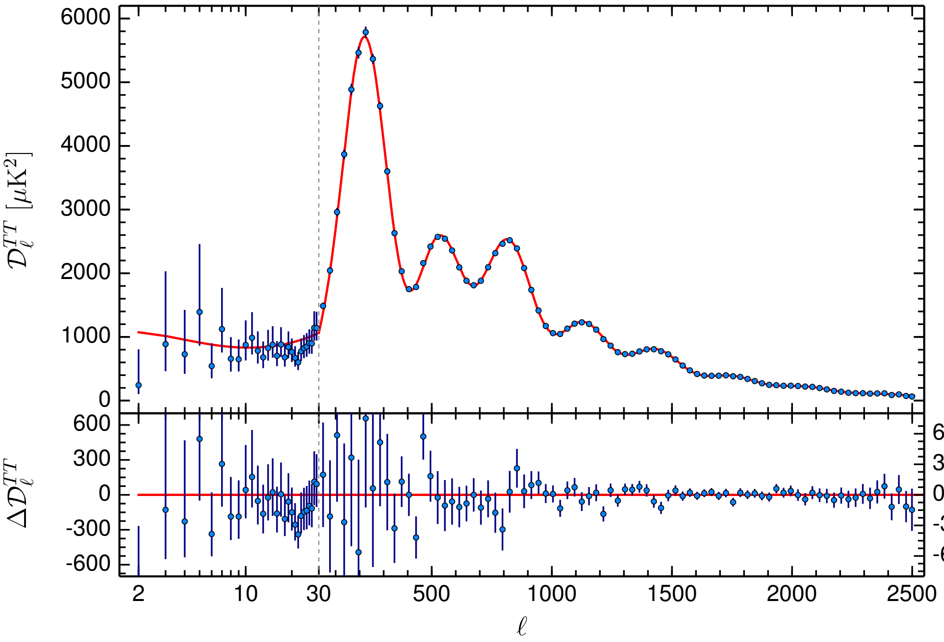

Figure 1.2.: The CMB temperature-temperature power spectrum as measured by *Planck* (Planck Collaboration et al., 2015c).

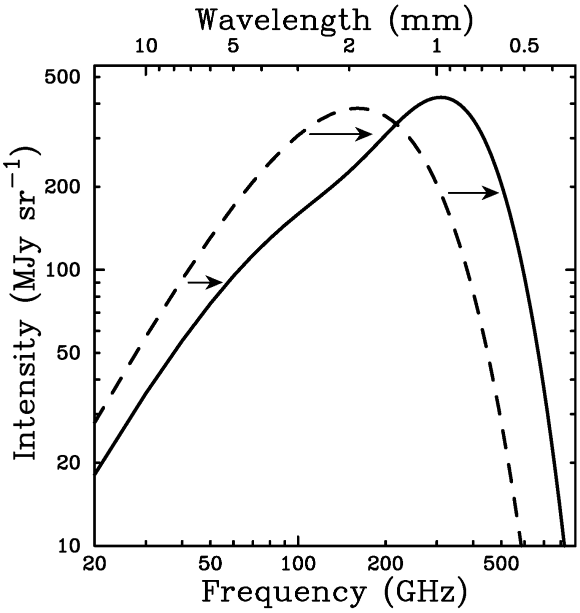

Figure 1.3.: The impact of the SZ-effect on the CMB temperature spectrum (Carlstrom, Holder & Reese, 2002).

1.5.3. Baryonic Acoustic Oscillations

Using galaxy redshift surveys, one can measure the two-point correlation function of the galaxy distribution

$$\xi_{\mathrm{gg}}(\vec{r}) = \langle n_{\mathrm{g}}(\vec{x}) n_{\mathrm{g}}(\vec{x}+\vec{r})\rangle \ , \tag{1.32}$$

which tells us the excess probability of finding a galaxy at a comoving separation $\vec{r}$ to another galaxy at position $\vec{x}$ in comparison to a Poisson distribution. Here n_{g} is the galaxy number density and $\langle\rangle$ is the ensemble average. Its Fourier transform is the power spectrum

$$\mathcal{P}_{\mathrm{gg}}(\vec{k}) = \int \mathrm{d}^3 r \, \xi_{\mathrm{gg}}(\vec{r}) e^{-\mathrm{i}\vec{r}\cdot\vec{k}} \ . \tag{1.33}$$

Those two functions describe the statistical properties of the matter density field. The BAO peaks in the matter field, which we already experienced in the CMB power spectrum, are also imprinted in the matter power spectrum and correlation function. Since we know that galaxies are good tracers of the matter density field, the BAO can also be observed in the galaxy correlation function, ξ_{gg}. The location of the BAO peak in ξ_{gg} can be used as a standard rod to measure the expansion of the Universe as it tells us the size of the sound horizon at recombination and thus it can be used to constrain cosmological parameters.

The most successful experiments in this field of research are the Baryonic Oscillations Spectroscopic Survey (BOSS; e.g. Sánchez et al. 2013) and the WiggleZ survey (e.g. Blake et al. 2012).

1.5.4. Supernovae of Type Ia

Supernovae are explosions of stars, which can be categorised by using the reason for this explosion, as for example a collapsing stellar core. One category is the supernova of type Ia (SNIa). This is caused by a binary star, consisting of a red giant star and a white dwarf. The separation between the two must be sufficiently small so that the white dwarf can accrete mass from its companion. Once the white dwarf mass exceeds the Chandrasekhar limit, the star explodes in a supernova. The Chandrasekhar limit gives the maximum mass for a white dwarf, where the electron degeneracy pressure is still in equilibrium with the gravitational force. This explosion is amongst the most luminous in the Universe and since it is always caused by similar systems, a white dwarf exceeding the Chandrasekhar limit, its luminosity is always approximately the same. This knowledge can be exploited to use supernovae type Ia as standard candles for distance measurements, even at very high redshift. Subsequently, the distance measurements can be used as a probe of the expansion of the Universe and thus to constrain cosmological parameters. The first groups to use SNIa to constrain cosmology were the the High-Z Supernova Search Team (Riess et al., 1998) and the Supernova Cosmology Project (Perlmutter et al., 1999).

1.5.5. Gravitational Lensing

Gravitational lensing means the deflection of light rays by masses, as described by Einstein's theory of general relativity. Chapter 2 will give a detailed introduction to this phenomenon and

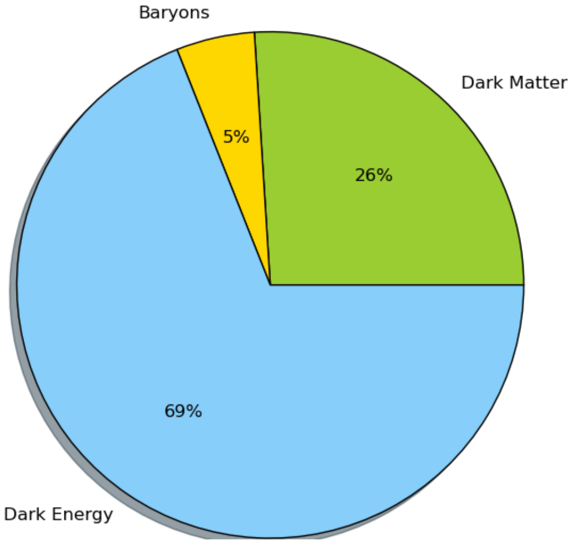

Figure 1.4.: The energy content of the Universe as measured by *Planck* (Planck Collaboration et al., 2015c).

its application, so here we will only acknowledge the fact that different lensing applications can be used as cosmological probes and refer to Chapter 2 for more information.

1.6. The Cosmological Standard Model: ΛCDM

Using the diversity of cosmological probes described above, the astronomical community was able to independently constrain the cosmological parameters and arrived at a concordance model of cosmology. This model is called the Λ cold dark matter (ΛCDM) model. In this model, only about 5 per cent of the Universe consist of ordinary baryonic matter, about 25 per cent of dark matter and roughly 70 per cent of dark energy. The best fit values of some cosmological parameters, including density parameters for dark energy and dark matter, from the *Planck* collaboration can be found in Table 1.1, a graphic that shows the energy content in Fig. 1.4. The ΛCDM universe we think we live in started with the big bang, and then expanded, first through a radiation dominated, then later through a matter dominated phase. In the late times of the Universe, dark energy started to dominate and the expansion started to accelerate.

From intuition it is not at all clear, how astronomers would come up with a world model, that includes mysterious materials like dark energy and dark matter nor what these things are. We will find that the idea of dark matter is already almost a hundred years old, whereas dark energy is a more recent one.

The first hint for dark matter was found in the 1930s by Fritz Zwicky (Zwicky, 1933), who

Table 1.1.: This table shows a few cosmological parameters constrained by the *Planck* satellite while adding information from lensing, BAO, and other data sets (Planck Collaboration et al., 2015c).

Parameter	$\Omega_{\Lambda,0}$	$\Omega_{\mathrm{m},0}$	$\Omega_{\mathrm{b},0}$	$H_0\,[\frac{\mathrm{km}}{\mathrm{s\,Mpc}}]$	σ_8
Best fit	0.6911 ± 0.0062	0.3089 ± 0.0062	0.04851 ± 0.00035	67.74 ± 0.46	0.8159 ± 0.0086

used the virial theorem to estimate the mass of the Coma cluster (more details in Chapter 3). His findings showed that there was apparently more mass than was visible in the optical, thus the term dark matter. This agrees with other studies, like rotation curves of galaxies, or from the CMB. The conclusion is that there must be some new particles, which do not interact with light, but only show themselves via gravity. Nowadays, most people believe that dark matter must be some unknown elementary particle but the search for it is still ongoing.

Dark energy is basically a term to describe the apparent accelerated expansion of the Universe found by Riess et al. (1998) and Perlmutter et al. (1999) at the end of the 20th century. Those teams studied the expansion of the Universe using distant SNIa and found, in contradiction to most expectations, that the Universe's expansion was accelerating. Before, the community was convinced that our Universe was a matter dominated one with $\Omega_{\mathrm{m},0}$ close to unity. It turned out to be quite different. There are several possible explanations for this expansion behaviour, like Einstein's cosmological constant Λ or a new particle. Some researchers even believe that the accelerated expansion is only apparent and that it is due to general relativity failing to describe the Universe on cosmological scales. Unfortunately, so far those are all just guesses and cosmologists are nowhere near finding out what exactly dark energy is. Probably, the next generation of wide field surveys like *Euclid* or LSST will shed light onto this matter.

1.7. Inflation

Although the standard model of cosmology is very successful, there are some problems, which can only be resolved by extensions to the model. Here we will briefly explain those problems and then introduce the idea of inflation, which is the most popular solution to these problems.

The particle horizon is the distance within which regions can have interacted and thus achieve thermal equilibrium. Regions further apart than this distance had no chance of interaction. The particle horizon at the time of recombination can be calculated from theory, and using the known redshift of recombination and the angular diameter distance this can be projected on to the sky. The result is of the order of a few degrees. This means that the CMB temperature should only be the same on scales comparable to the particle horizon. This is not the case. In fact we know the CMB to be homogeneous and isotropic on very large scales. How can this be if widely separated regions had no chance of interaction? This is known as the horizon problem.

Using the first Friedmann equation, one can show that the Universe is evolving away from flatness. Considering the fact that the Universe today is already close to flatness, this means that in early times the Universe must have been even closer to flatness. This leaves an immense fine tuning problem: Why would the Universe from all possible configurations start off that close to flatness? We call this the flatness problem.

These two problems can be solved by a theoretical construct, which is called inflation. In this theory, shortly after the big bang, the Universe undergoes an epoch of exponential expansion. It gets inflated, thus the term inflation. Through inflation all curvature would be wiped out and inflation would leave the Universe almost flat. Also, via inflation formerly connected regions would become so distant that they appeared as informationally disconnected today.

Inflation itself is motivated purely observational. There is no physical need to construct anything like this, except to bring observations in line with the cosmological standard model. There are many theoretical works and different theories how inflation might have worked. The few observables connected to inflation are the slope of the primordial power spectrum, n_s, and the amplitude of a gravitational wave signal imprinted by inflation into the CMB polarisation. The term primordial power spectrum refers to the power spectrum of the density fluctuations at very early times. This can supposedly be described as a power law $\mathcal{P}_\delta(k) \propto k^{n_\mathrm{s}}$. Inflation predicts n_s to be a bit smaller than unity, which is in agreement with findings by *Planck* (Planck Collaboration et al., 2015c). Gravitational waves in the CMB polarisation data have not been discovered yet, although there were recent claims (Ade et al., 2014b), which were later found to be premature (BICEP2/Keck and Planck Collaborations et al., 2015).

1.8. Structure Formation

When considering the small anisotropies in the CMB, a major goal for cosmology should be to find a way to properly describe the evolution from small inhomogeneities in the early Universe to the galaxy clusters and voids we are observing today. In order to achieve this, we first need to find out how density perturbations evolve and how we can describe the density field in a sensible way.

We can describe inhomogeneities in the density field using the so-called density contrast

$$\delta(\vec{x}, t) = \frac{\rho(\vec{x}, t) - \bar{\rho}(t)}{\bar{\rho}(t)} , \tag{1.34}$$

where $\rho(\vec{x}, t)$ is the density at comoving position $\vec{x}$ and time t and $\bar{\rho}(t)$ the mean density. In structure formation theory the horizon scale is an important one, because, as we will see now, it determines the growth of perturbations δ in the density field. For simplicity we define the Hubble scale as the horizon

$$d_\mathrm{h}(t) = \frac{c}{H(t)} . \tag{1.35}$$

At some point in the past all perturbations were larger than the horizon, which is what we call super-horizon perturbations. Later on all perturbations enter the horizon and become sub-horizon perturbations. When considering super-horizon perturbations we find that in a radiation-dominated universe they grow as $\delta \propto a^2$ and in a matter-dominated one with $\delta \propto a$. For a sub-horizon perturbation we find that in a matter-dominated universe the perturbations still grow with a, whereas in a radiation-dominated one they grow with $\delta \propto \ln a$.

For sub-horizon perturbations we can now assume that matter is a fluid, which in the early Universe is a sound assumption. We can then use the continuity equation, the Euler equation, and the Poisson equation given in comoving coordinates to describe the perturbations

$$\frac{\partial \delta}{\partial t} + \frac{1}{a}\nabla_{\vec{x}} \cdot [(1+\delta)\vec{v}] = 0 \ , \tag{1.36}$$

$$\frac{\partial \vec{v}}{\partial t} + \left(\frac{\dot{a}}{a}\right)\vec{v} + \frac{1}{a}(\vec{v} \cdot \nabla_{\vec{x}})\vec{v} = -\frac{\nabla_{\vec{x}}\Phi}{a} - \frac{\nabla_{\vec{x}}p}{a\bar{\rho}(1+\delta)} \ , \tag{1.37}$$

$$\nabla^2_{\vec{x}}\Phi = 4\pi G\bar{\rho}a^2\delta \ , \tag{1.38}$$

where p is the pressure, Φ the gravitational potential, and $\vec{v}$ the peculiar velocity. Here we also assume that the perturbations are embedded in a smoothly expanding universe. If those perturbations are small, they do not influence the evolution of the surrounding universe. We can now assume an equation of state

$$\frac{\nabla_{\vec{x}}p}{\bar{\rho}} = c_{\mathrm{s}}^2\nabla_{\vec{x}}\delta + \frac{2}{3}(1+\delta)T\nabla_{\vec{x}}S \ , \tag{1.39}$$

where c_{s} is the speed of sound and S the entropy, and that δ and $\vec{v}$ are small and thus neglect higher order terms. After some calculus we arrive at the linear growth equation

$$\frac{\partial^2 \delta}{\partial^2 t} + 2\frac{\dot{a}}{a}\frac{\partial \delta}{\partial t} = 4\pi G\bar{\rho}\delta + \frac{c_{\mathrm{s}}^2}{a^2}\nabla^2_{\vec{x}}\delta + \frac{2}{3}\frac{T}{a^2}\nabla^2_{\vec{x}}S \ . \tag{1.40}$$

Eq. (1.40) describes how small perturbations grow in an expanding universe with scale factor a and mean density $\bar{\rho}$. In case of pressureless matter we can find two simple analytic solutions to Eq. (1.40), which in general needs to be solved numerically. A decaying solution is $D_- \propto H(t)$, a growing solution is

$$D_+ \propto H(t)\int_0^t \mathrm{d}t' \frac{t'}{a^2(t')H^2(t')} \ . \tag{1.41}$$

We call D_+ the linear growth factor. Describing the evolution of density perturbations in the non-linear case is not as simple and one is usually in need of numerical simulations. We will not explain this here and instead begin to find a way to describe the initial conditions of the density field in our Universe found in the CMB. Using the linear growth equation and numerical simulations, we can try to evolve initial perturbations like the ones found in the CMB to form the large inhomogeneities we observe today. Due to the fact that initial conditions in the early Universe are one realization of a random field, no simulation will be able to exactly match the outcome of the Universe today. Thus we need some statistical tool to describe the matter distribution in the Universe. For this we will use the already introduced concepts of the two-point correlation function and the power spectrum, which we show here again for the matter distribution

$$\xi_{\mathrm{mm}}(\vec{r}) = \langle \rho_{\mathrm{m}}(\vec{x})\rho_{\mathrm{m}}(\vec{x}+\vec{r})\rangle \ , \tag{1.42}$$

$$\mathcal{P}_{\mathrm{mm}}(\vec{k}) = \int \mathrm{d}^3 r \, \xi_{\mathrm{mm}}(\vec{r})e^{-\mathrm{i}\vec{r}\cdot\vec{k}} \ . \tag{1.43}$$

From theory the shape of the power spectrum can be derived, not so its amplitude, which we need to fix using observations. This amplitude is usually parametrised in terms of the dispersion of the smoothed matter distribution on a scale r

$$\sigma_r^2 = \langle \delta_r^2(\vec{x}) \rangle. \tag{1.44}$$

Observations showed that when one is counting the number of galaxies, N, in spheres of a radius of $8h^{-1}$ Mpc we find

$$\sigma_{\mathrm{gal},8}^2 = \frac{\langle (N - \langle N \rangle)^2 \rangle}{\langle N \rangle^2} \approx 1\ . \tag{1.45}$$

Assuming galaxies are unbiased tracers of the matter distribution this then means that

$$\sigma_8 \approx 1. \tag{1.46}$$

In case of galaxies being a biased tracer σ_8 becomes

$$\sigma_8 = \frac{\sigma_{\mathrm{gal},8}}{b} = \frac{1}{b}\ , \tag{1.47}$$

where b is the galaxy bias. σ_8 is another cosmological parameter.

Using the tools of the power spectrum or the correlation function, we can statistically describe the matter density field in the Universe or in simulations and thus quantify our observations. In fact, the matter power spectrum is one of the easiest predicted observables and thus it is very useful for constraining cosmological parameters. Unfortunately, the matter power spectrum is mostly about dark matter, which cannot be observed and so we have to use other observables, in this case galaxies. The galaxy distribution though cannot be expected to and is indeed known to not exactly follow the matter distribution. This can again be seen in the power spectrum or the correlation function. The difference in the matter and galaxy correlation function can be understood as a measure of how much more galaxies cluster and it is parametrised by the galaxy bias, b. In a simple model one can assume the bias to be linear and deterministic,

$$\mathcal{P}_{\mathrm{gg}} = b^2 \mathcal{P}_{\mathrm{mm}}\ . \tag{1.48}$$

Note that this is usually not a correct assumption unless one is dealing with large scales, where the bias has been found to be mostly constant. Furthermore, we can also connect the two auto-correlations $\mathcal{P}_{\mathrm{gg}}$ and $\mathcal{P}_{\mathrm{mm}}$ using the cross-correlation

$$r_{\mathrm{gm}}^2 = \frac{\mathcal{P}_{\mathrm{gm}}^2}{\mathcal{P}_{\mathrm{gg}} \mathcal{P}_{\mathrm{mm}}}\ , \tag{1.49}$$

where r_{gm} is the cross-correlation coefficient.

Bibliography

Ade P. A. R. et al., 2014a, ApJ, 792, 62

Ade P. A. R. et al., 2014b, Physical Review Letters, 112, 241101

Bennett C. L. et al., 2003, ApJ, 583, 1

BICEP2/Keck and Planck Collaborations et al., 2015, Physical Review Letters, 114, 101301

Blake C. et al., 2012, MNRAS, 425, 405

Bleem L. E. et al., 2015, APJS, 216, 27

Carlstrom J. E. et al., 2011, PASP, 123, 568

Carlstrom J. E., Holder G. P., Reese E. D., 2002, ARA&A, 40, 643

Carrol S. M., 2004, Spacetime and Geometry. Pearson Education

Dodelson S., 2003, Modern Cosmology. Academic Press

Hasselfield M. et al., 2013, JCAP, 7, 8

Mather J. C. et al., 1984, in Bulletin of the American Astronomical Society, Vol. 16, Bulletin of the American Astronomical Society, p. 500

Mo H., van den Bosch F., White S., 2010, Galaxy Formation and Evolution. Cambridge University Press

Perlmutter S. et al., 1999, ApJ, 517, 565

Planck Collaboration et al., 2015a, ArXiv e-prints: 1502.01582

Planck Collaboration et al., 2015b, ArXiv e-prints: 1502.01598

Planck Collaboration et al., 2015c, ArXiv e-prints: 1502.01589

Riess A. G. et al., 1998, AJ, 116, 1009

Sánchez A. G. et al., 2013, MNRAS, 433, 1202

Schneider P., 2006, Extragalactic Astronomy and Cosmology - An Introduction. Springer

Schneider P., 2009, Cosmology Lecture Notes

Serjeant S., 2010, Observational Cosmology. Cambridge University Press in association with The Open University

Sunyaev R. A., Zel'dovich Y. B., 1970, Comments on Astrophysics and Space Physics, 2, 66

Sunyaev R. A., Zel'dovich Y. B., 1980, ARA&A, 18, 537

Swetz D. S. et al., 2011, ApJS, 194, 41

Zwicky F., 1933, Helvetica Physica Acta, 6, 110

CHAPTER 2

Gravitational Lensing

If not stated otherwise, all equations in this chapter are taken from Bartelmann & Schneider (2001).

2.1. Basics of Gravitational Lensing

In Fig. 2.1 we can see the geometry of a typical gravitational lensing system. We have the observer, the lens plane, where the lens is located, and the source plane, where the source is located that emits light that will be deflected by the mass of the lens. A normally continuous light ray in our model can be replaced by two straight lines if the extension of the lens is considerably smaller than its distance to source and observer. We define the angular diameter distance between deflector and observer as D_{d}, the one between deflector and source as D_{ds}, and the one between observer and source as D_{s}. $\vec{\eta}$ is the position of the source in the source plane. It emits a light ray that gets deflected by the lens with the deflection angle $\vec{\alpha}'$. $\vec{\xi}$ is the distance in the lens plane between the lens and the position where the light ray passes through the lens plane. $\vec{\beta}$ is the true source position as seen by the observer, if there was no light deflection, whereas $\vec{\theta}$ is the observed source position. We can safely assume all angles to be small. From the source plane in Fig. 2.1 we see that

$$\vec{\eta} = \vec{a} - \vec{b} \, , \tag{2.1}$$

where we can replace $\vec{a} = \vec{\theta} D_{\mathrm{s}}$ and $\vec{b} = \vec{\alpha}'(\vec{\xi}) D_{\mathrm{ds}}$

$$\vec{\eta} = \vec{\theta} D_{\mathrm{s}} - \vec{\alpha}'(\vec{\xi}) D_{\mathrm{ds}} \, . \tag{2.2}$$

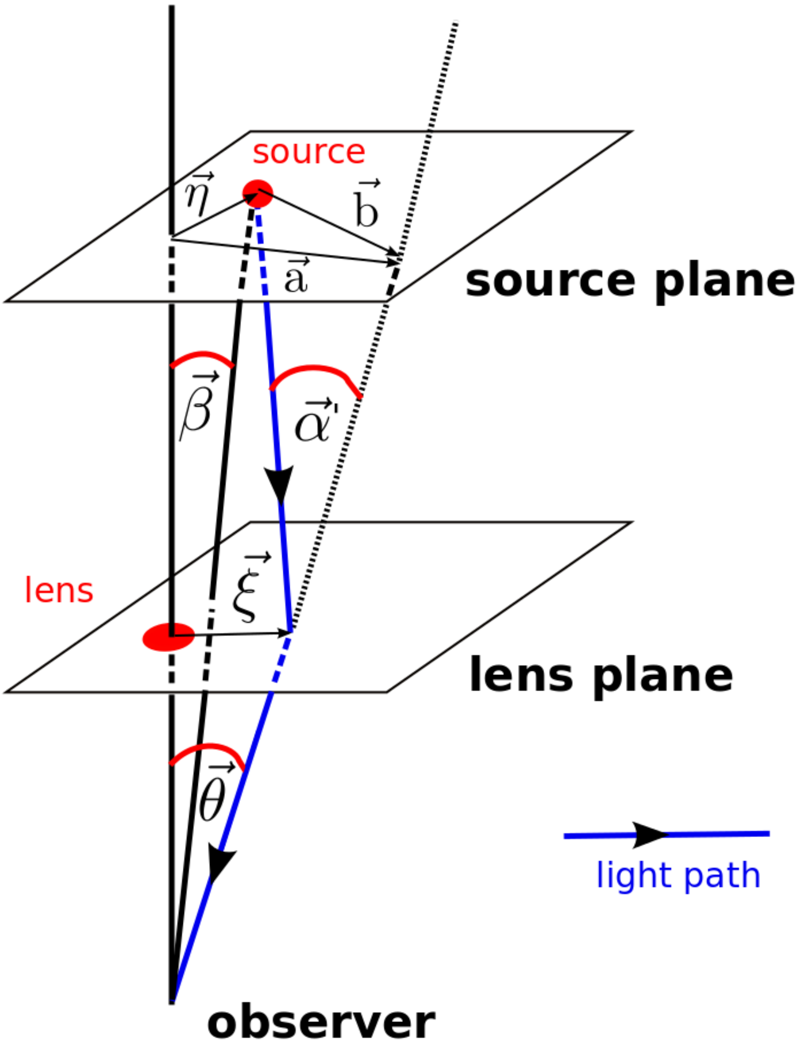

Figure 2.1.: Geometry of a typical gravitational lensing system.

Now we can make use of the definition of the angular diameter distance and divide by D_s, which then yields the lens equation

$$\vec{\beta} = \vec{\theta} - \frac{D_{ds}}{D_s}\vec{\alpha}'(D_d\vec{\theta}) = \vec{\theta} - \vec{\alpha}(\vec{\theta}) \ , \tag{2.3}$$

where in the last step we defined the reduced deflection angle

$$\vec{\alpha}(\vec{\theta}) = \frac{D_\mathrm{ds}}{D_\mathrm{s}}\vec{\alpha}'(D_\mathrm{d}\vec{\theta}) \ . \tag{2.4}$$

Eq. (2.3) can have multiple solutions, each one corresponding to a different image of the source. For a system with a spherically symmetric lens and $\vec{\xi}$ much smaller than the Schwarzschild radius of the lens, the deflections angle is

$$\alpha' = \frac{4GM}{c^2\xi} \ . \tag{2.5}$$

We can plug this into Eq. (2.3) and while using $\theta = \xi/D_\mathrm{d}$ we find

$$\beta = \theta - \frac{D_\mathrm{ds}}{D_\mathrm{d}D_\mathrm{s}}\frac{4GM}{c^2\theta} \ . \tag{2.6}$$

When the source is exactly behind the lens, $\beta = 0$ which leaves us with

$$\theta_\mathrm{E} \coloneqq \sqrt{\frac{D_\mathrm{ds}}{D_\mathrm{d}D_\mathrm{s}}\frac{4GM}{c^2}} \ , \tag{2.7}$$

where we defined the Einstein angle θ_E. This means that in case of a spherically symmetric lens and the source being exactly behind the lens, the image will appear as a ring around the lens. This is called an Einstein ring. The angular radius of the ring is then the Einstein angle or Einstein radius θ_E, which can be used to immediately estimate the mass within the ring.

In case of a three-dimensional density distribution of the lens we can introduce the surface mass density

$$\Sigma(\vec{\xi}) = \int \mathrm{d}r_3 \rho(\xi_1(\lambda), \xi_2(\lambda), r_3(\lambda)) \ , \tag{2.8}$$

where ρ is the density distribution of the lens and ξ_1, ξ_2, and r_3 describe the path of the light ray. λ is an affine parameter. Usually the deflection angles involved are small angles, which is why we can make use of the Born approximation that allows us to describe the path of the light ray as a straight line close to the lens. r_3 then is the path on which the light ray travels. Now we can express the deflection angle using the surface mass density

$$\vec{\alpha}(\vec{\xi}) = \frac{4G}{c^2}\int \mathrm{d}^2\xi' \Sigma(\vec{\xi}')\frac{\vec{\xi} - \vec{\xi}'}{|\vec{\xi} - \vec{\xi}'|^2} \ , \tag{2.9}$$

or by using the convergence κ

$$\vec{\alpha}(\vec{\theta}) = \frac{1}{\pi}\int_{\mathbb{R}^2} \mathrm{d}^2\theta' \kappa(\vec{\theta}')\frac{\vec{\theta} - \vec{\theta}'}{|\vec{\theta} - \vec{\theta}'|^2} \ . \tag{2.10}$$

Here κ is the dimensionless surface mass density defined as

$$\kappa(\vec{\theta}) = \frac{\Sigma(D_{\rm d}\vec{\theta})}{\Sigma_{\rm crit}} \; , \tag{2.11}$$

where $\Sigma_{\rm crit} = \frac{c^2}{4\pi G}\frac{D_{\rm s}}{D_{\rm d}D_{\rm ds}}$. The reduced deflection angle can also be expressed as the gradient of a deflection potential ψ

$$\vec{\alpha} = \nabla\psi(\vec{\theta}) \; , \tag{2.12}$$

where

$$\psi(\vec{\theta}) = \frac{1}{\pi}\int_{\mathbb{R}^2} {\rm d}^2\theta' \kappa(\vec{\theta}') \ln|\vec{\theta} - \vec{\theta}'| \; . \tag{2.13}$$

Finally, we can say that

$$\nabla^2\psi = 2\kappa \; , \tag{2.14}$$

while making use of $\nabla^2 \ln|\vec{\theta}| = 2\pi\delta_{\rm D}(\vec{\theta})$, where in this case $\delta_{\rm D}$ is the Dirac delta function.

2.2. Weak Gravitational Lensing

So far, we only considered point sources or single light rays, but what happens with extended sources? Images of extended sources will get distorted due to the differential deflection of every light ray belonging to the image. The distortion of such an image is described by the Jacobian of the lens equation

$$\mathcal{A}(\vec{\theta}) = \frac{\partial\vec{\beta}}{\partial\vec{\theta}} = \delta_{ij} - \frac{\partial^2\psi(\vec{\theta})}{\partial\theta_i\partial\theta_j} = \begin{pmatrix} 1-\kappa-\gamma_1 & -\gamma_2 \\ -\gamma_2 & 1-\kappa+\gamma_1 \end{pmatrix} \; , \tag{2.15}$$

where γ is the so-called shear. It is a complex number and thus has two components γ_1 and γ_2

$$\gamma = \gamma_1 + {\rm i}\gamma_2 \; . \tag{2.16}$$

The inverse of the determinant of $\mathcal{A}$ is the magnification

$$\mu(\vec{\theta}) = \frac{1}{\det(\mathcal{A}(\vec{\theta}))} = \frac{1}{(1-\kappa)^2 - |\gamma|^2} \; . \tag{2.17}$$

In extreme cases, lensing can lead to giant arcs (see Section 2.3). However, when κ and $|\gamma|$ are both much smaller than unity, we are in the weak gravitational lensing regime, where these distortions are only small and the effect is subtle. In order to describe the change in galaxy shapes we first need to be able to quantify the shape. We do this by introducing the complex ellipticity

$$\epsilon = |\epsilon|e^{2{\rm i}\phi} \; , \tag{2.18}$$

where ϕ in this case is the position angle and

$$|\epsilon| = \frac{1-r}{1+r} \; , \tag{2.19}$$

with r being the axis ratio of the light distribution of the image of a galaxy. It was shown that the ellipticity under lensing changes as follows (Schneider & Seitz, 1995)

$$\epsilon_{\rm len} = \frac{\epsilon_{\rm int} + g}{1 + g^* \epsilon_{\rm int}}, |g| \leq 1 \quad \text{or} \quad \epsilon_{\rm len} = \frac{1 + g\epsilon^*_{\rm int}}{\epsilon^*_{\rm int} + g^*}, |g| > 1 \; , \tag{2.20}$$

where g is the reduced shear

$$g = \frac{\gamma}{1-\kappa} = g_1 + {\rm i} g_2 = |g| e^{2{\rm i}\phi} \; . \tag{2.21}$$

The change in ellipticity depends only on the reduced shear, not on κ and γ separately, thus g is the only quantity that can be inferred from measuring galaxy ellipticities.

In practice one does not know the intrinsic ellipticities of background galaxies and thus it is not possible to judge if a single galaxy has been lensed or not. For a large enough ensemble of galaxies, however, we can assume that due to the cosmological principle $\langle \epsilon_{\rm int} \rangle = 0$. If those galaxies were lensed this would not be the case. So for an ensemble of galaxies it is possible to measure the weak gravitational lensing signal. Typical lenses here can be galaxies, galaxy clusters or even the large scale structure of the universe. We will describe these applications in the next sections.

2.2.1. Cluster Weak Lensing

The gravitational potential of a single galaxy cluster can act as a gravitational lens in the strong (see Section 2.3) as well as the weak lensing regime. In order to find the weak lensing signal around a galaxy cluster, one usually uses the tangential shear,

$$\gamma_{\rm t} = -\Re[\gamma e^{-2{\rm i}\phi}] \; , \tag{2.22}$$

where ϕ is the angle that describes the position of the source galaxy with respect to the lens, which is in the centre of the coordinate frame. Astronomical lenses like galaxy clusters or galaxies should introduce a distortion to the sources that is tangential with respect to the lens centre. Thus, we use the tangential part of the shear whereas the cross shear,

$$\gamma_{\rm x} = -\Im[\gamma e^{-2{\rm i}\phi}] \; , \tag{2.23}$$

will be zero in such a case. If a non-zero $\gamma_{\rm x}$ is measured, this normally points to systematics in the data. Usually, $\gamma_{\rm t}$ is measured in annular bins around the lens. So instead of just having one source galaxy, people make use of all background galaxies around the cluster and thus measure the average $\gamma_{\rm t}$ as a function of separation to the lens. When assuming a mass profile for the lens, this signal can be predicted and using this, a mass for the cluster can be estimated. When redshift information is available one can also use the annular differential excess surface mass density

$$\Delta\Sigma(R) = \langle \gamma_{\rm t} \rangle \Sigma_{\rm crit} \tag{2.24}$$

as the lensing observable, where R is the projected separation between lens and source. A statistically complete sample of clusters can even be used to measure the so-called halo mass function and thus to constrain cosmological parameters. Recent results of cluster lensing studies can for example be found in Applegate et al. (2014) and Hoekstra et al. (2015).

2.2.2. Galaxy-Galaxy Lensing

Instead of a cluster of galaxies, one can also measure the average tangential shear as a function of separation around galaxies. The signal of a single galaxy is normally not strong enough to be detected, which can be overcome by stacking the signal of many lens galaxies. The resulting signal can then be used to learn about the average properties of the lens population. Recent results in this field are for example van Uitert et al. (2011), van Uitert et al. (2012), Mandelbaum et al. (2013), or Velander et al. (2014). An actual application of galaxy-galaxy lensing can be found in Chapter 6.

2.2.3. Cosmic Shear

Light rays emitted by a high-redshift source get deflected many times on their way to the observer. The lens in this case is the large scale structure of the universe. This deflection again changes the shapes of galaxies and can be measured in a statistical sense. The tools being used here are two-point statistics of the shear, namely the correlation functions

$$\begin{aligned} \xi_+(\vartheta) &= \langle\gamma_\mathrm{t}\gamma_\mathrm{t}\rangle(\vartheta) + \langle\gamma_\mathrm{x}\gamma_\mathrm{x}\rangle(\vartheta) \;, && (2.25)\\ \xi_-(\vartheta) &= \langle\gamma_\mathrm{t}\gamma_\mathrm{t}\rangle(\vartheta) - \langle\gamma_\mathrm{x}\gamma_\mathrm{x}\rangle(\vartheta) \;, && (2.26)\\ \xi_\mathrm{x}(\vartheta) &= \langle\gamma_\mathrm{t}\gamma_\mathrm{x}\rangle(\vartheta) \;. && (2.27) \end{aligned}$$

Here we use pairs of galaxies, each with a measured ellipticity, to estimate these functions, which is why we can again define a tangential as well as a cross part of the shear for each pair. Those functions are directly connected to the convergence power spectrum and thus to the matter power spectrum. This makes cosmic shear a powerful tool to constrain cosmological parameters. The first detections of cosmic shear happened about 15 years ago. Recent results are for example Schrabback et al. (2010) or Heymans et al. (2013).

2.2.4. The Aperture Mass

A special estimator for weak gravitational lensing is the aperture mass (Schneider 1996; Schneider et al. 1998). It was initially designed to overcome the mass-sheet degeneracy, which describes the problem that κ for a given lens can only be constrained up to a constant λ, which means that we cannot observe a difference between κ and a κ', where

$$\kappa'(\vec{\theta}) = \lambda\kappa(\vec{\theta}) + (1-\lambda) \;. \tag{2.28}$$

The aperture mass M_ap is now defined in such a way that it is insensitive to the mass sheet degeneracy. We define it as

$$M_\mathrm{ap} = \int \mathrm{d}\phi\, \phi\, \mathcal{U}(\phi)\, \kappa(\phi) \;, \tag{2.29}$$

where $\mathcal{U}$ is a compensated filter function and ϕ the aperture radius. In terms of the tangential shear γ_t instead of the convergence κ, it turns into

$$M_\mathrm{ap} = \int \mathrm{d}\phi\, \phi\, \mathcal{Q}(\phi)\, \gamma_\mathrm{t}(\phi) \;, \tag{2.30}$$

where $\mathcal{Q}$ is related to $\mathcal{U}$ via

$$\mathcal{Q}(\phi) = \frac{2}{\phi^2} \int_0^{\phi} \mathrm{d}\phi' \, \phi' \, \mathcal{U}(\phi') - \mathcal{U}(\phi) \; . \tag{2.31}$$

Several possible filters have been suggested and used in measurements, most of them polynomials. In Chapter 6 we will present a new set of filters for M_{ap} and apply these new estimators to data.

2.3. Strong Gravitational Lensing

If κ and $|\gamma|$ are of the order of 1, we are in the strong gravitational lensing regime. Massive lenses lead to the deflection of the emitted light of a source, which can result in multiple images, magnified images, and distorted images. The image distortion can lead to intrinsically elliptical background galaxies appearing as arcs in the vicinity of galaxy clusters or, when lens, source, and observer are aligned, to a complete ring, the Einstein ring. The radius of the ring or the curvature radius of arcs are called Einstein radius and, as mentioned before, can be used as a simple measure of the lens mass. In case of imperfect alignment also incomplete rings can appear. Furthermore, the position of multiple images and arcs can be used to build a lens model, which again can be used to find the mass of the lens. Typical lenses for these phenomena are single galaxies and clusters of galaxies.

When the source in a multiply imaged system is intrinsically variable, this can be used for constraining the Hubble constant, H_0. The path of the light rays of the multiple images will be different and hence also the light travel time between source and observer. Using long term photometric monitoring light curves of the different images can be produced and the time delay, Δt, can be measured, which is proportional to H_0.

Strong gravitational lensing does not play an important role in this work, so we will not discuss it in more detail here.

2.4. Microlensing

So far, the phenomena we discussed were all about extragalactic lenses and sources, such as galaxies and galaxy clusters. There is, however, the possibility of lower mass objects within the Milky Way to act as a lens, such as a black hole. When observing stars for example in the Magellanic clouds, it can happen that a lens passes between the observer and the star. Due to the mass of the lens the star light will be magnified for a short while. In long term photometric monitoring of stars such an event will create a distinct shape in the light curve and can thus be detected. The phenomenon of microlensing has been used for example to search for macroscopic dark matter in the Milky Way halo (e.g. Alcock et al. 1995) or quite recently to search for extrasolar planets (e.g. Kains et al. 2013; Skowron et al. 2015).

Bibliography

Alcock C. et al., 1995, ApJ, 445, 133

Applegate D. et al., 2014, MNRAS, 439, 48

Bartelmann M., Schneider P., 2001, PhR, 340, 291

Heymans C. et al., 2013, MNRAS, 432, 2433

Hoekstra H., Herbonnet R., Muzzin A., Babul A., Mahdavi A., Viola M., Cacciato M., 2015, MNRAS, 449, 685

Kains N. et al., 2013, A&A, 552, A70

Mandelbaum R., Slosar A., Baldauf T., Seljak U., Hirata C. M., Nakajima R., Reyes R., Smith R. E., 2013, MNRAS, 432, 1544

Schneider P., 1996, MNRAS, 283, 837

Schneider P., Seitz C., 1995, A&A, 294, 411

Schneider P., van Waerbeke L., Jain B., Kruse G., 1998, MNRAS, 296, 873

Schrabback T. et al., 2010, A&A, 516, A63

Skowron J. et al., 2015, ApJ, 804, 33

van Uitert E., Hoekstra H., Schrabback T., Gilbank D. G., Gladders M. D., Yee H. K. C., 2012, A&A, 545, A71

van Uitert E., Hoekstra H., Velander M., Gilbank D. G., Gladders M. D., Yee H. K. C., 2011, A&A, 534, A14

Velander M. et al., 2014, MNRAS, 437, 2111

CHAPTER 3

Clusters of Galaxies

Most parts of this chapter are based on the introduction of Buddendiek et al. (2015) published in *Monthly Notices of the Royal Astronomical Society*, Volume 450, Issue 4, p. 4248-4276.

3.1. Content of Galaxy Clusters

Galaxy clusters are the largest gravitationally collapsed structures in the Universe and as such a valuable tool for cosmology. Already in the early 20th century it had been shown that most of the mass in the Coma cluster is not visible in the optical (Zwicky, 1933). It turned out that indeed galaxies make up only about one per cent of the total mass of a galaxy cluster. About ten per cent is hot gas, the ICM, the rest is dark matter. In the centre of a cluster one usually finds a giant elliptical galaxy, which is at the same time the brightest cluster galaxy (BCG). The first large catalogue of galaxy clusters has been assembled by Abell in the 1950s (Abell, 1958). This has been done by visually inspecting photographic plates and looking for galaxy overdensities. In the course of this chapter we will describe briefly how galaxy clusters can be detected, how their mass can be estimated, and the ways clusters can be used as cosmological tools. Thereby, we will focus on the cosmological aspects and not go into detail concerning studies of cluster physics.

3.2. Detecting Clusters of Galaxies in Different Wavelength Regimes

Clusters of galaxies, especially at high-redshift, are important tools to study our Universe. Years before the discovery of dark energy in the late 20th century, cluster studies already pointed towards an $\Omega_{\mathrm{m},0}$ much smaller than unity (e.g. White et al. 1993; Bahcall, Lubin & Dorman 1995). Furthermore, one can measure the total number of clusters per mass bin and compare it to theoretical predictions. In order to conduct such a cosmological analysis of a sample of galaxy clusters, one first has to find them. Galaxy cluster detection is possible in many different ways depending on the wavelength. Since the intra-cluster medium (ICM) emits in the X-ray, one can use X-ray surveys to detect clusters. This has been done many times using different X-ray observatories. For example using the *ROSAT* satellite (e.g. XBAC: Ebeling et al. 1996; BCS: Ebeling et al. 1998; MACS: Ebeling, Edge & Henry 2001; HIFLUGCS: Reiprich & Böhringer 2002; 400D Cluster Survey: Burenin et al. 2007) or the *XMM Newton* satellite (e.g. XCS: Romer et al. 2001, Mehrtens et al. 2012; XMM LSS: Pierre et al. 2001, Pierre, Valtchanov & Refregier 2002; REXCESS: Böhringer et al. 2007). Using the X-ray emission of the ICM, one can measure the temperature of the gas, which probes the full gravitational potential of the cluster. Consequently, the X-ray properties of clusters correlate well with mass (e.g. Mahdavi et al. 2013). Once redshift, mass, and the selection function are known, the samples can be used for constraining cosmological parameters (e.g. Vikhlinin et al. 2009a; Mantz et al. 2014).

As already mentioned in Section 1.5.2, CMB photons experience inverse Compton scattering due to the electrons in the ICM and thus the CMB spectrum changes. Depending on the frequency one will either observe a decrease in photons or an increase, which is known as the SZ effect. The SZ effect is also being used as another way to find galaxy clusters for example by the South Pole Telescope (SPT, e.g. Bleem et al. 2015), the Atacama Cosmology Telescope (ACT, e.g. Hasselfield et al. 2013) or the *Planck* satellite (Planck Collaboration et al., 2015a). The SZ effect probes the integrated pressure of the ICM, which probes the gravitational potential and has also been found to correlate well with mass (e.g. Bonamente et al. 2008). SZ-selected samples have been used for cosmological parameter constraints (e.g. Benson et al. 2013; Sievers et al. 2013; Planck Collaboration et al. 2015b).

Galaxy cluster detection in the optical works somewhat differently. Most cluster finding algorithms look for overdensities in the galaxy distribution. Nowadays, this is usually combined with magnitude information or photometric redshifts (e.g. Postman et al. 1996; Milkeraitis et al. 2010). Similar to photometric redshifts one can also use colour information and an intrinsic property of clusters, the cluster red sequence. This red sequence can be observed as a region in the colour-magnitude diagram, where red galaxies of the same cluster align along a line of almost constant colour (Gladders & Yee, 2000). This is due to the redshift dependent shift of the 4000 Å-break through the filter bands in use, which is why the location of the red sequence in colour-magnitude space can be used as an estimator for the cluster redshift.

The red sequence method has also been used for cluster detection, for example by the Red Cluster Sequence Surveys 1 and 2 (Gladders & Yee 2005; Gilbank et al. 2011), by the MaxBCG program (Koester et al., 2007), or redMaPPer (Rykoff et al., 2014). Besides giving an estimate for the cluster redshift optical surveys can also provide estimates of “cluster richness”, which is the number of cluster galaxies within a certain radius and brighter than some characteristic magnitude. Several cluster surveys have been generated around various richness measures (e.g. Koester et al. 2007; High et al. 2010; Rykoff et al. 2014) and it has been shown to correlate with mass (e.g. Planck Collaboration et al. 2011, Sehgal et al. 2013) although this relation appears to have large intrinsic scatter (Angulo et al., 2012).

Usually, the methods of cluster detection that do not make use of optical observations require some kind of confirmation from a different wavelength regime. This can be overcome by cross-correlating data from two different regimes. This has been done using optical and X-ray data by for example the Massive Cluster Survey (MACS, Ebeling, Edge & Henry 2001), the RASS-SDSS Galaxy Cluster Survey (Popesso et al., 2004), or the extended MACS (eMACS, Ebeling et al. 2013). Also optical and infra-red data have been combined by the Massive Distant Clusters of Wise Survey (MaDCoWS, Brodwin et al. 2015).

Over the last few years, more large volume surveys were conducted. Especially the *Planck* satellite has been shown to find massive galaxy clusters at redshifts greater than $z = 0.5$ (Planck Collaboration et al., 2014) spread over the whole sky. This is complementary to the samples found by the SPT (Bleem et al., 2015) and ACT (Hasselfield et al., 2013), which originate from a smaller area and consist of typically slightly less massive but higher redshift clusters.

3.3. Determining the Mass of Clusters of Galaxies

For cosmological cluster studies the masses of the clusters play a crucial role, as we will see later on in this chapter and Chapter 5. Before explaining this, we will first briefly introduce some possibilities of estimating the mass of a galaxy cluster. As it is not intuitively clear what the mass of a cluster means, we define r_{500} (r_{200}) as the radius, where the density of the galaxy cluster is 500 (200) times the critical density of the universe. We then take M_{500} (M_{200}) to be the mass within this radius.

3.3.1. Strong and Weak Gravitational Lensing

Gravitational lensing is a great tool to measure the total mass of objects, also of clusters, as it probes not only the visible but also the dark matter. For the inner $\sim 100\,\mathrm{kpc}$ of a cluster, strong gravitational lensing can be used to constrain the cluster mass. This can be done by finding mass models using multiple images of the same background sources or by using the Einstein angle of giant luminous arcs. As we explained in Chapter 2, the Einstein angle can immediately be used as a mass proxy. If one is interested in the cluster mass on larger scales, weak lensing is the tool to use. Due to the gravitational potential of the cluster, the light of background galaxies gets deflected and their shapes distorted. Statistically this can be measured as the tangential shear γ_t as a function of distance to the cluster centre. While assuming a model for the mass profile, the expected tangential shear can be computed and fitted to the measured shear profile. The constrained mass profile can then be used to find the mass of the cluster (see Chapter 2).

3.3.2. Dynamical Mass Estimation

Mass estimation is also possible by using dynamical information, namely the motions of galaxies inside the cluster. For this to work we need to obtain a great number of spectra of cluster members, from which we can measure peculiar velocities. We can then use the virial theorem to find the mass of the cluster (e.g. Maurogordato et al. 2008). We will now give a brief derivation of this method closely following the one from Schneider (2006).

The virial theorem states that in a dynamically bound system, like a galaxy cluster, the potential energy E_{pot} is equal to twice the kinetic energy E_{kin}

$$-E_{\mathrm{pot}} = 2E_{\mathrm{kin}} \; . \tag{3.1}$$

We can define the energies of the cluster as the sum over the energies of all cluster galaxies, which yields

$$E_{\mathrm{kin}} = \frac{1}{2}\sum_i m_i v_i^2 \tag{3.2}$$

and

$$E_{\mathrm{pot}} = -\frac{1}{2}\sum_{i\neq j} \frac{G m_i m_j}{r_{ij}} \; , \tag{3.3}$$

where m_i is the mass of the ith galaxy, v_i the absolute value of the velocity of the ith galaxy, and r_{ij} the absolute value of the three dimensional separation between the ith and jth galaxy. Now we define the total mass of the cluster as $M_i = \sum\limits_i m_i$, the three dimensional velocity dispersion as $\langle v^2 \rangle = \frac{1}{M}\sum\limits_i m_i v_i^2$, and the three dimensional gravitational radius as $r_{\mathrm{G}} = 2M^2 \left(\sum\limits_{i\neq j} \frac{m_i m_j}{r_{ij}} \right)^{-1}$. All these equations, when plugged into the virial theorem, yield

$$M = \frac{\langle v^2 \rangle r_{\mathrm{G}}}{G} \; . \tag{3.4}$$

This expression makes use of three dimensional quantities such as $\langle v^2 \rangle$. In order to connect this to observables we need to use two dimensional quantities. In case of an isotropic velocity distribution we can use $\langle v^2 \rangle = 3\sigma_v^2$, where σ_v^2 is the two dimensional velocity dispersion, which can be measured using galaxy spectra. Additionally, we use $r_{\mathrm{G}} = \frac{\pi}{2} R_{\mathrm{G}}$, with $R_{\mathrm{G}} = 2M \left(\sum\limits_{i\neq j} \frac{m_i m_j}{r_{ij}} \right)^{-1}$, the absolute value of the two dimensional separation of the ith and jth galaxy. This then yields an expression for the total mass of a cluster using only observables

$$M = \frac{3\pi}{2} \frac{\sigma_v^2 R_{\mathrm{G}}}{G} \; . \tag{3.5}$$

This means that by assuming that the cluster is dynamically bound and by taking a large number of galaxy spectra, it is possible to estimate the dynamical mass of a galaxy cluster. However, we should note that this is an especially expensive way of mass determination in terms of observing time. Particularly, for high-redshift galaxy clusters it becomes increasingly hard to take reasonable spectra of a sufficient number of cluster members. This is probably a reason why this method is not as popular in estimating cluster masses as for example lensing.

3.3.3. Scaling Relations using Optical-, Radio-, and X-ray-Data

Weak lensing cluster mass estimates as described before can be used to calibrate scaling relations between the cluster mass and several observables that are known to correlate well with mass, but are easier to measure than the weak lensing mass. Those observables are usually the X-ray temperature of the ICM, T_X, and the integrated pressure of the ICM, Y_SZ, which can be measured using the SZ effect. A more detailed explanation of how to measure Y_SZ can be found in Chapter 5. In order to find a general scaling relation, the selection function of the cluster sample needs to be known and be corrected for. An example for a $Y_\mathrm{SZ} - M$ scaling relation will be applied to data in Chapter 5. A recent work with constrained scaling relations is for example Andersson et al. (2011).

3.4. Galaxy Clusters as a Cosmological Probe

3.4.1. Cluster Counting Experiments

The halo mass function is used to compute the number density of halos for a given mass bin. The number density of clusters, depends strongly on the initial conditions of the matter field they form in, which depend on the cosmology. Thus the cluster number density can be used for cosmological studies. The halo mass function can be constrained at the high mass end by counting galaxy clusters as a function of mass. Although the concept appears simple, it requires well calibrated mass measurements (e.g. from weak lensing or from the X-ray) as well as a statistically complete sample of clusters. Recent studies are Vikhlinin et al. (2009b), who use masses determined from X-ray data, or Planck Collaboration et al. (2015b), who use the data of the *Planck* satellite.

3.4.2. Probing the Extreme End of the Mass Function: Galaxy Clusters too Massive for our Universe

The most extreme clusters in mass ($M_{200} \geq 5 \times 10^{14} M_\odot$) can be used for a cosmological test other than cluster counting. Given a cosmological model, one can compute the highest possible masses of galaxy clusters as a function of redshift (Haiman, Mohr & Holder 2001; Weller, Battye & Kneissl 2002). This probes the extreme end of the mass function. In order to systematically search for the most massive clusters in our Universe, a deep and wide area survey that probes large volumes needs to be carried out. Until recently, mostly samples consisting of only a few clusters that were discovered in small surveys were tested for consistency with the ΛCDM model. For example, Broadhurst & Barkana (2008) used mass estimates based on strong lensing arcs of four galaxy clusters, whereas Jee et al. (2011) used weak gravitational lensing masses of 22 clusters. In Mortonson, Hu & Huterer (2011) two clusters are tested and the authors provide a fitting formula for exclusion curves, which was shown to be too strict by Hotchkiss (2011). In contrast to testing single cluster masses for consistency with the standard cosmological model one can also use extreme number statistics and test a whole sample of clusters (Waizmann, Redlich & Bartelmann 2012; Waizmann, Ettori & Bartelmann 2013). So far only Jee et al. (2011) find significant deviations from ΛCDM, using the exclusion curves from Mortonson, Hu & Huterer (2011). Considering the findings of Hotchkiss (2011), this tension has likely been resolved.

Bibliography

Abell G. O., 1958, ApJS, 3, 211

Andersson K. et al., 2011, ApJ, 738, 48

Angulo R. E., Springel V., White S. D. M., Jenkins A., Baugh C. M., Frenk C. S., 2012, MNRAS, 426, 2046

Bahcall N. A., Lubin L. M., Dorman V., 1995, ApJ, 447, L81

Benson B. A. et al., 2013, ApJ, 763, 147

Bleem L. E. et al., 2015, ApJS, 216, 27

Böhringer H. et al., 2007, A&A, 469, 363

Bonamente M., Joy M., LaRoque S. J., Carlstrom J. E., Nagai D., Marrone D. P., 2008, ApJ, 675, 106

Broadhurst T. J., Barkana R., 2008, MNRAS, 390, 1647

Brodwin M. et al., 2015, ApJ, 806, 26

Buddendiek A. et al., 2015, MNRAS, 450, 4248

Burenin R. A., Vikhlinin A., Hornstrup A., Ebeling H., Quintana H., Mescheryakov A., 2007, ApJS, 172, 561

Ebeling H., Edge A. C., Böhringer H., Allen S. W., Crawford C. S., Fabian A. C., Voges W., Huchra J. P., 1998, MNRAS, 301, 881

Ebeling H. et al., 2013, MNRAS, 432, 62

Ebeling H., Edge A. C., Henry J. P., 2001, ApJ, 553, 668

Ebeling H., Voges W., Böhringer H., Edge A. C., Huchra J. P., Briel U. G., 1996, MNRAS, 281, 799

Gilbank D. G., Gladders M. D., Yee H. K. C., Hsieh B. C., 2011, AJ, 141, 94

Gladders M. D., Yee H. K. C., 2000, AJ, 120, 2148

Gladders M. D., Yee H. K. C., 2005, ApJS, 157, 1

Haiman Z., Mohr J. J., Holder G. P., 2001, ApJ, 553, 545

Hasselfield M. et al., 2013, JCAP, 7, 8

High F. W. et al., 2010, ApJ, 723, 1736

Hotchkiss S., 2011, JCAP, 7, 4

Jee M. J. et al., 2011, ApJ, 737, 59

Koester B. P. et al., 2007, ApJ, 660, 221

Mahdavi A., Hoekstra H., Babul A., Bildfell C., Jeltema T., Henry J. P., 2013, ApJ, 767, 116

Mantz A. B., Allen S. W., Morris R. G., Rapetti D. A., Applegate D. E., Kelly P. L., von der Linden A., Schmidt R. W., 2014, MNRAS, 440, 2077

Maurogordato S. et al., 2008, A&A, 481, 593

Mehrtens N. et al., 2012, MNRAS, 423, 1024

Milkeraitis M., van Waerbeke L., Heymans C., Hildebrandt H., Dietrich J. P., Erben T., 2010, MNRAS, 406, 673

Mortonson M. J., Hu W., Huterer D., 2011, Phys. Rev. D, 83, 023015

Pierre M. et al., 2001, The Messenger, 105, 32

Pierre M., Valtchanov I., Refregier A., 2002, ArXiv Astrophysics e-prints

Planck Collaboration et al., 2014, A&A, 571, A29

Planck Collaboration et al., 2015a, ArXiv e-prints: 1502.01598

Planck Collaboration et al., 2015b, ArXiv e-prints: 1502.01597

Planck Collaboration et al., 2011, A&A, 536, A12

Popesso P., Böhringer H., Brinkmann J., Voges W., York D. G., 2004, A&A, 423, 449

Postman M., Lubin L. M., Gunn J. E., Oke J. B., Hoessel J. G., Schneider D. P., Christensen J. A., 1996, AJ, 111, 615

Reiprich T. H., Böhringer H., 2002, ApJ, 567, 716

Romer A. K., Viana P. T. P., Liddle A. R., Mann R. G., 2001, ApJ, 547, 594

Rykoff E. S. et al., 2014, ApJ, 785, 104

Schneider P., 2006, Extragalactic Astronomy and Cosmology - An Introduction. Springer

Sehgal N. et al., 2013, ApJ, 767, 38

Sievers J. L. et al., 2013, JCAP, 10, 60

Vikhlinin A. et al., 2009a, ApJ, 692, 1060

Vikhlinin A. et al., 2009b, ApJ, 692, 1060

Waizmann J.-C., Ettori S., Bartelmann M., 2013, MNRAS, 432, 914

Waizmann J.-C., Redlich M., Bartelmann M., 2012, A&A, 547, A67

Weller J., Battye R. A., Kneissl R., 2002, Physical Review Letters, 88, 231301

White S. D. M., Navarro J. F., Evrard A. E., Frenk C. S., 1993, Nature, 366, 429

Zwicky F., 1933, Helvetica Physica Acta, 6, 110

CHAPTER 4

Correcting for CCD Crosstalk in OmegaCAM@VST

4.1. Basics of Charge Coupled Devices

This introduction to CCD detectors is based on the chapters concerning CCDs in Rieke (2003).

Charge Coupled Devices (CCD) are semi-conductor detectors that were developed in 1969 in the Bell Labs. Nowadays, basically all optical telescopes used for scientific research are using cameras based on CCDs. Here we will give a brief introduction to how CCDs work and why they are being used. For more detailed explanations, we refer to literature about semi-conductor physics or detectors.

In a piece of semi-conductor material, we can apply condensed matter theories to describe the principles of a CCD. Electrons in such a piece exist in huge numbers and can move freely. Due to their high numbers they populate vast amounts of energy levels with very small differences in energy. Those can effectively be treated as energy bands. We will consider two bands here, the conduction band as well as the valence band. In metals all electrons are in the conduction band, whereas in insulators all electrons are in the valence band. Semi-conductors are somewhere in between those two cases. Between the valence and the conduction band is the band gap. If an electron in the valence band gets sufficiently excited by an incoming photon it can leave the valence band, cross the band gap and reach the conduction band, where it can contribute to the electrical current and can thus be measured. In an insulator this band gap crossing is not possible because the energy gap is too large. The basic principle of CCD semi-conductor detectors is that incoming photons excite electrons in the valence band, which are then counted in the conduction band. In CCD detectors each pixel has such a photo-active region. The charge carriers excited

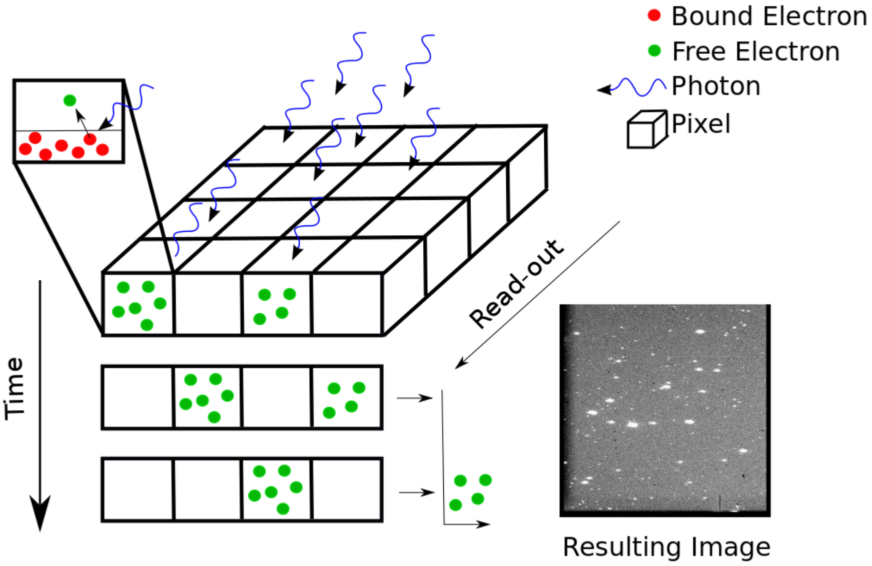

Figure 4.1.: This figure shows the basic concepts of a CCD Detector in a schematic way. The incoming photons enter the CCD and excite electrons that are read out by applying voltages and finally counted, which results in the raw image seen on the bottom right.

by incoming light are trapped by a capacitor. Using voltage, the charges can be transferred from one pixel to the next, which is used for the read-out. In case of a CCD in a camera, this results in a two dimensional array that contains the number of electrons counted per pixel. This is then interpreted as a grey-shaded image, where the number of counts is proportional to the number of incoming photons. This is of course only a very basic description of the much more complicated works of a CCD detector. Nevertheless, it is sufficient to understand the basic behaviour of such detectors. A schematic view of a how a CCD detector works is displayed in Fig. 4.1. For a more detailed introduction to detectors in astronomy see for example Rieke (2003).

CCD detectors are being used in astronomy due to some great properties. Compared to the photographic plates that had been used for decades before, they react in a much more predictable way. The amount of charge counted for the images for example goes linear with the amount of light exposed to the detector. Additionally, their quantum efficiency is much higher, which means that most of the light gets converted into charge during the exposure. Furthermore, it is possible to create large arrays of CCDs (also called chips in this context), to cover even wider fields of view. The usage of several CCD chips is necessary, as it is not feasible to construct increasingly big single chip CCDs. Due to the more complicated read-out, which happens separately for each chip, this can introduce other problems, for example CCD crosstalk. Additionally, it is not possible to place the different chips right next to each other, but instead there are gaps between chips, which will result in gaps in the image as well. This can be overcome by taking several exposures and slightly moving the telescope between those, which will lead to different parts of the sky being in the chip gaps at each exposure. This is called dithering. Further downsides of CCDs are for example hot pixels or pixel overflow due to the limited capacity of a pixel. A mosaic of the raw images of all 32 chips in OmegaCAM (which will be introduced later in the course of this chapter) is shown in Fig. 4.2.

4.2. Introduction to Crosstalk

In CCD detectors it is possible for a pixel to lose charge after the light exposure, which will show up on the image but at a different location or, in CCD arrays, possibly even at a different chip. This is called crosstalk. A possible scenario is for example the so-called row crosstalk, where during read-out the charge of one well filled pixel gets spread out over the whole row. Another example would be where inside the read-out electronics the currents in physically close wires interact and cause similar effects. Those are unwanted effects, that, especially in astronomy, need to be corrected for. We will now report on a particular case of CCD crosstalk at the Very Large Telescope Survey Telescope (VST) in Chile.

4.3. CCD Crosstalk in OmegaCAM@VST

The VST is a 2.6 m telescope located at Cerro Paranal in Chile and has been specifically designed for wide-field imaging surveys in the optical. As such it is the largest dedicated wide-field survey telescope in the world. Several surveys are being carried out using the VST, among them the Kilo Degree Survey (KiDS, de Jong et al. 2013, de Jong et al. 2015, Kuijken et al. 2015). KiDS makes use of OmegaCAM, a 32 chip CCD-camera that has a field of view of $1\,\mathrm{deg}^2$. The 32 chips are each 4102×2048 pixels big and are placed in a 4×8 grid. The pixel size is $0\farcs213$. As mentioned before, a mosaic of the raw images of each chip can be looked at in Fig. 4.2. Furthermore, this figure shows the different chip numbering schemes, which we will comes across now.

During the course of the data reduction for KiDS many images had to be visually inspected. At this image exploration it was found that there are several chips that apparently interact with each other, which results in artificial objects or "holes" in the image. This is a special kind of crosstalk, in which the flux of one chip gets transferred to another chip. It is especially easy to spot when looking at bright objects at the crosstalk-causing chip and the corresponding pixel positions at the other chip, where the artificial objects and holes will appear. On a small and negligible level this probably happens to all chips in OmegaCAM, but there are a few that show very strong cases of this effect. By visual image inspection it has been found that the chips 25, 26, 27 and in rare cases also 18[1] are having crosstalk interactions with each other. This interaction

---

[1] Note that we are using an internal numbering instead of the official ESO numbering, which is used in Kuijken et al. (2015) where those are the chips 94, 95, 96, and 87. Check Fig. 4.2 for an illustration of this.

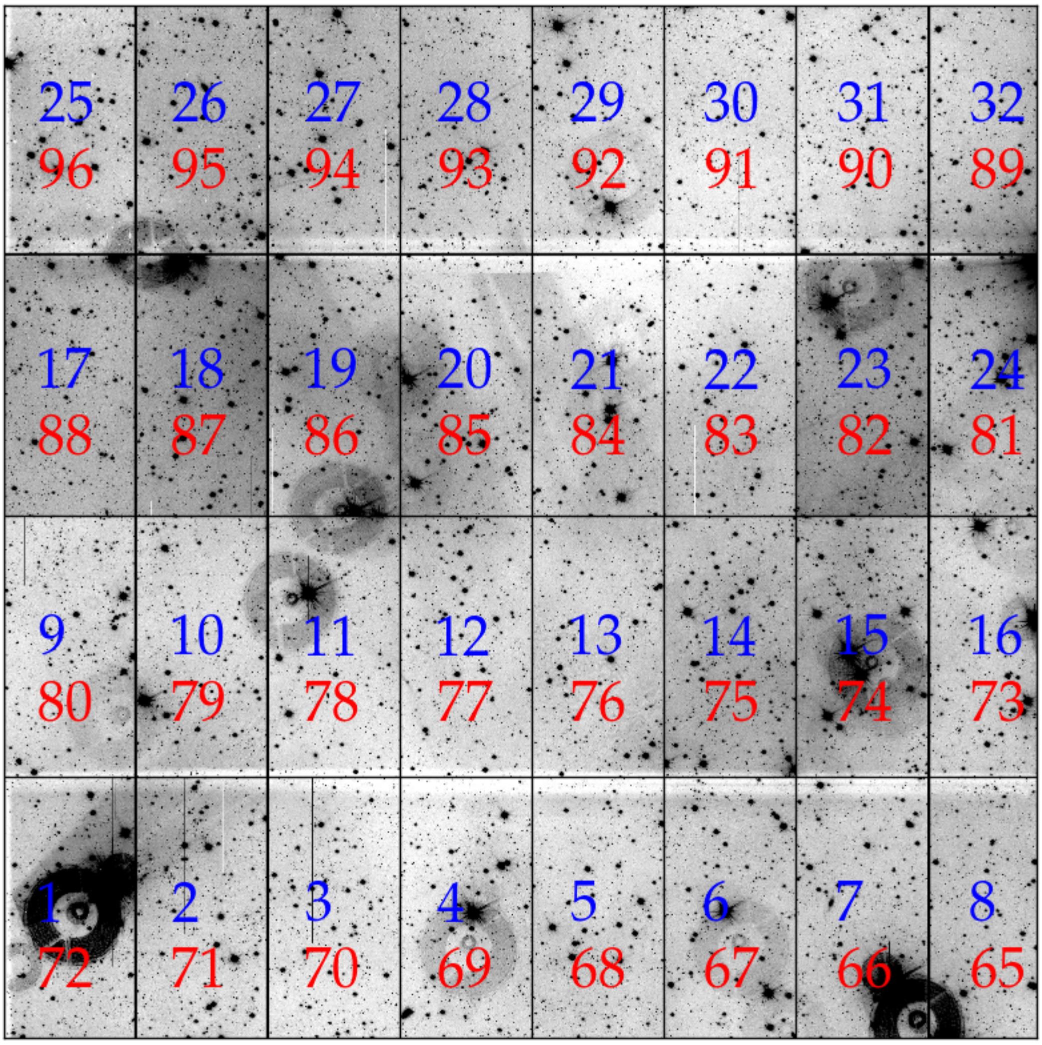

Figure 4.2.: This figure shows a mosaic of all 32 chips in OmegaCAM of a raw image. The red numbers indicate the ESO chip numbering and the blue ones the THELI numbering.

can be positive or negative crosstalk. We talk about positive crosstalk if a bright object at pixel position $\vec{x}$ in chip i causes an artificial object at the same pixel position $\vec{x}$ in chip j. If the bright object instead causes a hole, which has a negative flux, we call this negative crosstalk. The chip that causes the crosstalk with bright objects we call $thief$ (as in the case of negative crosstalk it "steals" flux) and the chip that shows the crosstalk objects we refer to as *robbed*. We find the flux of the artificial objects to be proportional to the flux of the object that causes the crosstalk. Fig. 4.3 shows two exposures with obvious crosstalk.

When we assume that this effect is linear we find an equation to add the missing or subtract the additional flux and thus correct for the crosstalk

$$I_{robbed,\mathrm{cor}}(\vec{x}) = I_{robbed}(\vec{x}) + c_{\mathrm{x}}(robbed, thief) \times I_{thief}(\vec{x})\,. \tag{4.1}$$

Here $I_{robbed,\mathrm{cor}}(\vec{x})$ is the intensity of the crosstalk-corrected image, $I_{robbed}(\vec{x})$ the intensity of the original image, and $I_{thief}(\vec{x})$ the intensity of the $thief$ image. We also defined the crosstalk coefficient c_{x} as the ratio of the flux between the crosstalk objects in $robbed$ and $thief$

$$c_{\mathrm{x}}(robbed, thief) = \frac{S_{robbed}}{S_{thief}}. \tag{4.2}$$

Here S_{thief} is the flux of the crosstalk-causing object, which in our case is always a star in $thief$ and S_{robbed} is the flux of the resulting crosstalk object, either a hole or an artificial object. We use stars for constraining c_{x} as those have the highest fluxes in astronomical images and thus will give less noisy estimates than for example galaxies.

Apart from the fact that the added or subtracted flux will corrupt photometric measurements on the image, especially the added objects will cause problems later on during the data analysis. Thus, a correction scheme needs to be developed. In order to do so we explored a few of the early images of KiDS. During this exploration we discovered several properties of this crosstalk effect. The coefficient c_{x} for example appears to be best measured with bright stars as causing objects. As the flux added or subtracted is always a fraction of the flux in the $thief$ chip at the corresponding position, the resulting crosstalk objects will be brightest (or the deepest holes in case of negative crosstalk) when considering the brightest objects in the $thief$ image, which are stars. On the other hand those stars should not be saturated already (the potential wells in the CCD are overflowing with electrons), as this will lead to a fixed constant flux for the saturated pixels. Thus, the information needed to find the correct c_{x} is lost. Consequently, saturated pixels cannot be corrected properly. Moreover, it was found that c_{x} appears to be roughly constant when measured for multiple stars in the same exposure of one chip (see Fig. 4.4). Unfortunately, it was also found that, although the rough level of the coefficient appears to be always the same (check Table 4.1 to see the default levels found during the data exploration), when considering the coefficient for several exposures over the time scales of hours, days or weeks it is not constant. Variations of up to 50 per cent can be observed. In Fig. 4.5 we show the coefficients for the different crosstalk combinations of the chips 25, 26, and 27 as they vary over a few months. This variation of the coefficients also means that the c_{x} itself needs to be measured on very small times scales, like one KiDS exposure, which is not always possible. As the chips cover only a small fraction of the sky, it is for example not always possible to find suitable stars to determine

Table 4.1.: This table shows all pairs of chips in OmegaCAM that show significant crosstalk. *robbed* and *thief* give the chip number of the chip affected by the crosstalk or causing the crosstalk. The default c_x is the rough level of the coefficient and cut-off gives the upper limits of the coefficients that were found during data exploration.

robbed	*thief*	default c_x	cut-off
25	26	-0.00750	-0.01
26	25	$+0.00400$	0.01
26	27	-0.00035	-0.001
25	27	$+0.00020$	0.001
27	26	-0.00035	-0.001
27	25	$+0.00020$	0.001
25	18	-0.00020	-0.001

c_x from those. Fortunately, we found the coefficients to be constant over the course of one KiDS observing block (OB), which corresponds to five exposures of the same pointing or $\sim 1800\,\mathrm{s}$. For these five exposures it is usually possible to determine the coefficient. If after all it is not possible, we can still fall back to the default level, which has been found during the image explorations. This will still be better than not applying any correction at all. The different levels for the chip pairs are shown in Table 4.1.

In some ways the crosstalk observed in OmegaCAM is special. The specific cause of the crosstalk is for example not known. In many cases crosstalk happens during read-out, outside the CCDs, whereas for OmegaCAM it appears to happen within the CCDs. Moreover, as we mentioned before, the coefficients appear to vary over time, which in other modern cameras is usually not the case, as the crosstalk level there seems to be fairly constant. We will now describe the correction scheme for OmegaCAM, which was designed for the r-band images of KiDS, but has also been tested on the shorter exposures ($t < 100\,\mathrm{s}$) in the u-, g-, r-, i, and z-band from the ATLAS survey (Shanks et al., 2015).

4.4. A Correction for the Crosstalk Problem in OmegaCAM

We can find the amount of flux added or subtracted to the images by measuring the crosstalk coefficient c_x for each chip pair that interacts. We will now briefly describe how these coefficients are measured and how the images are then corrected. The solution described here has been included in the THELI pipeline (Erben et al. 2005; Erben et al. 2013), which is being used for the r-band data reduction of the KiDS data and another small description of this procedure can be found in Kuijken et al. (2015).

Given a pair of crosstalk chips and their default crosstalk-coefficient, we can follow the steps below:

1. We subtract the background of both images. This is technically not necessary, as `SExtractor`

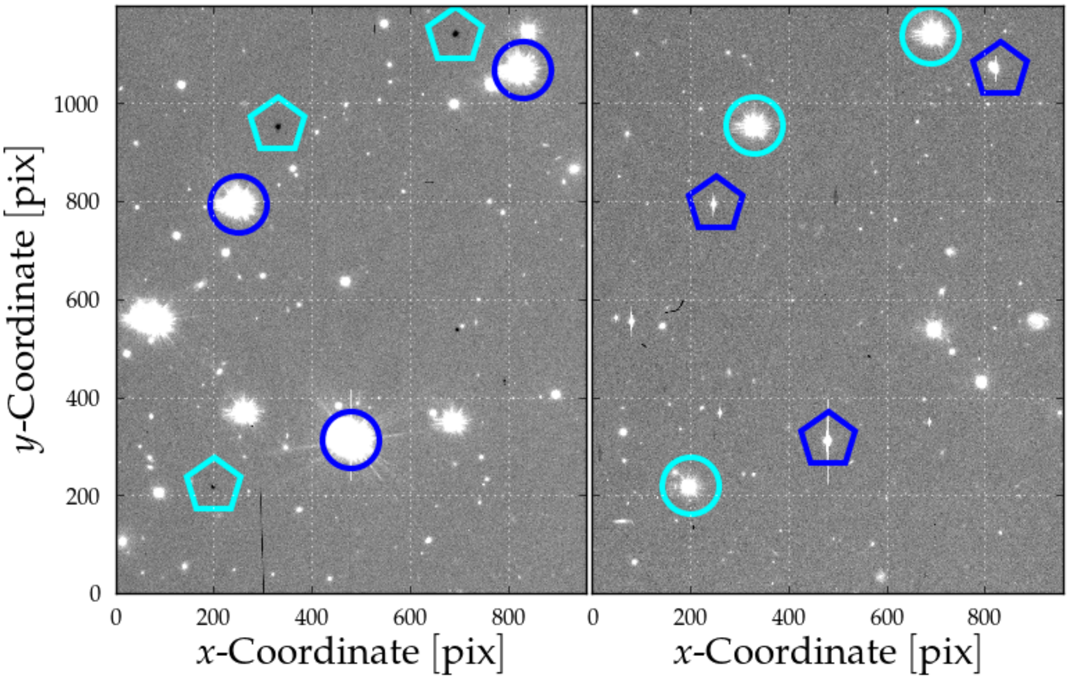

Figure 4.3.: The effect of positive and negative crosstalk on a raw science image. This shows the same part of the chips 25 (left) and 26 (right) with several crosstalk objects. Six of them are specifically marked. The circles show the object that causes the crosstalk, the pentagons the objects that result from the crosstalk. Crosstalk started from chip 25 is marked in blue, in case of chip 26 being the start, it is marked in cyan. We can see the negative crosstalk caused by 26, as well as the positive crosstalk caused by 25.

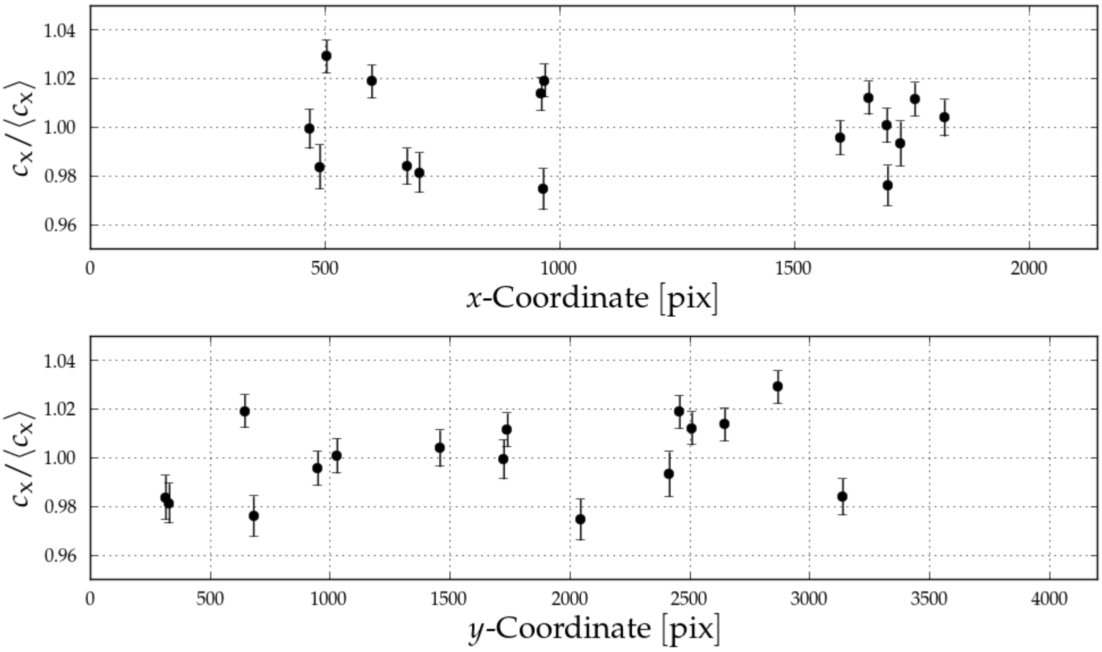

Figure 4.4.: We present the fractional difference between the crosstalk coefficient $c_{\mathrm{x}}(25, 26)$, measured for the stars in one exposure compared to the mean of all stars in this exposure. We show this as a function of x and y location in pixel coordinates. The measured coefficient for single objects does not vary more than 4 per cent from the mean, which is why we conclude that c_{x} is constant across a chip.

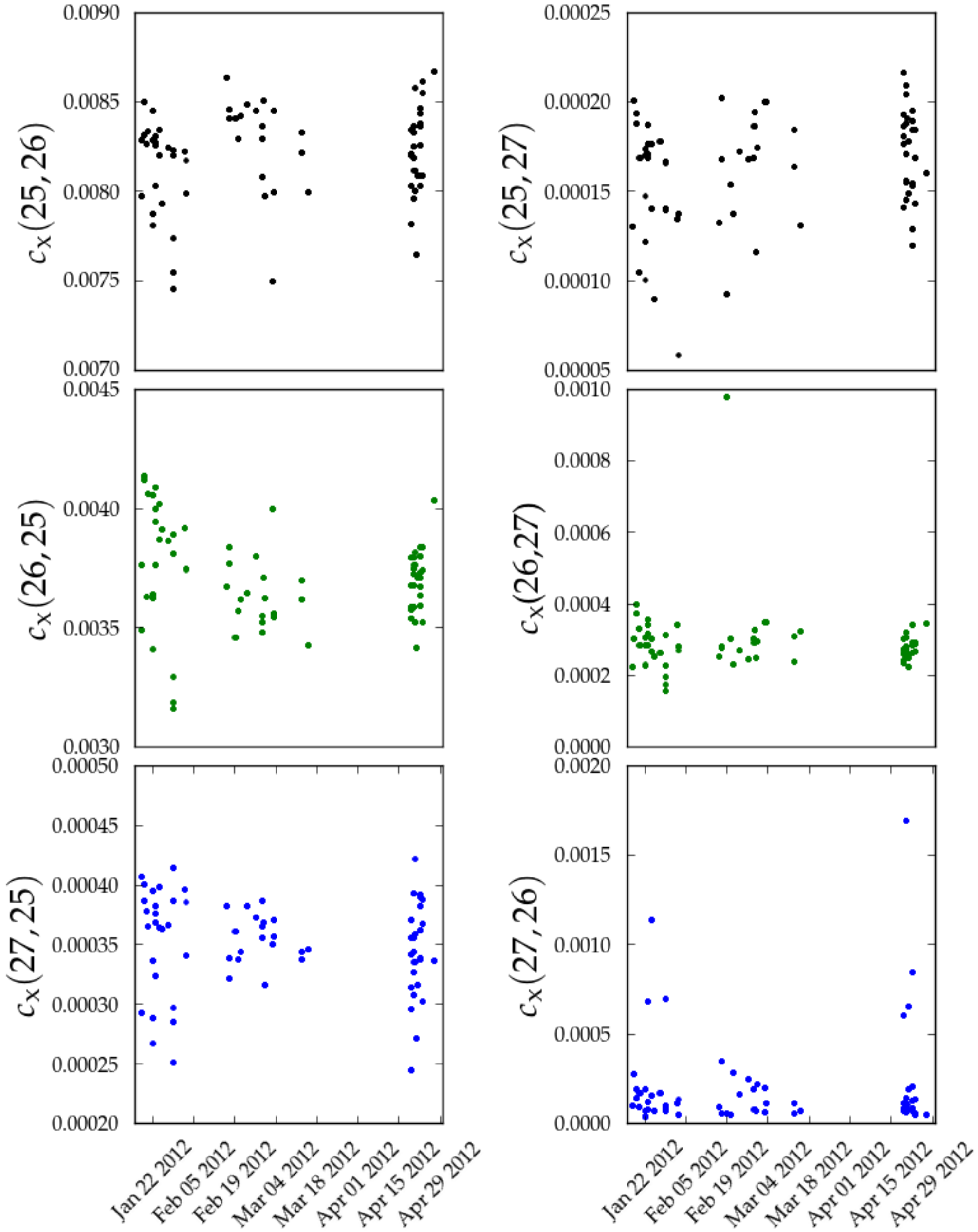

Figure 4.5.: We display the crosstalk coefficients for the chips 25, 26, and 27 over a period of a few months to demonstrate their variability.

(Bertin & Arnouts, 1996) supposedly subtracts the background for all photometric measurements, but in the implementation of this correction scheme this step is still included.

2. We then measure the fluxes of the crosstalk objects in both chips in *SExtractor*'s dual image mode, with $thief$ as the detection image. Dual image mode uses two images, one as a detection image, where it detects objects, and one measurement image, where it measures photometric properties like fluxes or magnitudes at the same pixel position as for the detected objects in the detection image. The assumption here is that both images have the same x and y dimensions and that the same pixel positions in both images correspond to the same sky positions. In our case it is obviously not the case that the same pixels correspond to the same sky positions, as we are using two chips, that map different parts of the sky. Nevertheless, this is an ideal tool to measure the fluxes of the stars in $thief$ and the corresponding artificial crosstalk objects or holes in *robbed* in such a way that we use the exact same object positions for both images. This procedure will result in a catalogue that includes measurements of the stars in $thief$ as well as the crosstalk objects in *robbed*. Especially important are the flux measurements.
3. Afterwards, a signal-to-noise (S/N) cut is applied to the fluxes of the stars in $thief$. We define the S/N as the ratio of the flux S measured as `SExtractor`'s $FLUX\_APER$ and its measurement error ΔS, $S/N = S/\Delta S$. As mentioned before, we are looking for high S/N stars in $thief$ that are not yet saturated, so we can determine the c_x from their fluxes. Obviously, the S/N level needed here depends strongly on the exposure time t. When looking for the ideal cuts for selecting bright, but not saturated stars, we arrived at the following configuration:
   - $t < 100\,\mathrm{s}$: $20\,000 < S/N < 100\,000$,
   - $t \geq 100\,\mathrm{s}$: $10\,000 < S/N < 50\,000$.

   This means that we are eliminating all entries in the catalogue where the star in $thief$ lies outside the given S/N range.
4. As explained before, we know from exploring vast numbers of crosstalk affected images that the level of crosstalk is never higher than the cut-off values given in Table 4.1. However, due to bad object selection, it can happen that for a few objects we find such a high coefficient. Thus, we remove all entries from the catalogue that give obviously wrong values for the coefficient. We determine this by using the cut-off in Table 4.1 as an upper limit.
5. Objects that are within 10 pixels from the artificial crosstalk objects in *robbed*, which are used to determine the coefficient, can corrupt the coefficient estimate. Therefore, we run *SExtractor* again, with *robbed* as the detection image, and check for entries in our catalogues, that are located close to such objects. If this is the case, we remove those entries from the coefficient determination.
6. Although c_x is fairly constant across one chip, we use more than just one object to determine it. This will suppress the noise in the measurement. We decide to use the median of all

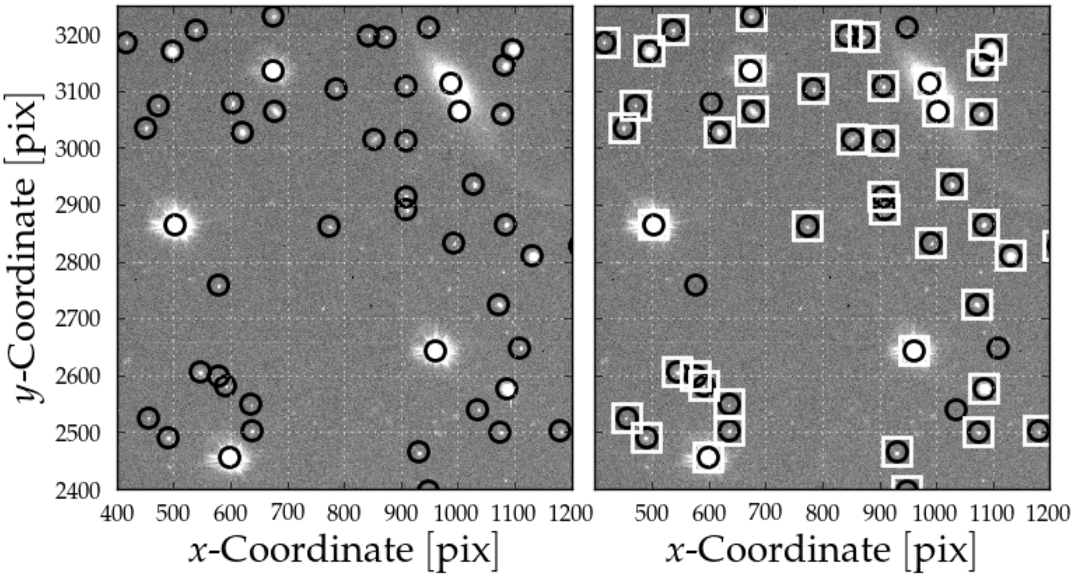

Figure 4.6.: Here we show the detected objects of a simple `SExtractor` run on the uncorrected (left) and the corrected (right) raw image of chip 26. In order to make it easier for the eye, we display only parts of the images. The black circles indicate the detections on the uncorrected image, whereas the white boxes show the detections on the corrected image. One can immediately see the five black circles on the right, that do not have a white box counterpart. This is due to artificial crosstalk objects, that were removed by the crosstalk correction.

measured c_x within one exposure as the estimate for this exposure. The median is chosen as it is less sensitive to outliers than the mean.

7. The mean of the coefficients of all exposures for one OB is then saved as the coefficient to correct all exposures in this OB. Again, taking the mean of all measurements will suppress noise in the measurement.

Given the measured coefficient, we can correct the images by first subtracting the background (this time it is needed as we are taking fractions of the flux in one image, which is affected by the background), then applying Eq. (4.1) and finally adding the background again.

As stated before, due to the limited area of a single chip, it is possible that no stars are present on a chip that fulfil the S/N condition. In this case we either use the last measured value of c_x or, if this is not present either, the default value. Additionally, as we cannot correct for saturated objects, we only flag saturated pixels in the crosstalk chips so that they will not be used for photometry measurements or object detection later on.

In order to briefly demonstrate that the approach of finding c_x is indeed working and necessary, we apply it to the images of chips 25 and 26 of a single exposure. We first determine the coefficient using chip 26 as *robbed* and chip 25 as $thief$ following the steps in the description above, except that we do not average over the measurements of the whole OB, as for simplicity we are only using one single exposure. After the coefficient has been determined we apply Eq. (4.1) to the image of chip 26. Subsequently, we conduct a simple `SExtractor` run, using the default configuration, to check the number of detected objects in the uncorrected and the corrected image of chip 26. For the uncorrected image we find 573 objects, whereas for the corrected one we find only 542 objects. This is expected as bright objects in chip 25 will result in artificial crosstalk objects in chip 26. After the correction has been applied, those objects should have vanished, thus the lower number of detections. Parts of the uncorrected and the corrected images of chip 26 and the corresponding object catalogues are displayed in Fig. 4.6. This is of course only a simplified experiment, in which we did not take into account the more complicated aspects of object detection, as for example weight images. Nevertheless, it demonstrates in a neat way that crosstalk introduces artificial objects, which will be picked up during the source detection process. Consequently, it is possible that those objects get propagated further into the analysis, which can possibly lead to biases in or corruption of the scientific results.

As mentioned before, this approach has been implemented and is part of the KiDS weak lensing data production (Kuijken et al., 2015).

Bibliography

Bertin E., Arnouts S., 1996, A&AS, 117, 393

de Jong J. T. A. et al., 2013, The Messenger, 154, 44

de Jong J. T. A. et al., 2015, ArXiv e-prints: 1507.00742

Erben T. et al., 2013, MNRAS, 433, 2545

Erben T. et al., 2005, Astronomische Nachrichten, 326, 432

Kuijken K. et al., 2015, ArXiv e-prints: 1507.00738

Rieke G., 2003, Detection of Light - From the Ultraviolet to the Submillimeter. Cambridge University Press

Shanks T. et al., 2015, MNRAS, 451, 4238

CHAPTER 5

Optical & Sunyaev-Zel'dovich Observations of a New Sample of Distant Rich Galaxy Clusters in the *ROSAT* All Sky Survey

This chapter is based on Buddendiek et al. (2015), published in *Monthly Notices of the Royal Astronomical Society*, Volume 450, Issue 4, p. 4248-4276.

5.1. Introduction

This work is meant to be a continuation of the still ongoing search for massive galaxy clusters at high redshift. By cross-correlating the positions of red galaxies in the Sloan Digital Sky Survey (SDSS) and the faint and bright source catalogues of the *ROSAT* All Sky Survey (RASS), we create a new sample of distant ($z > 0.6$) and possibly massive cluster candidates, making use of the wide area of the SDSS Data Release 8. Because red galaxies are known to reside preferentially in clusters, this is a useful approach to identify massive clusters from the RASS catalogues which are strongly contaminated with other X-ray sources (for example AGN or binary stars). Through follow-up observations using the William Herschel Telescope (WHT), the Large Binocular Telescope (LBT), and the Combined Array for Research in Millimeter Astronomy (CARMA), we then confirm or reject our candidates and check for consistency with ΛCDM. This study presents one of the first systematic searches for massive high-redshift galaxy clusters in the optical and X-ray regimes in a very large volume. Similar approaches to detect clusters have been used for eMACS (Ebeling et al., 2013), which also uses RASS data but for the optical part it makes use of deeper imaging data from the Pan-STARRS Medium Deep Survey, which is part of the Pan-STARRS project (Kaiser et al., 2002). Also, the aforementioned work by Brodwin et al. (2015) searches for high redshift clusters in data from the Wide-Field Infrared Survey Explorer (*WISE*) satellite (Wright et al., 2010). Instead of cross-correlating with optical data, they use a non-detection in the SDSS as an indication for a high-redshift cluster.

One should note that we do not intend to use our sample for cosmological cluster abundance studies. By specifically following up the most extreme candidates, we compromise a simple selection function. Nonetheless, it is one of the largest samples of very X-ray-luminous high-redshift galaxy clusters in the northern hemisphere making it complementary to the cluster samples found by *Planck*, SPT, and ACT. The distribution of all clusters in our sample on the sky is plotted in Fig. 5.1.

In Section 5.2, we first describe how we define our cluster sample. We then explain the data from follow-up observations and the instruments which were used for those campaigns in Section 5.3. This is followed by a detailed description of the red sequence and richness analysis and their interpretation in Section 5.4. We describe the SZ data analysis in Section 5.5. In Section 5.6 we discuss possible tensions of our cluster sample with ΛCDM and in Section 5.7 properties of some individual clusters. This is followed by our conclusion. Images showing postage stamps of all 47 clusters, including three previously discovered objects, as well as SZ-maps from CARMA and *Planck* data can be found in Section 5.C, 5.D, and 5.E.

As our fiducial cosmology we use $H_0 = 70\,\mathrm{km/Mpc/s}$, $h = 0.7$, $\Omega_{\Lambda,0} = 0.7$ and $\Omega_{\mathrm{m},0} = 0.3$. The exclusion plots in Section 5.6 were created assuming $\sigma_8 = 0.83$ as has been done in Mortonson, Hu & Huterer (2011).

5.2. Preselection of cluster candidates

To find some of the most massive clusters at redshifts $0.6 \lesssim z \lesssim 1.0$, we use the combined bright and faint source catalogues of RASS (Voges et al. 1999[1]; Voges et al. 2000[2]), which is an X-ray all sky survey in the $0.1 - 2.4$ keV range carried out with the ROSAT satellite. This combined catalogue contains 125 000 entries with typical positional uncertainties of $20''$. Most of these objects are not galaxy clusters but rather AGN or X-ray binaries. Hence, to identify distant galaxy clusters, more information is needed. For that we combine the X-ray data with imaging data from the SDSS (Castander, 1998), where we used Data Release 8 (Aihara et al., 2011). By cross-correlating the RASS object positions with the position of SDSS galaxies for which the SDSS photometry suggests that they likely match the targeted redshift range, we are able to efficiently preselect candidates for galaxy clusters. Here we generally use a $50''$ matching radius, which should account for the positional uncertainty in RASS and for the fact that galaxies scatter around the cluster centre. Note that we did not employ a radius in projected physical separation given the photometric redshift uncertainties and the small change in projected radius of only

---

[1] `http://www.xray.mpe.mpg.de/rosat/survey/rass-bsc/`

[2] `http://www.xray.mpe.mpg.de/rosat/survey/rass-fsc/`

about 50 kpc between $z = 0.6$ and $z = 0.9$. Photometric redshifts are taken from the `Photoz`-table in the SDSS archive. We then employ two different SDSS galaxy selection schemes: In the first scheme we select all SDSS galaxies with a photometric redshift $z > 0.6$ and $i < 20.5$. This yields 1149 matches of RASS sources with two or more SDSS DR8 galaxies, mostly at $0.6 \lesssim z \lesssim 0.8$. At higher redshifts we expect that possibly only a single cluster galaxy (the BCG) is detected in SDSS. We select candidates for such galaxies photometrically from SDSS with colour cuts $r - i > 0.5$, $i - z > 0.8$, and $17 < i < 21$ (compare e.g. High et al. 2010). While requiring a match of at least one of these galaxies in the SDSS DR8 with the RASS sources and adding these cases to our preselected sample, we find 1395 candidates in total.

In the next step all candidates are visually inspected using SDSS postage stamps and graded. Here we immediately drop obvious chance alignments of background galaxies e.g. with bright foreground stars, spectroscopically classified QSOs, or low-z galaxy groups, which most likely dominate the X-ray flux. In addition, we drop sparse galaxy groups/clusters, where the SDSS colours suggest $z \sim 0.6 - 0.7$. At these redshifts we would still expect to detect numerous cluster galaxies in SDSS if these were massive clusters. Hence, these sparse groups/clusters likely have an X-ray flux boosted by an AGN and are not of interest for our study. The remaining candidates are graded in preparation for further follow-up observations (Section 5.3), where we prioritise the richest systems as well as good candidates for the highest-redshift clusters ($z \gtrsim 0.8$) in our sample. We attempted optical follow-up observations for a total of 80 candidates. From these 48 have data of sufficient quality in the three filters r, i, z, constituting the sample we analyse in this paper. This includes all of the top-graded candidates. For 8 of the remaining candidates, single band observations were sufficient to identify them as false positive. The remaining 24 candidates, which were all of lower or medium priority, were dropped from the current analysis, as they do not have observations of sufficient quality in all three bands. This was due to observations attempted under poor conditions, guiding errors, or limited target visibility. Within the allocated time these observations could not be completed or repeated, but we ensured to complete the observations for all of the highly-graded candidates.

With our automated pre-selection we also 'rediscovered' the known massive clusters MACSJ0744.8+3927 ($z = 0.6976$, Ebeling et al. 2007), MACSJ2129.4−0741 ($z = 0.5889$, Ebeling et al. 2007), and RCS2-J232727.7−020437, ($z = 0.705$, Menanteau et al., 2013), providing a confirmation of our algorithm and a reference sample of massive clusters in the targeted redshift range.

5.3. Follow-up observations

5.3.1. Optical images

William Herschel Telescope

The majority of our optical follow-up observations were taken with the Auxiliary-port CAMera (ACAM) (Benn, Dee & Agócs, 2008) on the 4.2-m William Herschel Telescope on the island of La Palma in Spain. ACAM is a red-optimised one chip camera with 2148 × 2500 pixels which has an unvignetted circular field of view of about $8'$ in diameter and a pixel scale of $0\farcs25$.

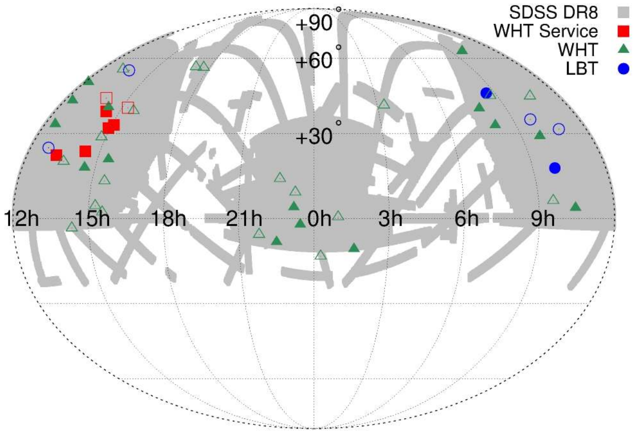

Figure 5.1.: This plot shows the distribution of all clusters of our sample on the sky. Open symbols indicate clusters with unknown spectroscopic redshift. Our search for clusters makes use of about one quarter of the whole sky.

Our WHT data were taken in service mode (August 2010 and August 2013, PIs Schrabback and Buddendiek, respectively), and in visitor mode (four nights each in August 2011 and March 2012, PI Schrabback). We obtained imaging in r, i, and z filters, which bracket the 4000 Å-break in the redshift range of interest. The service observations in 2010 were carried out with the RGOZ2 filter ($\lambda_{\mathrm{central}} = 8748\,\mathrm{\AA}$) as the SDSS z-band was not yet available. Therefore we need to create different red sequence models for those images later on. Our total exposure time per cluster candidate per filter varies between 360 and 1800 seconds, this choice primarily depends on observing conditions and the roughly estimated cluster redshift. For some of the candidates for the highest-redshift clusters in the sample – which typically were the most uncertain candidates with only a single noisy BCG candidate – we stopped observing after taking data in a single filter (i or z) if these data clearly showed that this was a spurious match (e.g. a faint red star misclassified as galaxy in SDSS). In total we obtained 3-band imaging for 42 cluster candidates with ACAM, plus 3 previously known clusters with spectroscopic redshifts which were included as reference objects for the generation of the red sequence model (see Table 5.1).

Large Binocular Telescope

We observed nine cluster candidates using the 2 × 8.4-m Large Binocular Telescope in Arizona during observations in October and December 2010, as well as February and April 2011 (PI: Eifler). Two of these candidates were also observed with the WHT. Here we employed the r-, i- and z-filters, which are similar to the WHT filters used. The instruments used were LBC_RED (i- and z-band) and LBC_BLUE (r-band) (Giallongo et al., 2008). Those cameras have four 2048 × 4608 pixel chips each, a pixel scale of $0\overset{\prime\prime}{.}23$ and a field of view of about 24×25 arcmin^2.

A single chip covers roughly 17×8 arcmin^2.

Total exposure times per filter for the LBT data are between 360 and 720 seconds, depending on the object. Single exposures were integrated for 180 seconds regardless of the filter in use.

5.3.2. Spectroscopic observations

We obtained long-slit spectroscopic data for 14 clusters with ACAM during the visitor mode WHT runs listed in Sect. 5.3.1, plus one cluster as part of a WHT service program in June 2014 (PI: Buddendiek). Targets were selected for the spectroscopic observations either if they appeared to be very rich, at very high redshift or if they seemed relaxed due to a single very bright BCG. Integration times varied between 600 s and 1100 s per exposure, which results in total integration times between 1800 s and 3300 s per target. In all cases we employed the V400 grating and the G495 filter, which provides a wavelength range from 4950 Å to 9500 Å and 3.3 Å/pixel. The slit width is $1\farcs0$, corresponding to a resolution of $R = 570$ at a wavelength of $\lambda = 7500\,\text{Å}$. For three clusters the spectra are too noisy and no redshift could be estimated. We generally placed the slit on top of the BCG and if possible oriented it so that other cluster members were visible through the slit as well.

5.3.3. Data reduction and calibration

The WHT and LBT data are reduced using the GUI version of the THELI[3] pipeline (Erben et al. 2005; Schirmer 2013). We apply bias subtraction, flat field correction, and superflat field correction. Exposures are co-added and later convolved with a Gaussian kernel to have approximately the same resolution in all bands for photometric measurements.

We calibrate the photometry by fitting the function

$$\mathrm{mag}_{\mathrm{SDSS}} - \mathrm{mag}_{\mathrm{m}} = \mathrm{C}_{\mathrm{SDSS}} \cdot \mathrm{CT} + \mathrm{ZP} \tag{5.1}$$

to field stars. $\mathrm{mag}_{\mathrm{m}}$ is the measured magnitude, $\mathrm{mag}_{\mathrm{SDSS}}$ the corresponding SDSS magnitude, CT the colour term and ZP the magnitude zero point. $\mathrm{C}_{\mathrm{SDSS}}$ is the SDSS colour we use for calibration, either $r - i$ (r- and i-band calibration) or $r - z$ (z-band calibration). After correcting magnitudes with the zero points we do not apply a colour correction but work in the instrumental system instead. Every single field is corrected independently. The data reduction for WHT and LBT data is performed in the same way.

In order to determine the limiting magnitude of a co-added image we use

$$m_{\mathrm{lim}} = \mathrm{ZP} - 2.5 \log \left(5 \sqrt{\mathrm{N}_{\mathrm{pix}}} \sigma_{\mathrm{sky}} \right) \ , \tag{5.2}$$

where N_{pix} is the number of pixels within a circle with a radius of $2\farcs0$ and σ_{sky} is the variation of the sky background noise (see Erben et al. 2009). This gives the 5σ detection limit. We find the mean limiting magnitudes of the WHT images to be $r_{\mathrm{lim}} = 23.81\,\mathrm{mag}$, $i_{\mathrm{lim}} = 23.42\,\mathrm{mag}$ and $z_{\mathrm{lim}} = 22.64\,\mathrm{mag}$. We also measure the seeing as the `FWHM` and find the median seeing

---

[3] `http://www.astro.uni-bonn.de/~theli/index.html`

$\texttt{FWHM}_r = 0\farcs95$, $\texttt{FWHM}_i = 0\farcs82$ and $\texttt{FWHM}_z = 0\farcs82$. For the LBT data we find $r_{\rm lim} = 24.52\,$mag, $i_{\rm lim} = 24.95\,$mag, $z_{\rm lim} = 23.63\,$mag and $\texttt{FWHM}_r = 0\farcs77$, $\texttt{FWHM}_i = 0\farcs92$, $\texttt{FWHM}_z = 0\farcs77$.

The spectra are also bias subtracted, flat fielded and then extracted. For the further reduction we use IRAF (Tody, 1993). We extract the spectra using the task `apall`. Furthermore, wavelength and flux calibration are performed with the tasks `identify`, `dispcor` and `calibrate` using skylines and standard star observations.

5.3.4. Sunyaev-Zel'dovich data

To obtain cluster mass estimates, we targeted a sub-sample of 21 targets with the Combined Array for Research in Millimeter Astronomy to measure the Sunyaev-Zel'dovich effect signal, which has been found to correlate with mass with small intrinsic scatter, both from simulations (e.g. da Silva et al. 2004; Motl et al. 2005; Stanek et al. 2010) and observations (e.g. Bonamente et al. 2008; Planck Collaboration et al. 2011; Marrone et al. 2012; Planck Collaboration et al. 2013).

The SZ data for 20 of those clusters were obtained using the eight 3.5 m telescopes of CARMA in the SH and SL configurations. For these configurations, 6 telescopes are grouped in a compact central array and two on outlying pads. The long baselines resolve out the cluster signal and yield uncontaminated measurements of point sources, which can then be subtracted from the short baseline data. We used the CARMA wideband correlator with 8 GHz of correlation bandwidth. Observations were carried out in the 30 GHz band and integration times were planned to be 8 h for each cluster. Due to various reasons the 8 h were not always reached. The exact integration times can be found in Table 5.4. The CARMA program numbers are `c0734`, `c0734Z` (both PI: Schrabback) and `c0934` (PI: Plagge). Those targets were selected because they appeared to be the richest or most distant objects in the sample. Additionally, we also have been granted director's discretionary time for the target ClG-J122208.6+422924 (`cx389`, PI: Buddendiek). This data set was recorded using an antenna configuration different from the SL and SH configurations. All 3.5 m-antennas were grouped in a compact array and the 6 m and 10 m antennas are used for long baselines.

The first 20 targets were selected after an initial optical analysis because they appeared to be either the richest, the most X-ray luminous or the highest redshift ones. One should note that at that time the optical campaign was not complete yet. The last of the 21 targets was selected after the optical analysis had been completed and it had a measured spectroscopic redshift greater than 1, which is the highest in the whole sample.

5.4. Optical Data Analysis

5.4.1. Spectroscopic redshifts

After extracting the spectra, we use the IRAF task `fxcor` (Fitzpatrick, 1993) in order to cross-correlate them with the absorption line template spectrum `fabtemp97` and the emission line template spectrum `femtemp97`. This yields the redshift estimates. In order to find the uncertainty `fxcor` fits a Gaussian to the correlation peak and we then take the half width at half maximum as the redshift error. Visually identified lines and features can be found in Table 5.1.

The spectra are mainly low S/N spectra due to very faint targets. The redshifts are mostly estimated using absorption features like the Ca K+H doublet, thus the errors for the redshifts are comparably high (≈ 0.5 per cent). Individual errors can be found in Table 5.1.

In our analysis we also include the already known redshifts of twelve galaxy clusters. Those were taken either from the SDSS Data Release 10 (Ahn et al., 2014) or from other independent discoveries. In one of those cases (ClG-J131339.7+221151) a spectrum from the SDSS was available, but no reliable redshift has been estimated ($z_{\mathrm{SDSS}} = 1.000 \pm 3.359$); we downloaded the already reduced and extracted spectrum and estimated the redshift ourselves. All redshifts used in this study are listed in Table 5.1, which also includes additional information.

Table 5.1.: The spectroscopic sub-sample. Spectroscopic redshifts are either measured from our data, taken from independent discoveries or from the SDSS DR 10. If z_{spec} was measured, the spectroscopic features which were identified by visually inspecting the spectra are listed. For ClG-J131339.7+221151 we downloaded one spectrum from the SDSS database and determined the redshift ourselves, because the estimate taken from SDSS proved not to be trustworthy ($z_{\text{SDSS}} = 1.000 \pm 3.359$).

Object	Redshift	Lines	# Spectra	Ref.
ClG-J013710.4−103423	0.662±0.002	Ca H+K, 4000Å	1	-
ClG-J031924.2+404055	0.680±0.003	Ca H+K, 4000Å	1	-
MACSJ0744.8+3927[a]	0.698	-	-	Ebeling et al. (2007)
ClG-J080434.9+330509	0.553	-	1	SDSS
ClG-J083415.3+452418	0.666	-	1	SDSS
ClG-J094700.0+631905	0.710	-	1	SDSS
ClG-J094811.6+290709	0.778±0.002	Ca H+K, 4000Å	1	-
ClG-J095416.5+173808	0.828	-	-	Nastasi et al. (2014)
ClG-J102714.5+034500	0.749±0.003	Ca H+K, 4000Å	1	-
ClG-J120958.9+495352	0.902±0.001	[OII], Ca H+K	1	-
ClG-J122208.6+422924	1.069±0.003	Ca H+K, 4000Å	2	-
ClJ1226.9+3332[a]	0.892	-	-	Ebeling et al. (2001)
ClG-J131339.7+221151	0.737±0.002	Ca H+K, 4000Å	1	SDSS
ClG-J142040.3+395509	0.607	-	-	Bayliss et al. (2011)
ClG-J142138.3+382118	0.762	-	1	SDSS
ClG-J142227.4+233739	0.726	-	1	SDSS
ClG-J143411.9+175039	0.744±0.003	Ca H+K, 4000Å	1	-
ClG-J145508.4+320028	0.654	-	1	SDSS
ClG-J150532.2+331249	0.758	-	1	SDSS
ClG-J152741.9+204443	0.693±0.002	Ca H+K, 4000Å	1	-
ClG-J223007.6−080949	0.623±0.003	Ca H+K, 4000Å	1	-
ClG-J231215.6+035307	0.648±0.003	[OII], Ca H+K, 4000Å	4	-
RCS2-J232727.7−020437[a]	0.705	-	-	Menanteau et al. (2013)

---

[a] These clusters were known before and are only included in the sample for calibration reasons.

5.4.2. Red sequence finding and redshift estimation

We derive empirical red sequence models in $r-i$, $i-z$ and $r-z$ using twelve clusters from the WHT sample with known spectroscopic redshifts. For this we use the colour-magnitude diagram of galaxies within the inner $50''$ around the BCG. Again, we employ a constant angular radius and not a physical one given the small change in the angular diameter distance between $z=0.6$ and $z=0.9$.

Within this radius, we fit a linear function of galaxy colour vs. magnitude as a red sequence yielding slope and offset. We then assume that red sequence slope and offset change linearly with redshift and thus fit both as a linear function of z. Using these fits, we can derive an empirical red sequence model for every redshift in the range $0.5 \lesssim z \lesssim 0.9$. Additionally, we extrapolate these models to $z=0.4$ and $z=1.0$. We are aware that the red sequence slope and offset do not in general vary linearly with redshift. Nevertheless, this assumption provides a good approximation given the redshift range and filter choice. The models created can be used for both the WHT and the LBT sample, because their filter sets are fairly similar; for the service observations in 2010, we create models in the same way but using different clusters, due to the different filters used. The clusters used to create the models for the WHT and LBT samples spread almost evenly in the redshift range between $z \approx 0.55$ and $z \approx 0.9$. For the models for the WHT service observations, we only have redshifts available between $z \approx 0.6$ and $z \approx 0.8$. Later on in this section, we will find these models to be sufficient for our purposes (see Fig. 5.2).

We create the galaxy catalogue with aperture photometry in dual image mode, using the i-band as the detection image. Due to the homogenised PSF, we suppress background noise and thus underestimate the photometric errors. To avoid this issue, we run `SExtractor` (Bertin & Arnouts, 1996) again on the unconvolved images and use those magnitude errors. Nevertheless, we find that we still underestimate the photometric errors due to multiple reasons. For example, during the reduction we resample the images to a new pixel grid, which correlates the background noise. This has a similar effect as the PSF homogenisation. We also use aperture photometry, which can lead to additional photometry errors, in case of a not completely homogeneous PSF in all three filters. In order to account for this, we take the photometric errors from `SExtractor` to be twice as large as the original value. A factor of 1.3 is due to noise correlations, the remaining due to uncertainties arising from the limitations in the PSF homogenisation. This is performed by assuming Gaussian PSFs and by quantifying the PSF using the flux radius, which is not a complete description of the PSF. In the end, this results in a total correction factor of 2. Using the newly created models, we find the red sequence and the corresponding redshifts by taking the following steps, which are similar to the approach used in High et al. (2010):

First, we identify the BCG in the colour image. We then use all galaxies, which are within a given radius R around the BCG. Additionally, we only take galaxies with a S/N larger than six in the i-band into account. Between redshifts 0.4 and 1.0, we proceed in steps of $\Delta z = 0.025$ and use the corresponding red sequence model to look for galaxies in the catalogue which lie within a certain error range in colour, Δc, from the red sequence lines in all three colours. Here we also use galaxies, even if they only fall within that range, when taking their magnitude errors into account. Although we only use the inner parts around the cluster centre, we are still affected by fore- and background galaxies, which are contaminating the colour-magnitude diagram. In order to avoid false detections through these galaxies, we determine and subtract an average red sequence background. Since the ACAM field of view is fairly small, we use about 100 apertures in the public CFHTLenS catalogue (Erben et al. 2013; Hildebrandt et al. 2012), using the same cuts as for the actual galaxy catalogues in order to estimate the mean red sequence object density. After normalising by the projected area and subtracting the background, we choose the redshift bin which contains the most galaxies to be our red sequence redshift estimate. The error range Δc, and the aperture radius R are free variables, which can be chosen arbitrarily. We explore the parameter space spanned by those two parameters, looking for the combination which recovers the known spectroscopic redshifts best. Although we vary the radius R for each cluster, we find that the best choice for all the WHT objects is $R = 1\overset{\prime}{.}25$ and $R = 0\overset{\prime}{.}76$ for all the LBT targets. While looking for the red sequence for every cluster candidate we maximize the signal by varying Δc in discrete steps between 0.01 and 0.2. In the end, for each cluster we pick the value, which leads to the strongest signal. A typical value here is $\Delta c = 0.08$.

We plot the estimated spectroscopic redshifts against their measured photometric counterparts for the best configuration of R and Δc. As can be seen in Fig. 5.2, no systematic bias is present, and on average the red sequence redshift estimates agree with the spectroscopic ones. Thus, we decide not to calibrate the estimates further.

The comparison with the spectroscopic sample shows that the models work fine as we find $\sigma_z = 0.037$, which we define as

$$\sigma_z = \sqrt{\frac{1}{N} \sum \left(\frac{z_{\text{spec}} - z_{\text{phot}}}{1 + z_{\text{spec}}} \right)^2}\,, \tag{5.3}$$

where N is the number of galaxy clusters with a known spectroscopic redshift and z_{spec} and z_{phot} is their corresponding spectroscopic or red sequence redshift.

We also try building analytical models from Bruzual & Charlot (2003), taking into account filter curves, quantum efficiency, and reflection curves of all optical elements inside the telescope, but we found that, especially at the low- and high-redshift regions in our sample, the redshift estimation failed completely. These models apparently do not match the observed galaxy distribution over the whole redshift range. Already Hildebrandt et al. (2010) showed that photometric redshift codes, which are tested on a suitable training sample, usually work best while using empirical models. In the end, we decided to use the empirical models rather than the analytical ones.

A colour image of a typical cluster, a background subtracted histogram of possible red sequence members, the red sequence corresponding to the photo-z estimate, and also the number counts (Section 5.4.3) can be seen in Fig. 5.3.

We estimate statistical errors from bootstrapping the whole galaxy catalogue and estimating the redshift several thousand times. To the standard deviation of the distribution, which is the statistical error, we quadratically add the magnitude zero point error, which gives a fair estimate of the photometric error, and take this as the red sequence redshift uncertainty. We check if this is indeed a fair representation of the true uncertainty by computing the standard deviation, Δz, of $z_{\text{spec}} - z_{\text{phot}}$ and comparing it with the mean redshift error $\langle \Delta z \rangle$. We find $\Delta z = 0.048$ and $\langle \Delta z \rangle = 0.044$. This means that on average Δz is a good representation of the true redshift

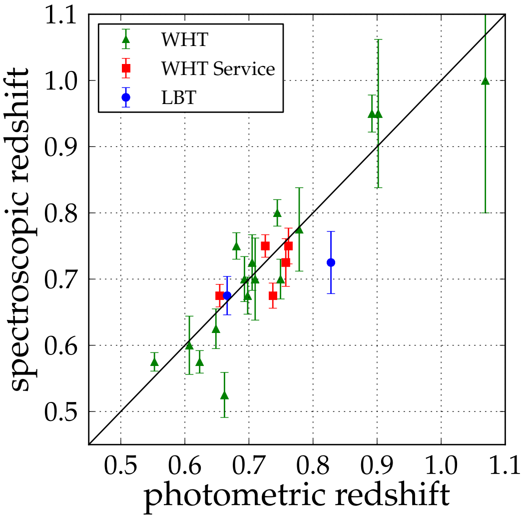

Figure 5.2.: Comparison of spectroscopic vs. red sequence redshifts of galaxy clusters. Error bars represent statistical errors and photometric errors, which originate from the photometric calibration. The black line shows the one on one relation. No systematic bias seems to be present.

uncertainty.

Defining a detection

After running our red sequence finder on the data of all 48 cluster candidates, which have three band imaging, we define a detection using two criteria:

1. The object shows a peak in the red sequence histogram (see Fig. 5.3, top right panel).
2. In the three colour image, we can visually find an overdensity of galaxies, which have the same colour.

If both these criteria are true, we consider this a detection and continue the analysis. If only one or none are true, we stop the analysis after the red sequence finding and consider this a non-detection. From the 48 cluster candidates, we detect 44 according to these criteria. The three previously known clusters are detected as well.

5.4.3. Richness estimates

We define the richness N_{gal} to be the number of cluster galaxies within 0.5 Mpc around the BCG, which are brighter than some characteristic magnitude of the cluster luminosity function. We will now describe the procedure to estimate N_{gal}.

Once the red sequence redshift was estimated, we created new catalogues with all galaxies which were detected as a red sequence member in all three colours at this redshift. For the aperture radius r, we now choose 0.5 Mpc. The galaxies are divided in magnitude bins of size 0.5 mag between 19th and 24th magnitude in the i-band and normalised to the area. Again, a background is estimated from CFHTLenS and subtracted. We then fit a Schechter function (Schechter, 1976) normalised to projected area rather than volume to the data

$$\phi(m)\mathrm{d}m = 0.4 \ln 10\, \phi^* \, 10^{-0.4(m-m^*)(\alpha+1)} \exp[-10^{-0.4(m-m^*)}]\mathrm{d}m \; . \tag{5.4}$$

For the fit, we keep α fixed to -1.1, which has been shown to be robust for rich clusters (e.g. Paolillo et al. 2001). Furthermore, we assume passive stellar evolution and use the stellar population synthesis models from Bruzual & Charlot (2003) with the Padova stellar evolution models (Bertelli et al., 1994) and the initial mass function by Chabrier (2003) to fix m^* for every redshift. In the end, we only fit the normalisation ϕ^*. Subsequently, we integrate the Schechter function up to $m^* + 2$. After multiplying the result with the projected area, this gives us our richness estimate, N_{gal}. An example of such a measured function can be found in the bottom right panel of Fig. 5.3.

We estimate statistical errors for the richness by bootstrapping the cluster member sample and repeating the whole estimation procedure several thousand times. We then quadratically add the Poissonian error and take this as the total uncertainty in richness. For comparison, we also estimate the richness of a cluster by counting the red sequence galaxies that are brighter than $m^* + 2$ and call this N_{count}. Here we take the Poissonian error as the uncertainty. For the further analysis we use only the N_{gal} estimates, because we expect them to be more robust.

Redshifts, richnesses, and other properties as well as comments concerning the data and the analysis can be found in Table 5.3.

5.4.4. Discussion of the results from the optical data

With our analysis, we confirmed 44 galaxy clusters at redshifts between $0.5 \lesssim z \lesssim 1.0$. Additionally, we conducted the analysis for three previously known clusters in order to have a calibration sample. The cluster richnesses within 0.5 Mpc vary between 3 and 46. We summarise all measured quantities in Table 5.3. One column in this table lists problems that occurred during the analysis. Those problems were poor observing conditions like high airmass, cloud coverage etc., which lead to considerable systematic uncertainties. Furthermore, the galaxy redshift distribution in the histograms like the one shown in Fig. 5.3 does not always have a clear peak, sometimes it is bimodal. Additionally, the Schechter function fit can fail, which can for example be caused by a poor redshift estimate due to a faint cluster. An example for this is ClG-J094742.3+351742. From the fit we find $N_{\mathrm{gal}} = 20 \pm 4$, which does not agree with the counted estimate of $N_{\mathrm{count}} = 2 \pm 1$. Poor data in one or more bands can also lead to poor richness estimates. The r-band of ClG-J144847.4+284312 for example is much shallower than the rest of the data, because it was observed in bright time. Due to this we overestimate the background in this field, which leads to the low values in $N_{\mathrm{gal}} = 3 \pm 2$ and $N_{\mathrm{count}} = 3 \pm 2$.

The redshift and richness distribution of our sample can be found in Fig. 5.4. The redshift distribution peaks at $z = 0.75$. We targeted a redshift range of $0.6 \lesssim z \lesssim 1.0$ while cross-

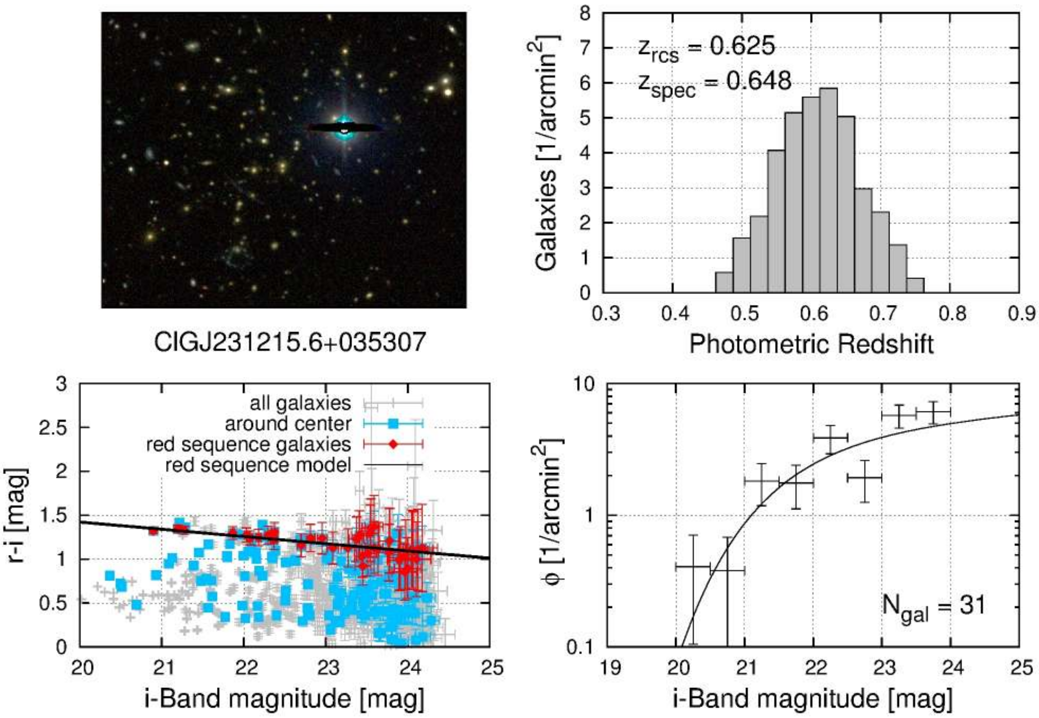

Figure 5.3.: This figure shows the output of the red sequence analysis for one cluster, ClG-$J231215.6+035307$. The top left panel shows a colour image of the inner parts of the cluster. In the top right panel we show the number of galaxies around the cluster centre, which coincide with the red sequence models as a function of redshift. Here the peak lies at $z = 0.625$. The bottom left panel shows a colour-magnitude diagram. Grey points are all galaxies in the field, blue points are galaxies within $1\overset{\prime}{.}25$ of the centre and red points are red sequence galaxies. The black line shows the red sequence for $z = 0.625$. Finally, the bottom right panel shows the i-band number counts of the cluster members, shown in the figure to the left. The black line is the best Schechter function fit. The fact that the number counts do not start to decrease at fainter magnitudes suggests that we do not suffer from significant incompleteness issues.

correlating RASS and SDSS. In this respect, the left panel of Fig. 5.4 is a confirmation that our approach works indeed. The richness distribution shows a peak between 20 and 30 and then a decreasing trend towards higher richness. The most interesting objects are those at the high richness tail at $N_{\mathrm{gal}} > 30$. Nevertheless, all objects in this sample seem to be rare X-ray luminous high-redshift galaxy clusters, which makes them interesting objects for further research.

By inspecting the colour images, eleven clusters with one or more potential strong gravitational lensing features were found. Those clusters and the arc coordinates are listed in Table 5.2 and corresponding colour images can be found in Fig. 5.5.

Due to the two clusters RCS2-J232727.7−020437 and ClG-J120958.9+495352 being in both the WHT as well as the LBT sample, we have the possibility to cross-check the results. The red sequence redshifts both agree within 2σ with the spectroscopic redshift. Comparing richness, we see that for ClG-J120958.9+495352, the measured values from the WHT sample are, within the error bars, consistent with the ones from the LBT sample (ClG-J120958.9+495352: 18 ± 5; 22 ± 5). For RCS2-J232727.7−020437, the Schechter function fit did not work for the LBT data and thus the estimate for $N_{\mathrm{gal}} = 11 \pm 6$ is very different to the one from the WHT (46 ± 7). This is due to the values to which we fix the parameters in the Schechter function. Those apparently do not match the observed data for RCS2-J232727.7−020437 in the deeper LBT data.

Six of the clusters in this sample had been discovered independently by Wen, Han & Liu (2012), another four by the *Planck* collaboration (Planck Collaboration et al., 2015b). We marked those clusters in Table 5.3.

5.5. SZ Data Analysis

The SZ signal is quantified in terms of the Compton y parameter, the line-of-sight integrated pressure. For scaling with mass, a convenient measure is the integrated Comptonization

$$Y = \int y \,\mathrm{d}\,\Omega = \frac{1}{(d_{\mathrm{A}})^2} \frac{\sigma_T}{m_e c^2} \int \mathrm{d}l \int P(r) \mathrm{d}A \,, \tag{5.5}$$

where Ω is the subtended solid angle of the cluster on the sky, d_{A} is the angular diameter distance, σ_T is the Thomson cross-section, $P(r)$ is the projected pressure profile, and A is a projected physical area. Following Marrone et al. (2012), we quantify the SZ signal in terms of the *spherical* measure

$$Y_{\mathrm{SZ}} \equiv Y_{\mathrm{sph}}(d_{\mathrm{A}})^2 = \frac{\sigma_T}{m_e c^2} \int P(r) \mathrm{d}V \,, \tag{5.6}$$

where $\mathrm{d}V$ is a physical volume element and $P(r)$ is now the pressure as a function of physical radius. Note that we have moved d_{A} to the left-hand side of the equation to remove the redshift dependence in the SZ measure.

For the pressure as a function of radial distance, we adopt the generalised NFW pressure profile (Nagai, Kravtsov & Vikhlinin, 2007), with the functional form

$$P(r) = \frac{P_0}{c_{500} x^{\gamma} (1 + c_{500} x^{\alpha})^{(\beta - \gamma)/\alpha}} \,, \tag{5.7}$$

Table 5.2.: This table names clusters where potential strong lensing features were found and gives their coordinates.

Object	Ra	Dec
ClG-*J*013710.4−103423	01:37:09.87	−10:34:31.15
ClG-*J*080434.9+330509	08:04:37.90	+33:04:53.49
ClG-*J*083415.3+452418	08:34:16.82	+45:23:24.15
ClG-*J*104803.7+313843	10:48:04.68	+31:38:51.70
	10:48:03.71	+31:38.29.46
	10:48:04.47	+31:39:05.18
ClG-*J*124515.2+245335	12:45:15.25	+24:53:46.61
ClG-*J*142040.3+395509	14:20:37.48	+39:54:48.53
	14:20:38.61	+39:54:52.47
ClG-*J*142138.3+382118	14:21:39.41	+38:21:05.21
ClG-*J*214826.3−053312	21:48:25.77	−05:33.02.26
ClG-*J*231215.6+035307	23:12:16.79	+03:52:38.90
	23:12:16.99	+03:52:12.15
ClG-*J*231520.6+090711	23:15:21.73	+09:07:34.09
	23:15:19.88	+09:07:06.59
RCS2-*J*232727.7−020437	23:27:29.41	−02:03:48.03
	23:27:30.69	−02:04:29.47

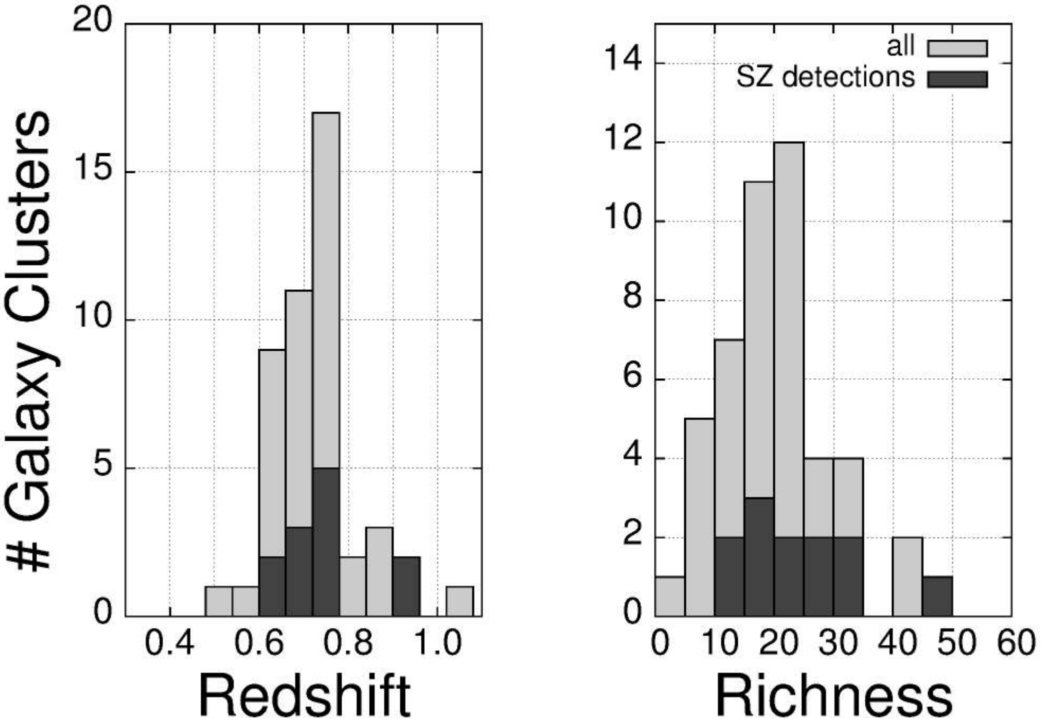

Figure 5.4.: Redshift and richness distribution of all 44 galaxy clusters in our sample and of the three previously known objects. Wherever available, we use spectroscopic redshifts. Light grey bars show the whole sample, dark grey bars the SZ-detected clusters only.

where $x = r/r_{500}$ and $(P_0, c_{500}, \alpha, \beta, \gamma)$ are parameters of the model. For our analysis, we fix (α, β, γ) to the best-fit values of the 'universal pressure profile' found by Arnaud et al. (2010).

We reduce the CARMA data using a pipeline similar to the one used in Muchovej et al. (2007), which was adapted for the use with CARMA. We first filter out bad weather errors as well as pointing errors and then apply a gain and flux calibration. For the flux calibration, we use the model of Mars from Rudy et al. (1987). We assume that Mars is a disk of uniform brightness, Fourier transform this disk to the visibility plane and compare it to the measured visibilities. From this comparison, we derive an antenna-specific scale factor, which brings the observations in line with the model. A conservative estimate for the absolute flux calibration uncertainty is $\sim$7 per cent. This results from $\sim$5 per cent uncertainty in the model from Rudy et al. (1987) and $\sim$5 per cent uncertainty from the gain solution of the telescopes.

We carry out a model fit using the pressure profile of Arnaud et al. (2010) to the interferometric data by Fourier transforming the model and comparing it to the data in visibility space. We minimize a χ^2 statistic and estimate the detection significance. If this significance is greater than three, we estimate the spherical volume-integrated Comptonization, Y_{SZ}. If the significance is less than three, we only give upper limits on Y_{SZ} and the mass. We call these cases non-detections. We estimate r_{500} by forcing Y_{SZ} to be consistent with the $Y_{\mathrm{SZ}}-M_{500}$ scaling relation of Andersson et al. (2011), which effectively means we are fitting only to integrated Comptonization (or equivalently, mass) from which r_{500} is directly given. We use the scaling relation with a fixed slope of 1.79. The positions and peak fluxes of point sources detected in the long-baseline image are included in the fit (rather than subtracted in the visibility-plane), and marginalised over in determining Y_{SZ}.

In addition to the statistical errors in the fit, there are further sources of uncertainty. First, there is intrinsic scatter in the $M-Y_{\mathrm{SZ}}$ scaling relation, for which we assume a 21 per cent intrinsic scatter in mass consistent with Andersson et al. (2011). We add this scatter in quadrature to the statistical errors of the fit as it assumes that the clusters follow the scaling relation exactly. In addition, it is important to realise that this scaling relation has been calibrated via the $M-Y_{\mathrm{X}}$ scaling relation, which itself was calibrated empirically using weak lensing data at much lower redshifts only (Vikhlinin et al., 2009). Given the high-redshift range of our clusters, any deviation from the assumed self-similar redshift evolution would lead to a systematic bias in the derived masses. So far, Jee et al. (2011) present the only weak lensing study for a large cluster sample at high redshifts. Their analysis suggests a possible evolution in the $M-T_{\mathrm{X}}$ scaling relation until $z \sim 1$ in comparison to self-similar evolution at the $20-30\%$ level. To be conservative, and accounting for the in comparison to Jee et al. (2011) slightly lower redshift range of our clusters ($z_{\mathrm{median}} = 0.725$), we therefore adopt an additional 20 per cent systematic uncertainty in the mass scale. Andersson et al. (2011) use a cosmology slightly different to ours, introducing another systematic bias of about 5 per cent in mass, which is however negligible compared to the statistical errors.

For ClG-J122208.6+422924, which was observed in a different configuration, we used the 6 m and 10 m antennas to search for point sources and the 3.5 m antennas to estimate Y_{SZ}. We analysed about 4 hours of these data but could not detect the cluster. Half of the data had only been observed at half the normal bandwidth.

From the 21 clusters analysed, we detect eleven. For those we estimate M_{500} according to the scaling relation. Furthermore, using the mass-concentration relation from Duffy et al. (2008), we can convert this to M_{200}. Again, for the non-detections, we only determine upper limits. In Fig. 5.6, we show how the masses from the SZ data scale with our richness estimates. Additionally, we also show masses which were already known for RCS2-J232727.7−020437, MACS074452.8+392725, and ClGJ1226+33. M_{200} for RCS2-J232727.7−020437 was determined from the value given for Y_{SZ} in Sharon et al. (2015), which had been measured from CARMA data. We estimate $M_{200} = (11.3 \pm 3.9) \times 10^{14}\, h_{70}^{-1}\, \mathrm{M}_{\odot}$ using the cosmology adopted in our work; the given uncertainty is dominated by the uncertainties in the scaling relation. For MACS074452.8+392725, we use the weak lensing mass estimate from Umetsu et al. (2014). Also, Jee & Tyson (2009) estimate a weak lensing mass for ClGJ1226+33. The mass estimates for MACS074452.8+392725 and ClGJ1226+33 use different techniques than we do, which means that they do not necessarily measure the same mass as our SZ estimate.

In the plot, there is only a rough relation between mass and richness visible; one can see large scatter among the data. This is expected due to comparably short integration times, the

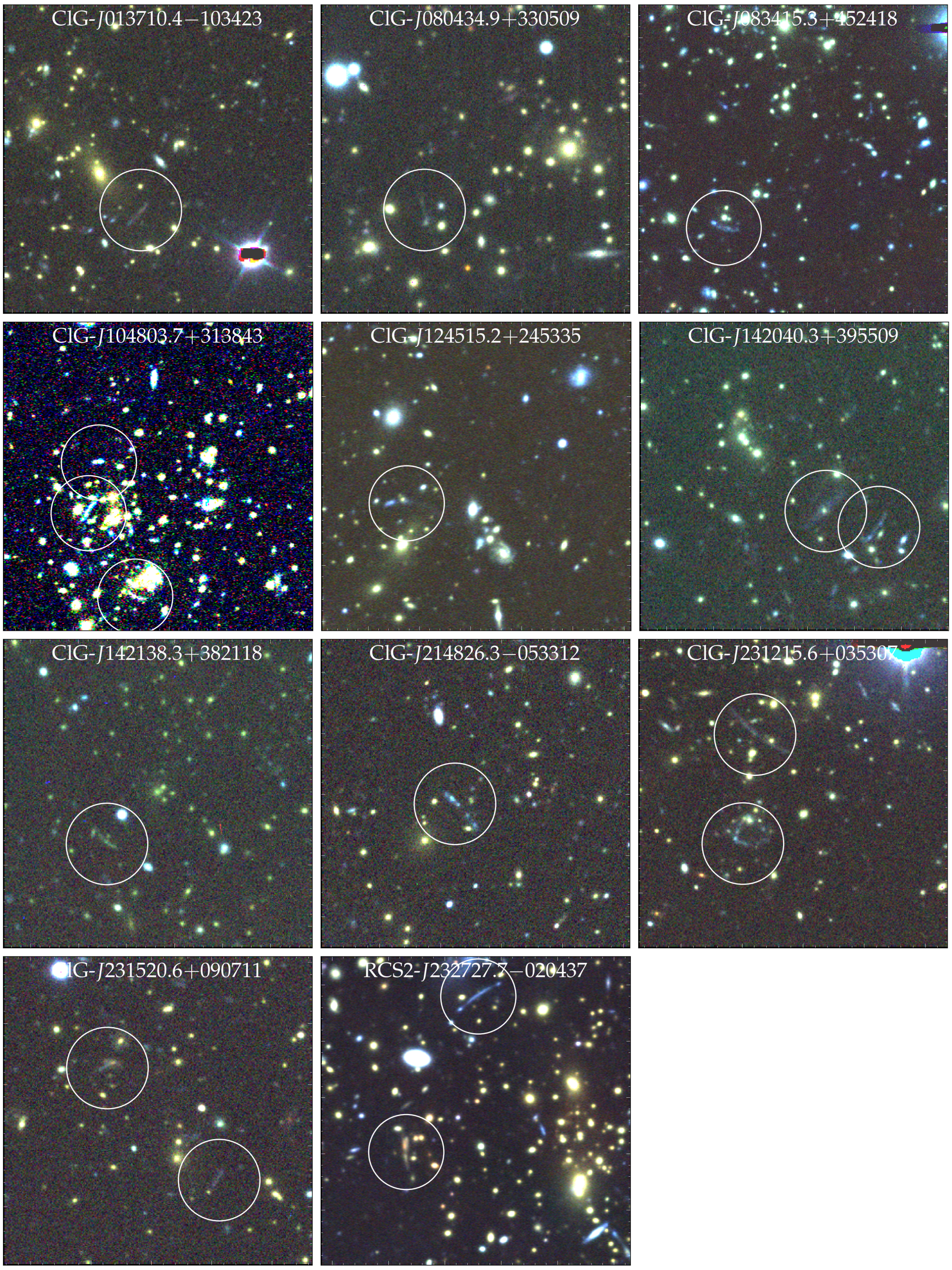

Figure 5.5.: Strong lensing arc candidates. All panels show 75″ × 75″. Arc candidates are highlighted by a white circle.

assumptions we make while determining the masses, but most importantly due to the large intrinsic scatter between mass and richness (e.g. Angulo et al. 2012). We also find that our M_{500} estimates range mostly between $3-9\times10^{14}h_{70}^{-1}\mathrm{M}_{\odot}$ at redshifts of $0.6\leq z\leq0.9$. That we only find these high masses is due to a selection effect; the less massive clusters could not be detected at $>3\sigma$ in the SZ data while using only these comparably short integration times.

The objects that have not been detected with CARMA are in most cases not particularly rich in the optical or were only integrated for a short amount of time. There are two exceptions. One of these is ClG-J142040.3+395509, for which we find a point source at the BCG position, which can potentially cancel the SZ-signal. Due to a flagged antenna, we do not have enough long baselines to properly measure the flux of this source. This could explain the apparent strong SZ-peak, with an offset of about $2'$ from the BCG position. The other one is ClG-J095416.5+173808, which is optically rich, but not detected. As we already explained before, there is a large scatter in the mass-richness relation, so this could mean that ClG-J095416.5+173808 shows a strong richness while not being massive, which would result in a faint SZ signal.

In Fig. 5.7, we show the $M_{500}-L_{\mathrm{X}}$, the $L_{\mathrm{X}}-Y_{\mathrm{SZ}}$, and the $Y_{\mathrm{SZ}}-N_{\mathrm{gal}}$ scaling relations. The blue lines show the corresponding $M_{500}-L_{\mathrm{X}}$ and $L_{\mathrm{X}}-Y_{\mathrm{SZ}}$ relations from Arnaud et al. (2010). In order to compare the data to those relations, we assume self-similar evolution, which depends on the self-similar evolution factor $E(z)=H(z)/H_0=\sqrt{\Omega_{\mathrm{m}}(1+z)^3+\Omega_{\Lambda}}$ (in this form it is only true for flat cosmologies). We plot both the CARMA detections as well as the non-detections (denoted in red) using their 3σ upper limits. The measured $M_{500}-L_{\mathrm{X}}$ and the $L_{\mathrm{X}}-Y_{\mathrm{SZ}}$ relations agree well with the results from Arnaud et al. (2010). The non-detections seem to have a preferentially lower L_{X} than the detection. When comparing N_{gal} to Y_{SZ} we find no clear trend, as already discussed for Fig. 5.6. We do not attempt to compare the mass-richness or Y_{SZ}-richness relations to previous works, due to differences in the definition of richness between studies.

All results from the CARMA SZ observations can be found in Table 5.4. In addition to the CARMA data, we also check if the clusters observed with CARMA can be found in data from *Planck*. A detailed description of this and postage stamps of the CARMA and *Planck* SZ-maps are given in the appendix.

5.6. Are there galaxy clusters too massive compared to predictions from ΛCDM?

Using M_{200} estimated from the SZ data, we can check for eleven clusters if they are too massive for our current structure formation paradigm. For this we use the fitting formula given in Mortonson, Hu & Huterer (2011) for upper mass limits as a function of redshift and survey size in a flat ΛCDM cosmology. One limitation here is that we do not test the whole sample but every cluster individually. We do not know the exact area which has been used for our cluster detection, due to our selection procedure. Nevertheless, we can calculate a lower limit for the area. For this we use all galaxies from the SDSS DR8, which includes the complete SDSS imaging data, with `psfMag_i` <13 and all objects from the RASS faint source catalogue. We grid both samples and compute the overlapping area as the sum of cells, which contain at least

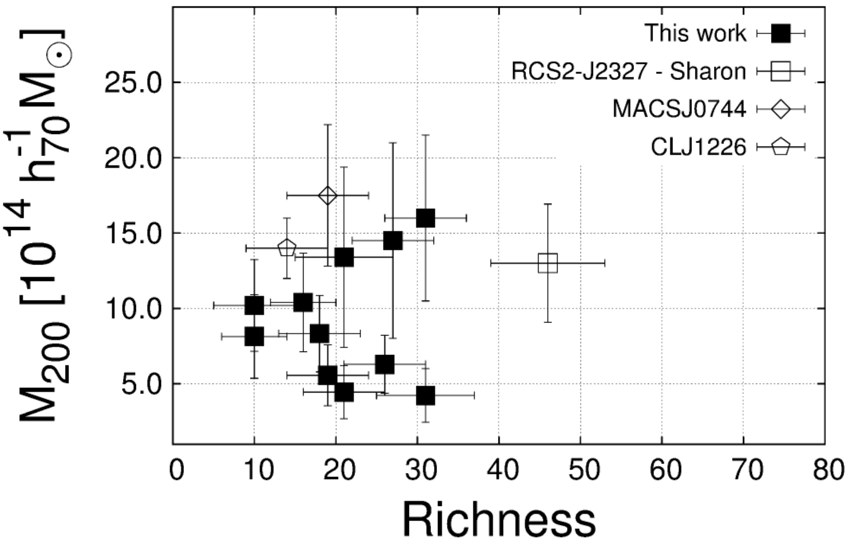

Figure 5.6.: We show mass estimates as a function of richness. The solid points are SZ masses from this study. The open symbols are masses from previous studies. The masses for RCS2-J232727.7$-$020437 were determined from $Y_{\rm SZ}$ given in Sharon et al. (2015), which was measured from CARMA data. For MACS074452.8+392725, the mass estimate is taken from Umetsu et al. (2014), which is a weak lensing mass estimate. Jee & Tyson (2009) measure a weak lensing mass for ClGJ1226+33. The error bars in mass for objects from this work include the 21 per cent scatter from the scaling relation from Andersson et al. (2011) but not the 20 per cent systematic error due to the high-redshift mass calibration (see Section 5.5).

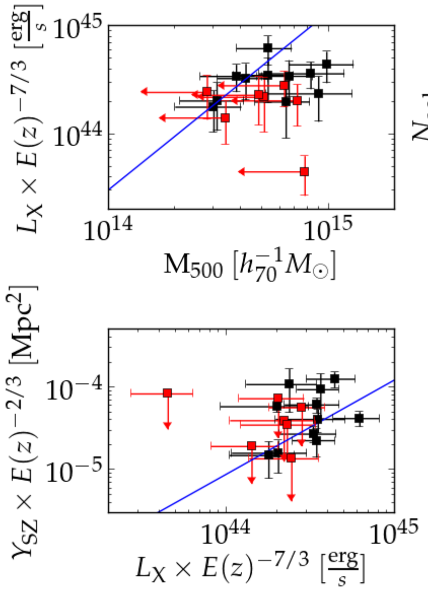

Figure 5.7.: We present scaling relations comparing the ROSAT X-ray luminosity L_{X}, the integrated Comptonization parameter Y_{SZ} from the CARMA data, the SZ-inferred galaxy cluster mass M_{500}, and the cluster richness N_{gal}. The black points show the CARMA detections, the red points the CARMA non-detections and the corresponding 3σ upper limits. The blue lines show corresponding relations from Arnaud et al. (2010). We assume self-similar evolution in order to compare the data to the scaling relations from Arnaud et al. (2010). For a detailed discussion please see Section 5.5.

one object of each survey. This estimate does strongly depend on the cell size and does not converge. In order to find a lower limit on the area used, we vary the cell size and check how many of the 44 clusters are within the overlapping area. The smallest cell size for which we still find all clusters within the overlap is $0.7 \times 0.7\,\mathrm{deg}^2$. For this configuration, we find the area to be $\approx 10,000\,\mathrm{deg}^2$. This estimate is, as mentioned before, only a lower limit and it does not take variations in sensitivity in the SDSS and RASS into account. Thus we only provide this area estimate to put our findings into a cosmological context. We also test if our sample selection is sensitive to the exposure time in RASS. We find the lowest exposure time of a cluster in the sample to be $\approx 350\,\mathrm{s}$. Areas in RASS with exposure times greater than or equal to these 350 s correspond to about 80 per cent of the total RASS area.

We plot the cluster masses against redshift in Fig. 5.8. Additionally, the masses of three clusters from previous studies are plotted (see Section 5.5). Furthermore, we take the 10 most massive clusters at redshifts $0.6 < z < 1.0$ from Bleem et al. (2015)[4] and also from *Planck*

---

[4] `http://pole.uchicago.edu/public/data/sptsz-clusters/index.html`

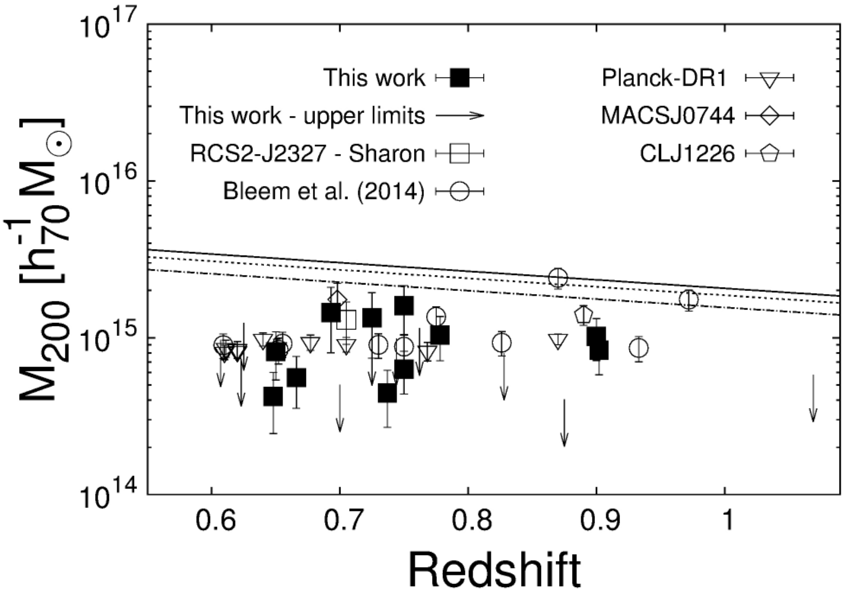

Figure 5.8.: The solid line shows the 99 per cent confidence mass limit as a function of redshift for a flat ΛCDM universe and the survey size of *Planck*. The dotted line shows the same limit for a survey size of $10,000\,\mathrm{deg}^2$, which corresponds to the survey size in this work. The dashed-dotted one shows the corresponding limit for the SPT $2500\,\mathrm{deg}^2$ survey. To compute these lines, we use the fitting formula from Mortonson, Hu & Huterer (2011) and acknowledge the fact that this gives too strict limits. The solid points show the masses estimated in this study. The other symbols represent masses from previous studies. Arrows indicate the upper limits we find in CARMA for non-detected clusters. We find no tension with the ΛCDM model. The open circles are the ten most massive clusters between $0.6 < z < 1.0$ from Bleem et al. (2015), the triangles with the tip down show the ten most massive clusters in this redshift range in the *Planck* SZ sample (Planck Collaboration et al., 2015c).

(Planck Collaboration et al., 2015c)[5], determine their M_{200} as described above and plot them as well. The masses we find for both of these samples are comparable to ours. Considering that we use the most massive ones from that study, this might again be an indication of the massive and extreme nature of our cluster sample.

As visible in Fig. 5.8, we find no significant tension between our clusters and the current cosmological standard model. The clusters from Bleem et al. (2015) and from *Planck* were found by different surveys using a different selection function. Thus, from Fig. 5.8 we should not infer possible tension for those clusters. We are aware that Hotchkiss (2011) showed that the fitting formula we use is too strict, but since none of the objects is in strong tension, the method from Mortonson, Hu & Huterer (2011) is sufficient for our purposes.

Only a sub-sample is tested here and ideally we would like to achieve mass estimates for more clusters than these eleven, preferably for those with the highest N_{gal}, since this should be a rough indication for the mass.

5.7. Notes on Individual Clusters

After this summary of the general data, we will now focus on the most notable objects in the sample, which are either high-redshift clusters, very rich clusters in the optical or very massive clusters according to their SZ signal. Those clusters are the most interesting targets for further and deeper follow-up observations, in order to determine their masses and other interesting properties.

5.7.1. RCS2-J232727.7$-$020437

We can confirm this object to be a very rich cluster. The measured photometric redshift $z_{\mathrm{phot}} = 0.725 \pm 0.042$ agrees well with the known spectroscopic one, $z_{\mathrm{spec}} = 0.705$ (Menanteau et al., 2013). The richness of 46 ± 7 (WHT) is the largest in the sample, as expected from its high mass. However, as we will see later on, there are comparable clusters in our sample. Its mass has been estimated before. For example Gralla et al. (2011) find $M_{500} = (6.2 \pm 0.8) \times 10^{14}\, h_{70}^{-1}\, \mathrm{M}_{\odot}$. Hasselfield et al. (2013) estimate masses from ACT data and use different ways to fix their $Y - M$ scaling relation. This leads to different mass estimates for RCS2-J232727.7$-$020437. The results from using what they call a 'universal pressure profile' (UPP) scaling relation is $M_{500} = (9.4 \pm 1.5) \times 10^{14}\, h_{70}^{-1}\mathrm{M}_{\odot}$, which is their lowest estimate. Their largest value arises from using a scaling relation determined with dynamical masses. With $M_{500} = (14.9 \pm 3.0) \times 10^{14}\, h_{70}^{-1}\mathrm{M}_{\odot}$, this is about 50 per cent larger than the UPP value. From the Y_{SZ} given in Sharon et al. (2015), we estimate $M_{500} = (8.1 \pm 2.3) \times 10^{14}\, h_{70}^{-1}\, \mathrm{M}_{\odot}$. This agrees well with the value from Gralla et al. (2011) and within 1σ with the UPP mass from Hasselfield et al. (2013).

---

[5] `http://pla.esac.esa.int/pla/aio/planckProducts.html`

5.7.2. ClG-J095416.5+173808

ClG-J095416.5+173808 has a measured photometric redshift of $z_{\rm phot} = 0.725 \pm 0.047$, which scatters 2σ low compared to $z_{\rm spec} = 0.828$ (Nastasi et al., 2014). The richness of $N_{\rm gal} = 40 \pm 6$ is comparable to the one of RCS2-J232727.7$-$020437. We do not detect this object with more than 3σ in CARMA.

5.7.3. ClG-J104803.7+313843

This object is located at $z_{\rm phot} = 0.750 \pm 0.047$ and has a richness of 31 ± 5. Its redshift appears to be slightly higher than the one measured for RCS2-J232727.7$-$020437. The existence of at least two potential arcs indicates a high mass, which is confirmed from the SZ observations, where we estimate $M_{200} = (16.0 \pm 5.5) \times 10^{14}\, h_{70}^{-1}{\rm M}_{\odot}$. This makes it one of the most massive systems known at high redshift.

5.7.4. ClG-J120958.9+495352

We discovered ClG-J120958.9+495352, which has a spectroscopic redshift of $z_{\rm spec} = 0.902$ and a measured red sequence redshift of $z_{\rm phot} = 0.950 \pm 0.112$ (WHT). The richness within 0.5 Mpc was measured to be 18 ± 5 (WHT). Due to its large distance, we cannot probe the luminosity function down to faint magnitudes. Based on the RASS count rate, this is the most X-ray luminous cluster discovered by our program with $L_{\rm X} = (20.3 \pm 6.2) \times 10^{44} \frac{\rm erg}{\rm s}$. In addition to the findings from the optical data, we estimate its SZ-mass to be $M_{200} = (8.3 \pm 2.5) \times 10^{14}\, h_{70}^{-1}{\rm M}_{\odot}$.

5.7.5. ClG-J122208.6+422924

ClG-J122208.6+422924 is the object with the highest measured red sequence redshift in our sample ($z_{\rm phot} = 1.000 \pm 0.200$). The large error arises from the fact that only very few cluster members are visible, and those have an average i-band magnitude of $i \approx 24.1$, which is very close to the detection limit. The measured spectroscopic redshift is somewhat larger with $z_{\rm spec} = 1.069$, which was measured from the two brightest cluster members, and both spectra show a clear break at the corresponding 4000 Å position. This makes the object by far the highest redshift one in the sample. Nevertheless, the two brightest cluster galaxies are detected in the SDSS which, given their high-redshift, is very rare and might indicate a high mass for those galaxies. We do not detect this object in 4 h of CARMA data but measure a 3σ upper mass limit $M_{500} < 3.8 \times 10^{14}\, h_{70}^{-1}{\rm M}_{\odot}$.

5.7.6. ClG-J133732.5+195827

This cluster has a redshift of $z_{\rm phot} = 0.900 \pm 0.106$, but it was observed at a high airmass, which might have affected the data. It does show a strong SZ signal, and considering its possibly high redshift, its mass of $M_{200} = (10.2 \pm 3.0) \times 10^{14} h_{70}^{-1}{\rm M}_{\odot}$ is extraordinarily high. The optical colour image shows only a few very red galaxies, and we measure its richness as $N_{\rm gal} = 10 \pm 5$.

5.7.7. ClG-J135345.0+432905

ClG-J135345.0+432905 shows a very strong SZ signal and with $M_{200} = (13.4 \pm 6.0) \times 10^{14} h_{70}^{-1} \mathrm{M}_{\odot}$, it is among the most massive clusters in the CARMA sample. It has no spectroscopic redshift but we measure the red sequence redshift to $z_{\mathrm{phot}} = 0.725 \pm 0.024$. Its richness is $N_{\mathrm{gal}} = 21 \pm 6$.

5.7.8. ClG-J142040.3+395509

This cluster has a spectroscopic redshift of $z_{\mathrm{spec}} = 0.607$ (Bayliss et al., 2011) and shows a richness of $N_{\mathrm{gal}} = 25 \pm 5$. From serendipitous *Chandra* observations, we conducted an X-ray analysis, which can be found in appendix 5.A. This analysis shows a gas temperature of about 8^{+3}_{-2} keV, which indicates a high mass. Also, Bayliss et al. (2011) find several strong lensing features and a high velocity dispersion of $\sigma_v = 1095^{+86}_{-175} \frac{\mathrm{km}}{\mathrm{s}}$. Oguri et al. (2012) use weak and strong gravitational lensing to measure its virial mass, which, adapted to the cosmology we use, is $M_{\mathrm{vir}} = 10.77^{+3.59}_{-2.88} \times 10^{14} \mathrm{M}_{\odot}$. Still, we did not detect this cluster at more than 3σ using CARMA. A possible explanation is a point source we find at the BCG position. This source could counter act the SZ signal and thus we would not detect the cluster. ClG-J142040.3+395509 shows a strong signal in *Planck*.

5.7.9. ClG-J142138.3+382118

With a measured redshift of $z_{\mathrm{phot}} = 0.750 \pm 0.027$ ($z_{\mathrm{spec}} = 0.762$) and a richness of 41 ± 7, this cluster appears to be at higher redshift but with a comparable richness to RCS2-J232727.7−020437. Possible strong lensing arcs have been observed which also indicate a high mass. On the other hand, we cannot detect it at more than 3σ in the CARMA data, which could be due to the short integration time of only 1.3 hours.

5.7.10. ClG-J152741.9+204443

ClG-J152741.9+204443 has a redshift of $z_{\mathrm{spec}} = 0.693$ and a richness of $N_{\mathrm{gal}} = 27 \pm 5$. This is a rather large richness, which also agrees with the CARMA analysis. There we find one of the strongest SZ signals, which corresponds to a mass of $M_{200} = (14.5 \pm 6.5) \times 10^{14} h_{70}^{-1} \mathrm{M}_{\odot}$. Again, this appears to be an exceptionally massive cluster.

5.8. Conclusions

We cross-correlated RASS and SDSS in order to find rich galaxy clusters at redshifts $0.6 \lesssim z \lesssim 1.0$. Using follow-up observations, we confirmed 44 cluster candidates. The motivation was to find similar objects as RCS2-J232727.7−020437, in which we succeeded. We estimated red sequence redshifts which we compared to our spectroscopic sub-sample and determined the cluster richness by fitting and integrating a Schechter function.

In the end we found at least two clusters of comparable richness as RCS2-J232727.7−020437. Furthermore, we achieved rough mass estimates from SZ observations for a sub-sample of eleven clusters and find them to be massive systems. Using the formalism by Mortonson, Hu & Huterer (2011), we find no tension between any of these clusters and the standard cosmological model. Further investigations, which will need deeper and higher-quality observations, will reveal the masses of more of these rare objects and check whether those are compatible with the ΛCDM structure formation paradigm.

We have demonstrated that the approach of cross-correlating X-ray with optical data within an area of about 10 000 $\deg^2$ is efficient, resulting in the discovery of some of the richest galaxy clusters at high-z to date.

Our cluster sample is unique and complementary to the *Planck* cluster sample and also to the southern hemisphere samples of the SPT and ACT. With respect to the redshift range and the large area, this sample is more similar to the *Planck* sample than to the other two. Although we have constructed our sample by surveying a large area, we cannot attempt to infer cosmological parameters from it. The sample is by default incomplete, because we searched for the most massive objects, which are easiest to detect.

While preparing this paper, we made use of the python version of Ned Wright's cosmology calculator (Wright, 2006), which was implemented by James Schombert. Additionally, we used `TOPCAT` (Taylor, 2005) and `STILTS` (Taylor, 2006).

The overall program, and the optical follow-up campaign were conceived and led by Tim Schrabback. Glenn Morris led the Chandra analysis. The CARMA observations, reductions, and analysis were conducted by Christopher Greer, Martin Sommer, and Dan Marrone. Jens Erler created the y-maps from the Planck data.

Bibliography

Ahn C. P. et al., 2014, ApJS, 211, 17

Aihara H. et al., 2011, ApJS, 193, 29

Andersson K. et al., 2011, ApJ, 738, 48

Angulo R. E., Springel V., White S. D. M., Jenkins A., Baugh C. M., Frenk C. S., 2012, MNRAS, 426, 2046

Arnaud M., Pratt G. W., Piffaretti R., Böhringer H., Croston J. H., Pointecouteau E., 2010, A&A, 517, A92

Bayliss M. B., Hennawi J. F., Gladders M. D., Koester B. P., Sharon K., Dahle H., Oguri M., 2011, ApJS, 193, 8

Benn C., Dee K., Agócs T., 2008, in Society of Photo-Optical Instrumentation Engineers (SPIE) Conference Series, Vol. 7014, Society of Photo-Optical Instrumentation Engineers (SPIE) Conference Series

Bennett C. L. et al., 2003, ApJS, 148, 97

Bertelli G., Bressan A., Chiosi C., Fagotto F., Nasi E., 1994, A&AS, 106, 275

Bertin E., Arnouts S., 1996, A&AS, 117, 393

Bleem L. E. et al., 2015, ApJS, 216, 27

Bonamente M., Joy M., LaRoque S. J., Carlstrom J. E., Nagai D., Marrone D. P., 2008, ApJ, 675, 106

Brodwin M. et al., 2015, ApJ, 806, 26

Bruzual G., Charlot S., 2003, MNRAS, 344, 1000

Buddendiek A. et al., 2015, MNRAS, 450, 4248

Castander F. J., 1998, Ap&SS, 263, 91

Chabrier G., 2003, PASP, 115, 763

da Silva A. C., Kay S. T., Liddle A. R., Thomas P. A., 2004, MNRAS, 348, 1401

Duffy A. R., Schaye J., Kay S. T., Dalla Vecchia C., 2008, MNRAS, 390, L64

Ebeling H., Barrett E., Donovan D., Ma C.-J., Edge A. C., van Speybroeck L., 2007, ApJ, 661, L33

Ebeling H. et al., 2013, MNRAS, 432, 62

Ebeling H., Jones L. R., Fairley B. W., Perlman E., Scharf C., Horner D., 2001, ApJ, 548, L23

Erben T. et al., 2009, A&A, 493, 1197

Erben T. et al., 2013, MNRAS, 433, 2545

Erben T. et al., 2005, Astronomische Nachrichten, 326, 432

Fitzpatrick M. J., 1993, in Astronomical Society of the Pacific Conference Series, Vol. 52, Astronomical Data Analysis Software and Systems II, Hanisch R. J., Brissenden R. J. V., Barnes J., eds., p. 472

Giallongo E. et al., 2008, A&A, 482, 349

Gralla M. B. et al., 2011, ApJ, 737, 74

Hasselfield M. et al., 2013, JCAP, 7, 8

High F. W. et al., 2010, ApJ, 723, 1736

Hildebrandt H. et al., 2010, A&A, 523, A31

Hildebrandt H. et al., 2012, MNRAS, 421, 2355

Hotchkiss S., 2011, JCAP, 7, 4

Jee M. J. et al., 2011, ApJ, 737, 59

Jee M. J., Tyson J. A., 2009, ApJ, 691, 1337

Kaiser N. et al., 2002, in Society of Photo-Optical Instrumentation Engineers (SPIE) Conference Series, Vol. 4836, Survey and Other Telescope Technologies and Discoveries, Tyson J. A., Wolff S., eds., p. 154

Marrone D. P. et al., 2012, ApJ, 754, 119

Menanteau F. et al., 2013, ApJ, 765, 67

Mortonson M. J., Hu W., Huterer D., 2011, Phys. Rev. D, 83, 023015

Motl P. M., Hallman E. J., Burns J. O., Norman M. L., 2005, ApJ, 623, L63

Muchovej S. et al., 2007, ApJ, 663, 708

Nagai D., Kravtsov A. V., Vikhlinin A., 2007, ApJ, 668, 1

Nastasi A. et al., 2014, A&A, 564, A17

Oguri M., Bayliss M. B., Dahle H., Sharon K., Gladders M. D., Natarajan P., Hennawi J. F., Koester B. P., 2012, MNRAS, 420, 3213

Paolillo M., Andreon S., Longo G., Puddu E., Gal R. R., Scaramella R., Djorgovski S. G., de Carvalho R., 2001, A&A, 367, 59

Planck Collaboration et al., 2015a, ArXiv e-prints: 1502.01582

Planck Collaboration et al., 2013, A&A, 550, A129

Planck Collaboration et al., 2011, A&A, 536, A11

Planck Collaboration et al., 2015b, ArXiv e-prints: 1502.01598

Planck Collaboration et al., 2015c, ArXiv e-prints: 1502.01597

Remazeilles M., Delabrouille J., Cardoso J.-F., 2011, MNRAS, 410, 2481

Rudy D. J., Muhleman D. O., Berge G. L., Jakosky B. M., Christensen P. R., 1987, Icarus, 71, 159

Schechter P., 1976, ApJ, 203, 297

Schirmer M., 2013, ApJS, 209, 21

Sharon K. et al., 2015, ArXiv e-prints: 1503.07188

Stanek R., Rasia E., Evrard A. E., Pearce F., Gazzola L., 2010, ApJ, 715, 1508

Taylor M. B., 2005, in Astronomical Society of the Pacific Conference Series, Vol. 347, Astronomical Data Analysis Software and Systems XIV, Shopbell P., Britton M., Ebert R., eds., p. 29

Taylor M. B., 2006, in Astronomical Society of the Pacific Conference Series, Vol. 351, Astronomical Data Analysis Software and Systems XV, Gabriel C., Arviset C., Ponz D., Enrique S., eds., p. 666

Tody D., 1993, in Astronomical Society of the Pacific Conference Series, Vol. 52, Astronomical Data Analysis Software and Systems II, Hanisch R. J., Brissenden R. J. V., Barnes J., eds., p. 173

Umetsu K. et al., 2014, ApJ, 795, 163

Vikhlinin A. et al., 2009, ApJ, 692, 1060

Voges W. et al., 1999, A&A, 349, 389

Voges W. et al., 2000, IAU Circ., 7432, 3

Wen Z. L., Han J. L., Liu F. S., 2012, ApJS, 199, 34

Wright E. L., 2006, PASP, 118, 1711

Wright E. L. et al., 2010, AJ, 140, 1868

5.A. X-ray Analysis of ClG-J142040.3+395509

In addition to our optical and SZ data, we found serendipitous archival data from *Chandra* for ClG-J142040.3+395509. Fig. 5.9 shows the $0.6 - 7.0\,\mathrm{keV}$ count rate image. This was background subtracted and exposure corrected. When fitting a simple free absorption + thermal Bremsstrahlung model to the data, we find the metallicity to be $0.5^{+0.4}_{-0.3}\,Z_\odot$ and a temperature of $T_X = 8^{+3}_{-2}$ keV. This temperature as well as the high velocity dispersion from Bayliss et al. (2011) indicate a high mass. The flux in the 0.6-7.0 keV band is $S_X = 6.8 \times 10^{-13}\,\frac{\mathrm{erg}}{\mathrm{cm}^2\,\mathrm{s}}$. The 2-10 keV luminosity is $L_X = 8.1 \times 10^{44}\,\frac{\mathrm{erg}}{\mathrm{s}}$ which is consistent with the RASS luminosity in Table 5.3. In Fig. 5.9, we also show the optical three-colour image superposed with the X-ray contours. Clearly the X-ray peak coincides with the position of the BCG.

The chip being analysed here is acis-S4, which is non standard for the analysis of extended sources. This means that the calibration model is probably not as reliable as usual which might result in an additional systematic bias of our measurements. All errors given are 1σ errors.

5.B. Galaxy Cluster and SZ Data

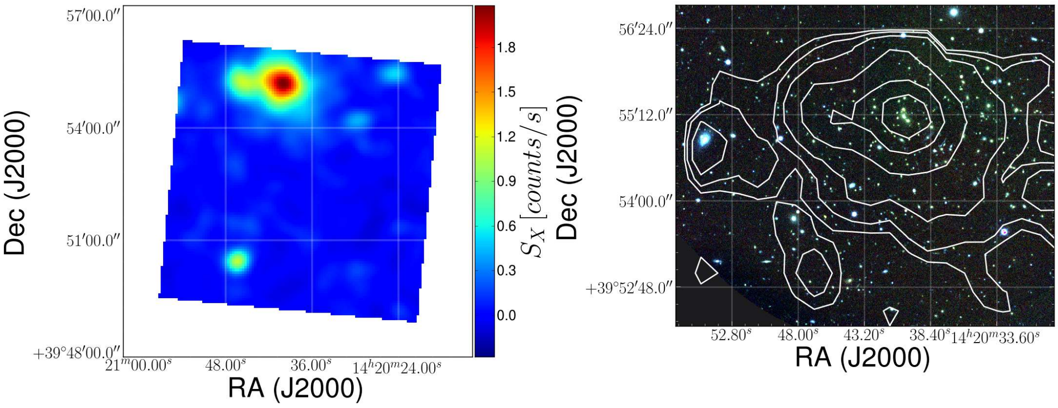

Figure 5.9.: *left:* Smoothed *Chandra* image of ClG-J142040.3+395509. Colour indicates the count rate. The cluster is visible in the upper part of the image. *right:* White lines are X-ray contours from *Chandra* superposed on the optical three-colour image from the WHT. This image shows a much smaller part of the field than visible in the left panel, due to the small field of view in the optical. The contour levels are 0.05, 0.1, 0.2, 0.5, 1.0 and 1.5 counts/s.

Table 5.3.: This table shows photometric and spectroscopic redshifts, richness, X-ray counts in 1/s, and the X-ray luminosity in $10^{44}\,\mathrm{erg\,s^{-1}}$ measured in the ROSAT $0.1-2.4$ keV band. N_{gal} is the richness measured using the Schechter function fit, N_{count} the one measured by counting galaxies brighter than $m^* + 2$. In the comments column we have noted several anomalies, namely: ^{1} bimodal red sequence galaxy distribution as a function of redshift or only a weak signal (compare Fig. 5.3 top right panel); ^{2} the data is shallow compared to other images; ^{3} the object had been observed at high airmass (≈ 2); ^{4} the Schechter function fit did not work well, which means that our fixed parameters lead to poor fits. For clusters with known spectroscopic redshift we used those instead of the photometric ones for the richness estimate. Coordinates given are those of the BCG. Cluster names showing the superscript † were independently discovered by Wen, Han & Liu (2012); the superscript $^\diamond$ indicates clusters that have been independently discovered by the *Planck* collaboration (Planck Collaboration et al., 2015b).

Object	WHT	LBT	SZ	Ra	Dec	z_{phot}	z_{spec}	N_{gal}	N_{count}	$\mathrm{counts}_{\mathrm{X}}$	L_X	com.
ClG-J001640.6−130644†	x	-	-	00:16:40.636	−13:06:43.84	0.700±0.097	-	18±6	13±4	0.0297±0.0126	6.5±3.1	1
ClG-J005805.6+003058	x	-	-	00:58:05.648	+00:30:57.85	0.725±0.017	-	33±6	39±6	0.0230±0.0099	5.5±2.4	
ClG-J013710.4−103423	x	-	-	01:37:10.433	−10:34:23.15	0.525±0.034	0.662	24±5	17±4	0.0192±0.0091	2.9±1.4	4
ClG-J031924.2+404055	x	-	-	03:19:24.237	+40:40:54.91	0.750±0.020	0.680	6±3	13±4	0.0229±0.0087	5.0±1.9	1,4
MACSJ074452.8+392725	x	-	-	07:44:52.775	+39:27:25.45	0.675±0.028	0.698	19±5	17±4	0.0148±0.0073	3.1±1.5	
ClG-J080434.9+330509$^{\dagger\diamond}$	x	-	-	08:04:34.899	+33:05:08.99	0.575±0.014	0.552	24±5	26±5	0.0239±0.0102	3.0±1.3	
ClG-J083415.3+452418†	-	x	x	08:34:15.317	+45:24:18.19	0.675±0.029	0.666	19±5	13±4	0.0416±0.0116	8.1±2.3	
ClG-J084009.8+442154	x	-	-	08:40:09.783	+44:21:53.51	0.700±0.060	-	21±4	26±5	0.0689±0.0209	15.0±5.0	2
ClG-J093503.2+061438	x	-	x	09:35:03.235	+06:14:38.46	0.750±0.031	-	9±3	8±3	0.0435±0.0135	11.2±3.6	
ClG-J094742.3+351742	-	x	-	09:47:42.313	+35:17:41.81	0.500±0.065	-	20±4	2±1	0.0190±0.0086	1.8±0.9	4
ClG-J094700.0+631905	x	-	-	09:47:00.010	+63:19:04.99	0.700±0.062	0.710	9±4	10±3	0.0172±0.0076	3.8±1.8	4
ClG-J094811.6+290709	x	-	x	09:48:11.569	+29:07:09.48	0.775±0.063	0.778	16±4	21±5	0.0337±0.0109	9.5±3.4	
ClG-J095416.5+173808	-	x	-	09:54:16.461	+17:38:07.76	0.725±0.047	0.828	40±6	15±4	0.0216±0.0110	6.5±3.4	
ClG-J102714.5+034500	x	-	-	10:27:14.475	+03:45:00.36	0.700±0.030	0.749	20±5	33±6	0.0304±0.0126	7.4±3.1	
ClG-J103605.6+441140	x	-	-	10:36:05.645	+44:11:40.29	0.800±0.119	-	5±3	13±4	0.0228±0.0100	6.9±3.6	4
ClG-J104803.7+313843	-	x	x	10:48:03.669	+31:38:42.90	0.750±0.047	-	31±5	10±3	0.0443±0.0132	12.1±3.9	
ClG-J120958.9+495352	x	x	x	12:09:58.948	+49:53:52.02	0.950±0.112	0.902	18±5	16±4	0.0486±0.0145	20.3±6.2	
ClG-J122208.6+422924	x	-	x	12:22:08.612	+42:29:24.19	1.000±0.200	1.069	7±4	12±3	0.0189±0.0087	11.3±7.2	4
ClJ1226+33	x	-	-	12:26:58.170	+33:32:48.41	0.950±0.028	0.892	14±5	27±5	0.0233±0.0102	9.5±4.2	
ClG-J124515.2+245335†	-	x	x	12:45:15.204	+24:53:35.41	0.650±0.027	-	10±4	15±1	0.0233±0.0100	4.2±1.8	
ClG-J131104.8+551443	x	-	-	13:11:04.815	+55:14:42.67	0.775±0.127	-	12±5	10±3	0.0204±0.0080	5.7±2.8	
ClG-J131339.7+221151	x	-	-	13:13:39.723	+22:11:50.82	0.675±0.019	0.737	21±5	25±5	0.0232±0.0106	5.3±2.5	
ClG-J133620.3+544540	-	x	x	13:36:20.308	+54:45:40.22	0.875±0.039	-	17±4	20±4	0.0204±0.0088	7.7±3.4	
ClG-J133732.5+195827	x	-	x	13:37:32.451	+19:58:26.57	0.900±0.106	-	10±5	11±3	0.0162±0.0079	6.5±3.5	3
ClG-J135345.0+432905$^\diamond$	x	-	x	13:53:44.996	+43:29:05.12	0.725±0.024	-	21±6	42±6	0.0393±0.0107	9.3±2.6	

Table 5.3.:

Object	WHT	LBT	SZ	Ra	Dec	$z_{\rm phot}$	$z_{\rm spec}$	$N_{\rm gal}$	$N_{\rm count}$	counts$_{\rm X}$	L_X	com.
ClG-J142008.8−031906	x	-	-	14:20:08.763	−03:19:06.40	0.750±0.070	-	16±4	20±4	0.0209±0.0112	5.4±3.0	
ClG-J142040.3+395509$^{\dagger\diamond}$	x	-	x	14:20:40.353	+39:55:09.72	0.600±0.044	0.607	25±5	34±6	0.0360±0.0100	5.5±1.6	
ClG-J142138.3+382118$^{\diamond}$	x	-	x	14:21:38.288	+38:21:18.32	0.750±0.027	0.762	41±7	42±6	0.0209±0.0084	5.5±2.3	2
ClG-J142227.4+233739	x	-	-	14:22:27.366	+23:37:38.82	0.750±0.017	0.726	23±5	20±4	0.0284±0.0105	6.9±2.6	
ClG-J143411.9+175039	x	-	x	14:34:11.929	+17:50:38.96	0.800±0.020	0.744	25±7	35±6	0.0278±0.0101	7.4±2.7	3
ClG-J144847.4+284312	x	-	-	14:48:47.381	+28:43:12.17	0.750±0.125	-	3±2	3±2	0.0186±0.0074	4.8±2.4	1,2,3
ClG-J145508.4+320028	x	-	-	14:55:08.384	+32:00:27.90	0.675±0.017	0.654	11±4	27±5	0.0161±0.0068	3.0±1.3	
ClG-J150532.2+331249†	x	-	-	15:05:32.212	+33:12:48.83	0.725±0.036	0.757	24±5	24±5	0.0142±0.0058	3.6±1.5	
ClG-J151544.3+042554	x	-	-	15:15:44.312	+04:25:53.65	0.700±0.039	-	32±8	29±5	0.0262±0.0100	5.7±2.2	
ClG-J151601.9+394426	x	-	x	15:16:01.946	+39:44:26.57	0.725±0.025	-	10±5	34±6	0.0288±0.0084	6.8±2.0	2,3,4
ClG-J152741.9+204443	x	-	x	15:27:41.933	+20:44:42.77	0.700±0.034	0.693	27±5	14±4	0.0269±0.0122	5.8±2.6	
ClG-J153035.0+130512	x	-	-	15:30:34.980	+13:05:12.31	0.625±0.025	-	17±4	34±6	0.0216±0.0103	3.6±1.7	3,4
ClG-J153258.8+021324	x	-	-	15:32:58.807	+02:13:23.87	0.850±0.119	-	13±3	12±3	0.0209±0.0086	7.3±3.6	1,3
ClG-J153735.6+382851	x	-	x	15:37:35.582	+38:28:50.90	0.750±0.057	-	26±5	29±5	0.0336±0.0116	8.7±3.2	
ClG-J171225.8+561253	x	-	-	17:12:25.840	+56:12:52.51	0.600±0.036	-	19±5	13±4	0.0082±0.0036	1.2±0.6	
ClG-J174109.9+555819	x	-	x	17:41:09.881	+55:58:19.06	0.625±0.036	-	18±5	27±5	0.0059±0.0023	1.0±0.4	
ClG-J214826.3−053312	x	-	-	21:48:26.270	−05:33:12.01	0.625±0.025	-	23±5	34±6	0.0211±0.0095	3.5±1.6	
ClG-J223007.6−080949	x	-	x	22:30:07.589	−08:09:48.80	0.575±0.017	0.623	24±5	25±5	0.0336±0.0154	5.1±2.4	
ClG-J223727.5+135523	x	-	x	22:37:27.543	+13:55:22.56	0.700±0.043	-	15±5	24±5	0.0161±0.0067	3.5±1.5	
ClG-J231215.6+035307	x	-	x	23:12:15.600	+03:53:06.90	0.625±0.030	0.648	31±6	19±4	0.0234±0.0093	4.1±1.7	
ClG-J231520.6+090711	x	-	-	23:15:20.558	+09:07:11.09	0.725±0.024	-	20±5	36±6	0.0206±0.0086	4.9±2.1	
RCS2-J232727.7−020437	x	x	-	23:27:27.7	−02:04:37.00	0.725±0.042	0.705	46±7	35±6	0.0474±0.0137	10.7±3.6	4(LBT)

5.C. Postage Stamps of all Clusters

5.D. Maps from the CARMA Data

5.E. Results from Planck Data

We constructed 10° × 10° y-maps of all 44 galaxy clusters from public *Planck* data by forming a linear combination of maps (the ILC method; Bennett et al. 2003; Remazeilles, Delabrouille & Cardoso 2011), using all six frequency bands of the *Planck* High Frequency Instrument (HFI), taken from the recent 2015 data release (Planck Collaboration et al., 2015a).

A Gaussian filter was applied to smooth all maps to a common resolution of $10'$, corresponding to the *Planck* beam at 100 GHz. The final Compton-y maps are the weighted sum of all six maps: $y = \sum_i \omega_i T_i / T_{\mathrm{CMB}}$. Here T_i are the individual channel maps, each weighted with an ILC-coefficient ω_i. The coefficients are chosen to minimise the variance of the reconstructed Compton-y map while fulfilling two constrains: 1) eliminate the primary CMB Temperature anisotropies and 2) preserve the temperature fluctuations introduced by the SZ effect. The produced map may contain an offset, since the variance of the map stays unaffected while adding a constant. The map offset was determined by fitting the histogram of pixel values with a Gaussian, which provides a very good model for the map noise. The offset is then corrected for by subtracting the mean of the Gaussian. In Fig. 5.13, we show *Planck* y-maps for all clusters, which have been observed with CARMA.

Table 5.4.: This table shows the results from the SZ observations. t_{int} is the integration time in hours. All masses are in $10^{14}h_{70}^{-1}\mathrm{M}_{\odot}$, Y_{SZ} is given in $10^{-5}\mathrm{Mpc}^2$. To the statistical mass errors from the fit, we have added in quadrature the 21 per cent scatter from the scaling relation from Andersson et al. (2011). We acknowledge the fact that our error bars do not include the 20 per cent systematic error from the uncertainty in the high-redshift mass calibration (see Section 5.5).

Object	z_{spec}	z_{phot}	Y_{SZ}	M_{500}	M_{200}	t_{int}
ClG-J083415.3+452418	0.666	0.675	2.9±1.1	3.8±1.2	5.6±2.0	3.5
ClG-J094811.6+290709	0.778	0.775	8.2±1.7	6.6±1.9	10.4±3.3	4.1
ClG-J095416.5+173808	0.828	0.725	< 5.4	< 5.1	< 8.0	4.0
ClG-J104803.7+313843	-	0.750	16.8±3.6	9.8±3.2	16.0±5.5	3.5
ClG-J120958.9+495352	0.902	0.950	5.9±1.2	5.3±1.5	8.3±2.5	6.8
ClG-J122208.6+422924	1.069	1.000	< 3.7	< 3.8	< 5.8	4.0
ClG-J124515.2+245335	-	0.650	5.3±1.7	5.3±1.6	8.1±2.8	4.1
ClG-J131339.7+221151	0.737	0.675	2.1±0.9	3.1±1.0	4.4±1.8	5.8
ClG-J133620.3+544540	-	0.875	< 1.9	< 2.8	< 4.0	3.6
ClG-J133732.5+195827	-	0.900	8.2±1.2	6.4±1.8	10.2±3.0	1.4
ClG-J135345.0+432905	-	0.725	12.3±6.8	8.3±3.5	13.4±6.0	1.6
ClG-J142040.3+395509	0.607	0.600	< 7.0	< 6.2	< 9.7	1.5
ClG-J142138.3+382118	0.762	0.750	< 9.7	< 7.2	< 11.5	1.3
ClG-J143411.9+175039	0.744	0.800	< 7.5	< 6.3	< 9.9	1.7
ClG-J151601.9+394426	-	0.725	< 7.5	< 6.3	< 9.9	0.9
ClG-J152741.9+204443	0.693	0.700	14.0±7.6	9.0±3.8	14.5±6.5	1.8
ClG-J153735.6+382851	-	0.750	3.6±0.8	4.2±1.1	6.3±1.9	5.1
ClG-J174109.9+555819	-	0.625	< 10.5	< 7.8	< 12.4	4.5
ClG-J223007.6−080949	0.623	0.575	< 4.4	< 4.8	< 7.3	3.4
ClG-J223727.5+135523	-	0.700	< 2.5	< 3.4	< 5.0	6.3
ClG-J231215.6+035307	0.648	0.625	1.9±0.9	3.0±1.0	4.2±1.8	6.8

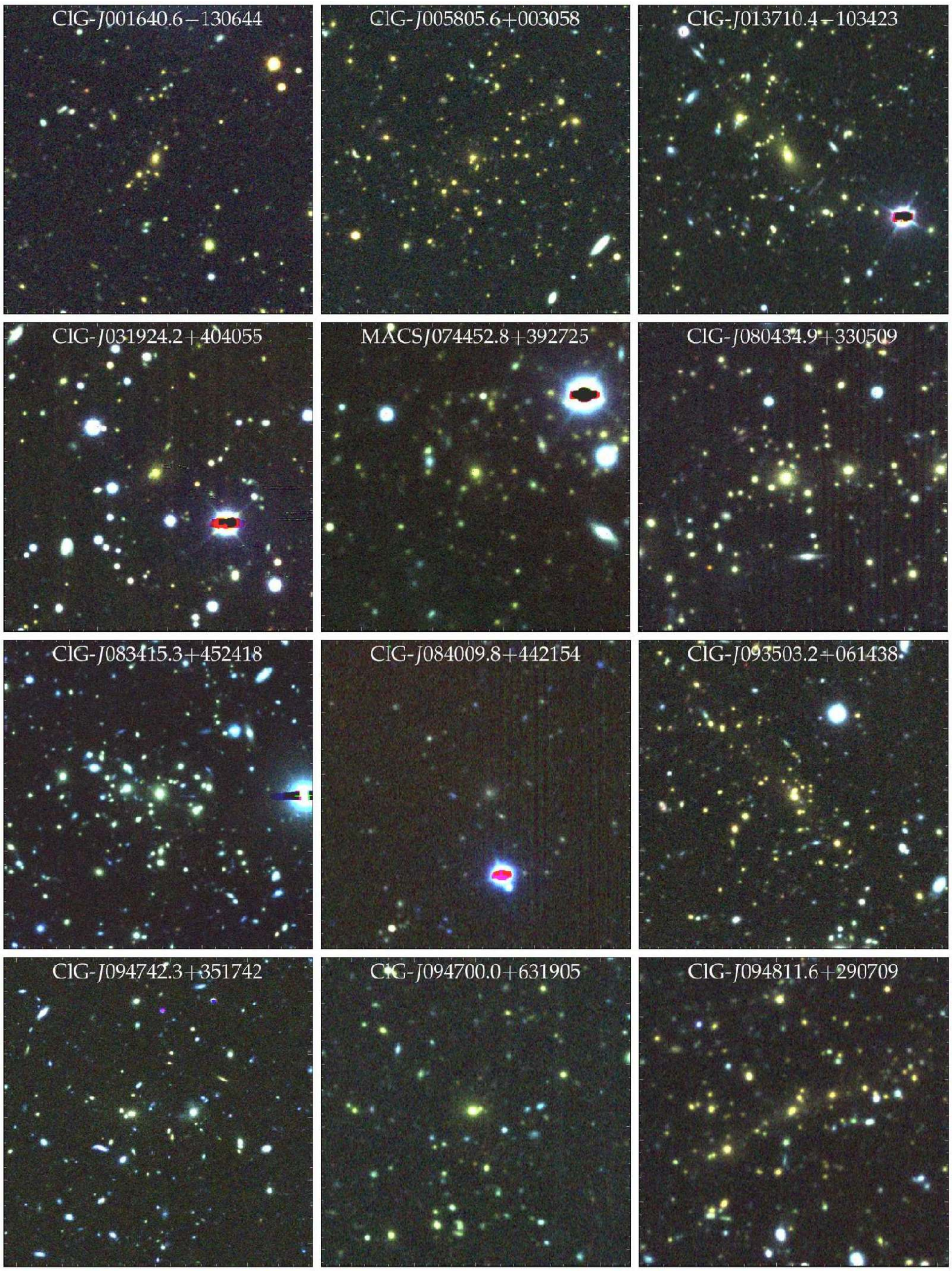

Figure 5.10.: In this figure, we present optical postage stamps of all clusters in our sample. These postage stamps were created using the r-, i- and z band images from WHT and LBT. Wherever available, we show the LBT data, which is considerably deeper. Which data is available can be found in Table 5.3. All images show the inner $1\farcm7$ of the cluster.

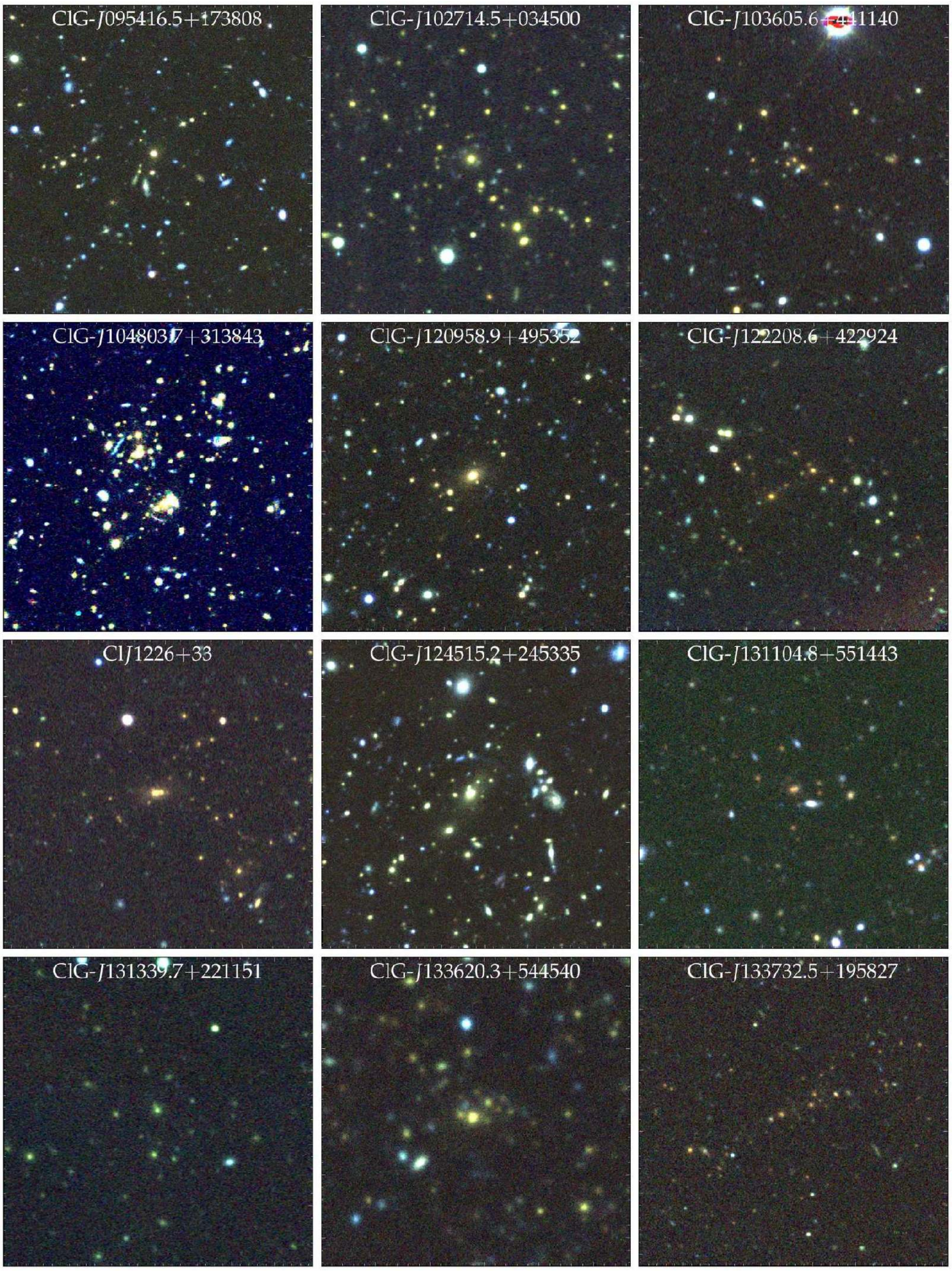
ClG-J095416.5+173808
ClG-J102714.5+034500
ClG-J103605.6+441140
ClG-J104803.7+313843
ClG-J120958.9+495352
ClG-J122208.6+422924
ClJ1226+33
ClG-J124515.2+245335
ClG-J131104.8+551443
ClG-J131339.7+221151
ClG-J133620.3+544540
ClG-J133732.5+195827

Figure 5.10.:

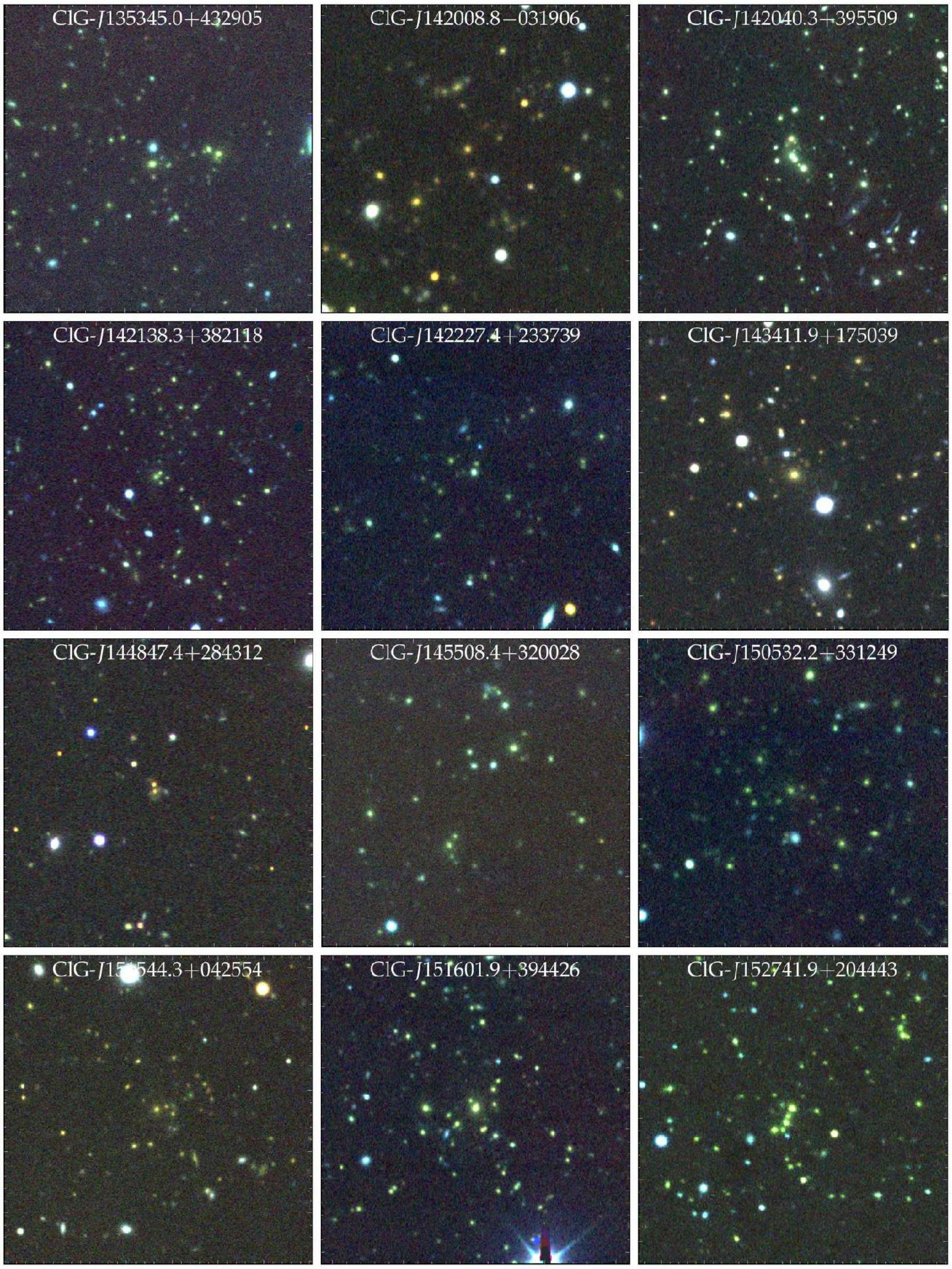
ClG-J135345.0+432905
ClG-J142008.8−031906
ClG-J142040.3+395509
ClG-J142138.3+382118
ClG-J142227.4+233739
ClG-J143411.9+175039
ClG-J144847.4+284312
ClG-J145508.4+320028
ClG-J150532.2+331249
ClG-J15 544.3+042554
ClG-J151601.9+394426
ClG-J152741.9+204443

Figure 5.10.:

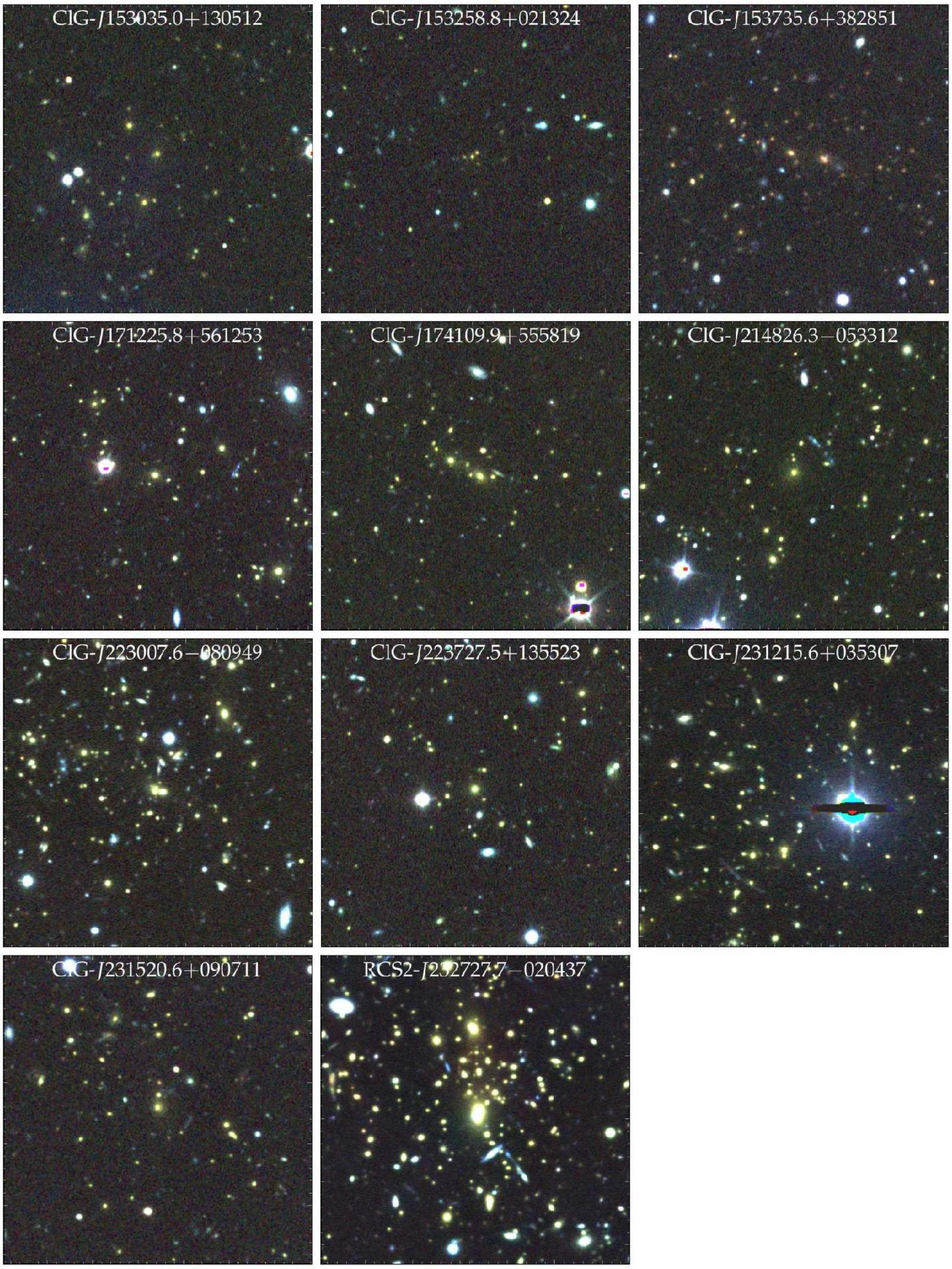
ClG-J153035.0+130512
ClG-J153258.8+021324
ClG-J153735.6+382851
ClG-J171225.8+561253
ClG-J174109.9+555819
ClG-J214826.3−053312
ClG-J223007.6−080949
ClG-J223727.5+135523
ClG-J231215.6+035307
ClG-J231520.6+090711
RCS2-J232727.7−020437

Figure 5.10.:

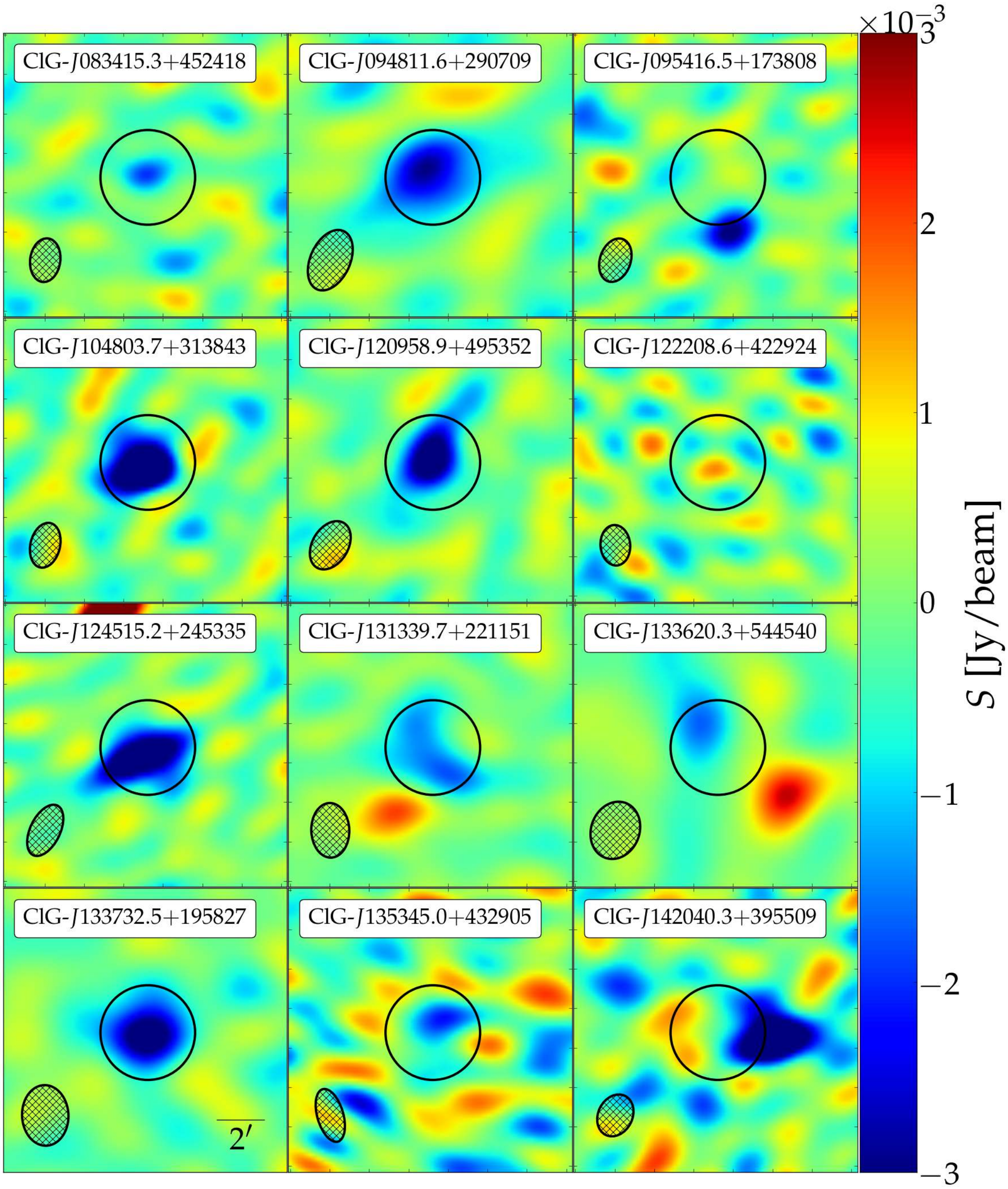

Figure 5.11.: We show SZ-maps for all clusters observed with CARMA. The images show $12 \times 12'$. The ellipses in the bottom left are the beams, the circle in the centre has a $2'$ radius and indicates the BCG position.

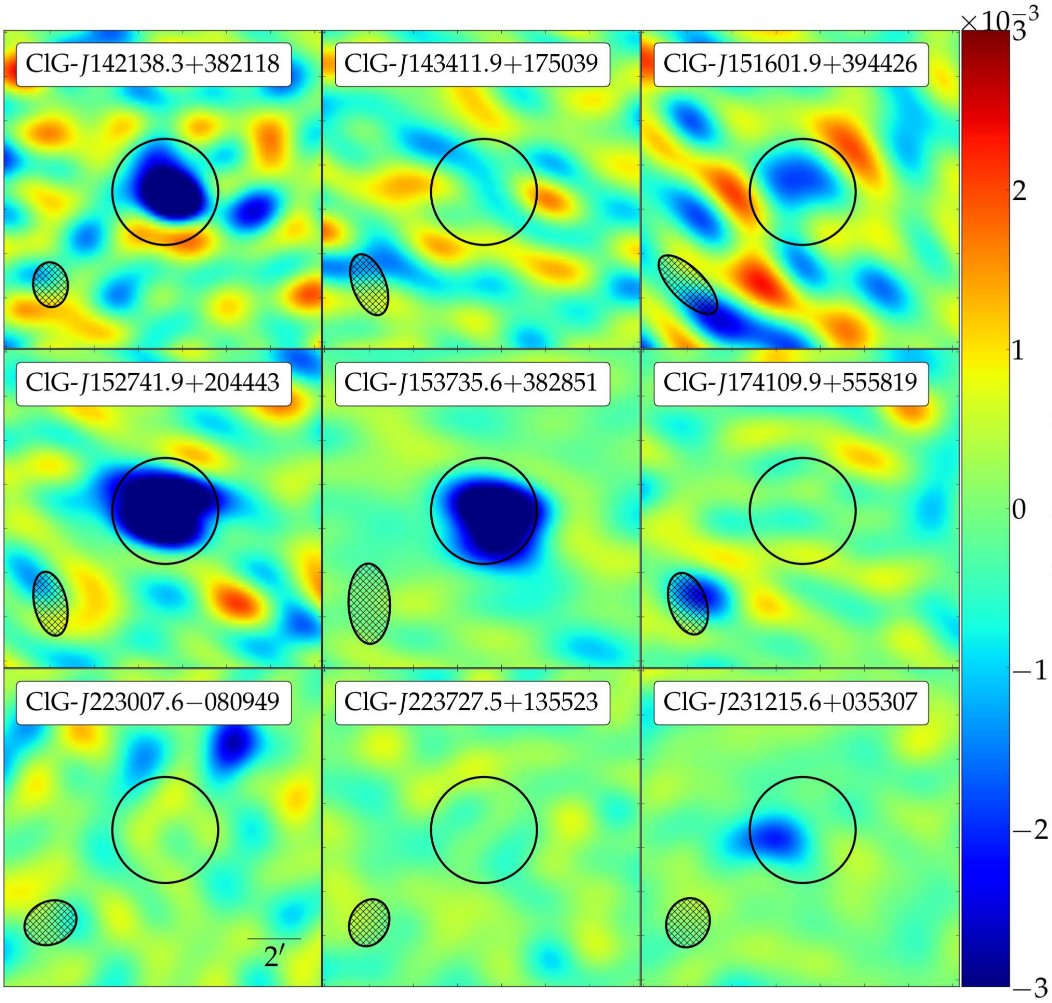
ClG-J142138.3+382118
ClG-J143411.9+175039
ClG-J151601.9+394426
ClG-J152741.9+204443
ClG-J153735.6+382851
ClG-J174109.9+555819
ClG-J223007.6−080949
ClG-J223727.5+135523
ClG-J231215.6+035307
2′
×10⁻³
3
2
1
0
−1
−2
−3
S [Jy/beam]

Figure 5.11.:

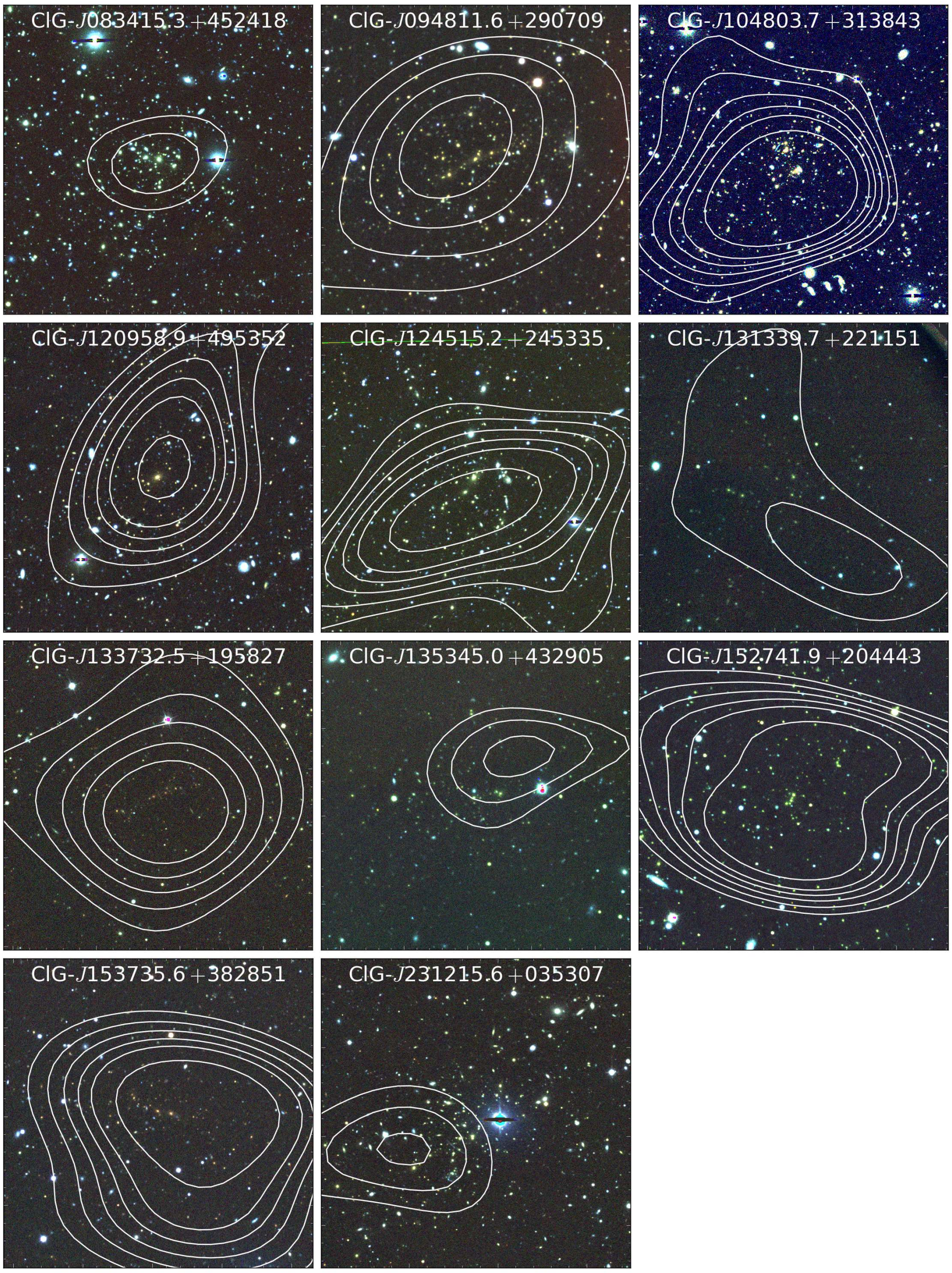

Figure 5.12.: We show optical three-colour images and the corresponding SZ-overlay for all clusters that have been detected at more than 3σ with CARMA. The images show $4.'2 \times 4.'2$ around the BCG. The contour levels are $-4.0, -3.0, -2.5, -2.0, -1.5$ and -1.0×10^{-3}Jy/beam.

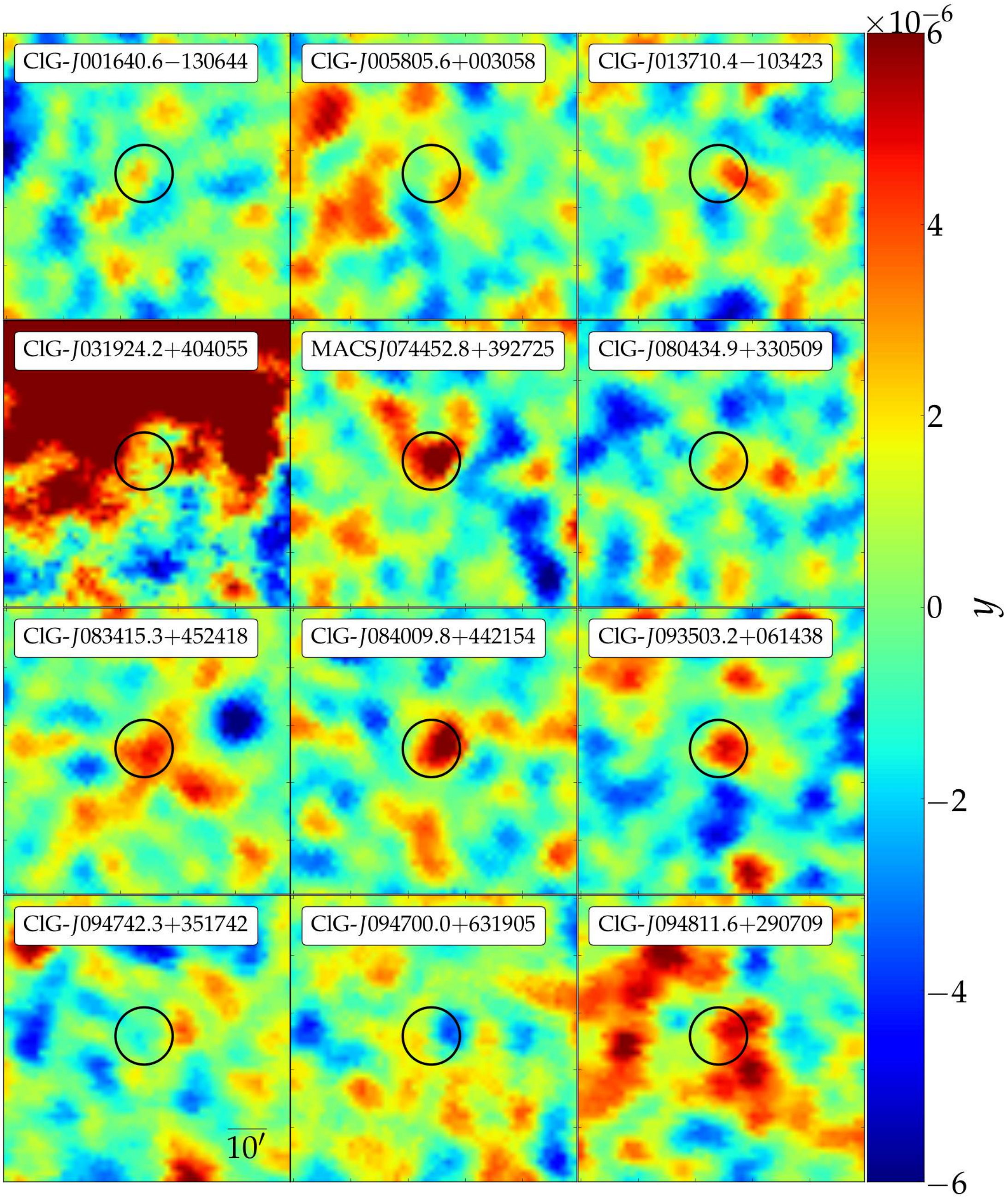

Figure 5.13.: This figure shows the y-maps of all the clusters in our sample in *Planck*. The images show a $1.25 \times 1.25\,\mathrm{deg}^2$ field around the cluster. The black circle has a $7\overset{\prime}{.}5$ radius and is centred at the BCG.

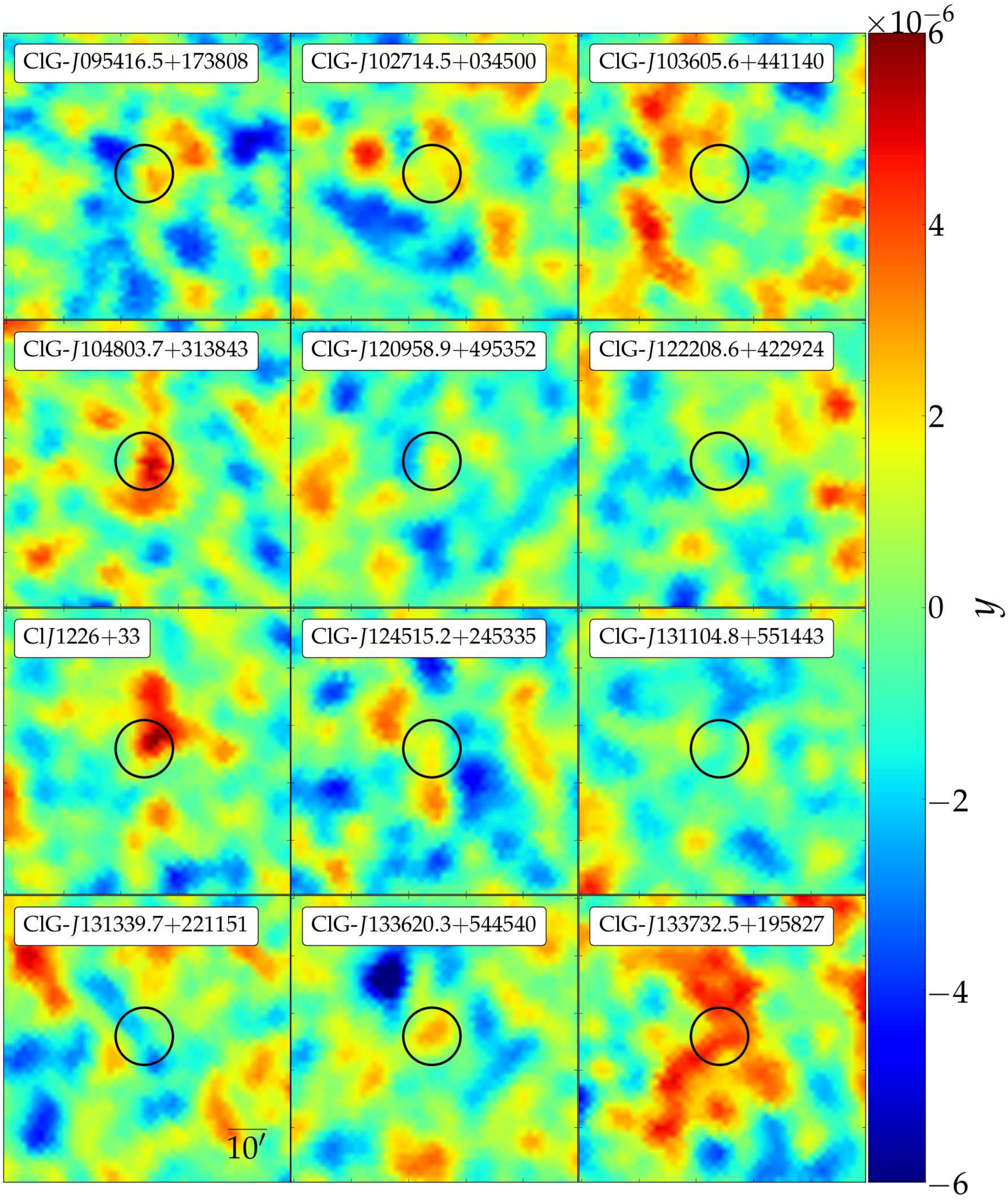
ClG-J095416.5+173808
ClG-J102714.5+034500
ClG-J103605.6+441140
ClG-J104803.7+313843
ClG-J120958.9+495352
ClG-J122208.6+422924
ClJ1226+33
ClG-J124515.2+245335
ClG-J131104.8+551443
ClG-J131339.7+221151
ClG-J133620.3+544540
ClG-J133732.5+195827
10′
×10⁻⁶
6
4
2
0
−2
−4
−6
y

Figure 5.13.:

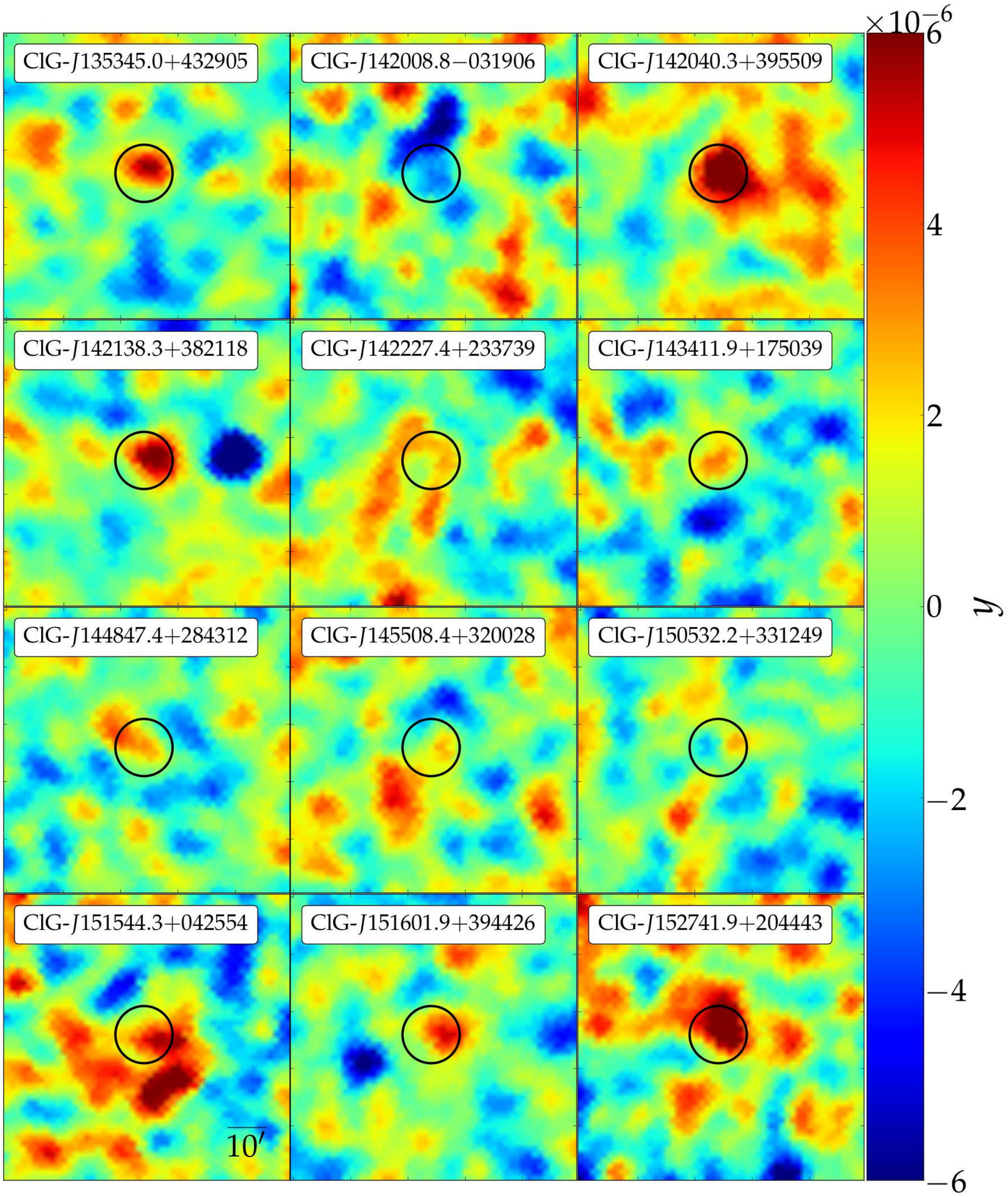
ClG-J135345.0+432905
ClG-J142008.8−031906
ClG-J142040.3+395509
ClG-J142138.3+382118
ClG-J142227.4+233739
ClG-J143411.9+175039
ClG-J144847.4+284312
ClG-J145508.4+320028
ClG-J150532.2+331249
ClG-J151544.3+042554
ClG-J151601.9+394426
ClG-J152741.9+204443
10′
×10⁻⁶
6
4
2
0
−2
−4
−6
y

Figure 5.13.:

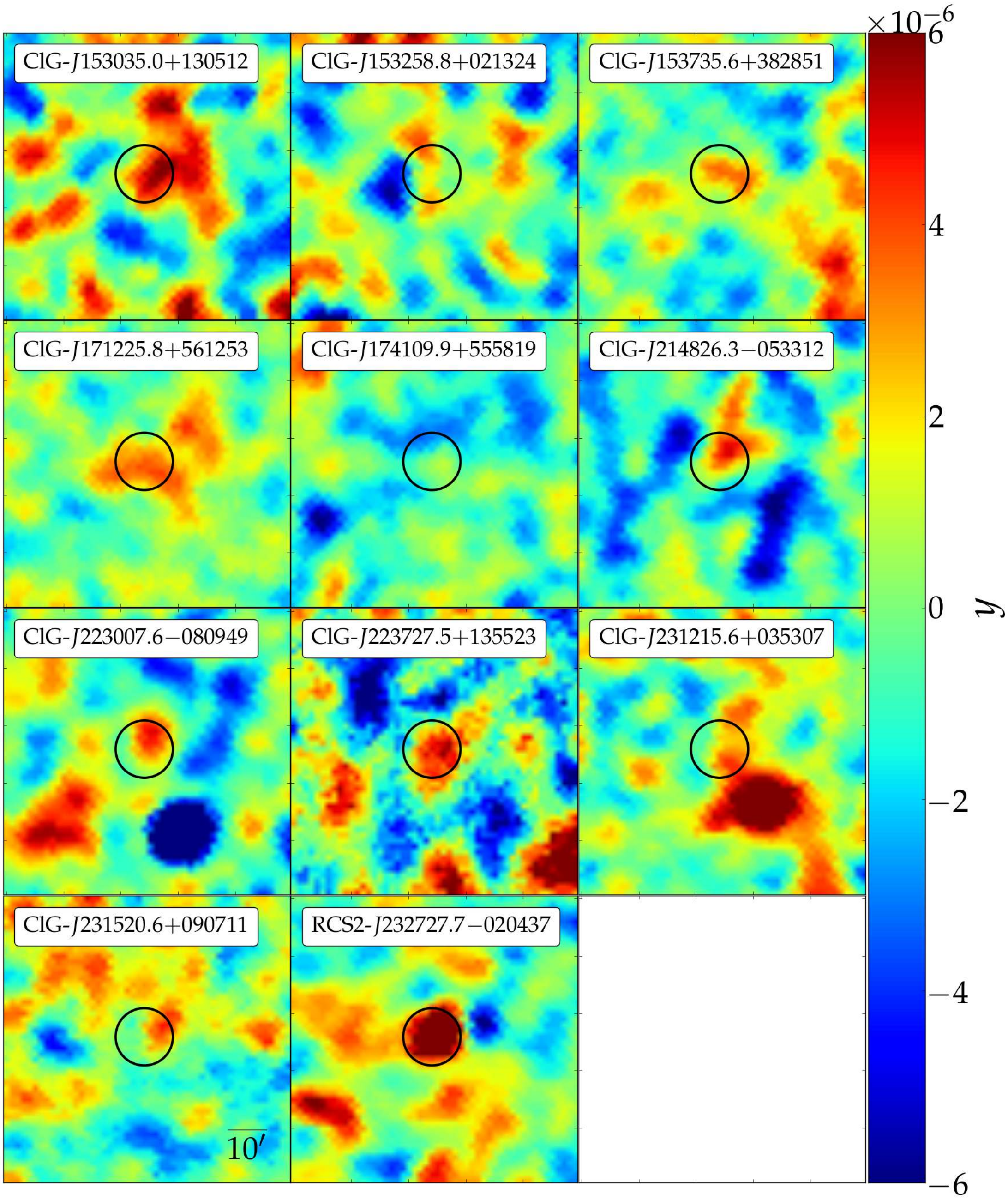
ClG-J153035.0+130512
ClG-J153258.8+021324
ClG-J153735.6+382851
ClG-J171225.8+561253
ClG-J174109.9+555819
ClG-J214826.3−053312
ClG-J223007.6−080949
ClG-J223727.5+135523
ClG-J231215.6+035307
ClG-J231520.6+090711
RCS2-J232727.7−020437
10′
×10⁻⁶
6
4
2
0
−2
−4
−6
y

Figure 5.13.:

CHAPTER 6

A new Estimator for Galaxy-Matter Correlations

This chapter is based on an analysis of data from RCSLenS and BOSS and is soon to be submitted to a journal. As RCSLenS uses a blinding scheme in order to prevent confirmation bias, the catalogues contain four different columns with galaxy ellipticities, from which only one is the true measured one (the procedure will be explained in more detail in this chapter). When I submitted this thesis, the manuscript for this paper was almost in its final form, but not quite. This is why the results still include information from all four ellipticity columns, and not only the single true one, which will only be revealed once the whole manuscript is finalised.

6.1. Introduction

Since the discovery of the accelerated expansion of the universe using supernovae in 1998 and 1999 (Riess et al. 1998; Perlmutter et al. 1999), the origin and nature of dark energy remains unknown. Several possible explanations like a cosmological constant, quintessence, or a modification of gravity on cosmological scales have been suggested. Although the accelerated expansion was confirmed by other cosmological probes like CMB experiments (Hinshaw et al. 2013; Planck Collaboration et al. 2015), weak gravitational lensing (Schrabback et al. 2010; Heymans et al. 2013), galaxy clusters (Vikhlinin et al. 2009; Mantz et al. 2014), or baryonic acoustic oscillations (BAO, Blake et al. 2012; Sánchez et al. 2013), the statistical power of these probes so far remains insufficient to reveal the true nature of dark energy. Statistical precision sufficient to distinguish a cosmological constant from a more dynamical nature of dark energy will only be reached by the next generation of cosmology experiments, like *Euclid* (Laureijs et al., 2011), the LSST (Ivezic et al., 2008), or *WFIRST* (Spergel et al., 2015). For this purpose, the *Euclid* satellite will not only map the whole extragalactic sky in the optical and the near-infrared, but it will also take near-infrared spectra of about 50 million galaxies up to a redshift of $z = 2$. Using this vast data set, the *Euclid* consortium will measure the geometry of the Universe using both baryonic acoustic oscillations and cosmic shear.

Cosmic shear is the distortion of light bundles from distant sources caused by the intervening tidal gravitational field, caused by the large-scale matter distribution in the Universe, which is measured from the auto-correlation of galaxy shapes (e.g. Bacon, Refregier & Ellis 2000; Van Waerbeke et al. 2001; Hoekstra et al. 2002b; see Bartelmann & Schneider 2001 for a review). The gravitational lensing signal in the galaxy shapes contributes only a few per cent of the whole galaxy ellipticities; furthermore, these galaxies are intrinsically small, typically smaller than the point-spread function of ground-based observations, and correspondingly are measured only on a very limited number of pixels on CCD detectors. Correcting for PSF effects and pixelisation still poses a great challenge to the astronomical community (e.g. Kitching et al. 2012; Mandelbaum et al. 2015). Due to these technical difficulties, it is important to have multiple independent weak lensing probes to map the density field in our Universe. A particularly promising approach is to combine information from galaxy auto-correlations (e.g. Blake et al. 2012; Sánchez et al. 2013) and galaxy-matter correlations (e.g. van Uitert et al. 2011; van Uitert et al. 2012; Velander et al. 2014). Much effort has been put into developing new theoretical frameworks for these measurements (e.g. Leauthaud et al. 2011; Eriksen & Gaztanaga 2014; Coupon et al. 2015).

A further challenge in relating observed signals to theoretical predictions stems from the difficulty to understand baryonic physics, like cooling, star formation, and feedback, which affects the statistical properties of the large-scale structure on small scales. Motivated by that, a particularly interesting approach was suggested by Baldauf et al. (2010), henceforth B10, who introduced a new estimator Υ for clustering and lensing, which ignores all small-scale contributions to the signals. This was successfully applied to data from the SDSS by Mandelbaum et al. (2013). This new estimator can be used to constrain cosmological parameters as well as the bias between galaxies and the dark matter distribution (Kaiser, 1984).

In this work we will show that the Υ statistic is a special case of the aperture mass formalism (Schneider 1996; Schneider et al. 1998). Using this information, we generalise the B10 approach; in particular, we define a complete set of estimators for a given range of scales which all are ‘blind’ to the correlation functions below a predescribed threshold. We expect that the first few elements of this discrete set contain all the relevant information, which thus leads to a substantial data compression and a much lower dimensional covariance, similar to the COSEBIs for cosmic shear (Schneider, Eifler & Krause, 2010).

As a proof of concept, in this paper we fix the cosmology and use the new estimators to measure the bias of a particular galaxy sample. For this study, we use as lenses the galaxies from the Baryon Oscillations Spectroscopic Survey (BOSS) LOWZ sample (Eisenstein et al., 2011) and as sources photometrically selected background galaxies from the Red Cluster Sequence Lensing Survey (RCSLenS[1]; Hildebrandt et al. in prep.). In order to create the corresponding covariance matrix, we use mock catalogues, that were initially designed for Choi et al. (in prep.) and are based on the simulations by Harnois-Deraps & van Waerbeke (2015).

---

[1] www.rcslens.org

In Sect. 6.2, we introduce the B10 method, our generalisation, and the approach to measure the galaxy bias. Section 6.3 describes the data analysis, and in Section 6.4, we give a detailed discussion. As the fiducial cosmology, we use a flat ΛCDM cosmology constrained by *Planck* with $H_0 = 67.74\,\mathrm{km\,s^{-1}Mpc^{-1}}$, $\Omega_{\mathrm{m},0} = 0.3089$, $\Omega_{\Lambda,0} = 0.6911$, and $\sigma_8 = 0.8159$ (Planck Collaboration et al., 2015). For testing the sensitivity of our results with respect to cosmological parameters, we also use the cosmology obtained in Heymans et al. (2013): $H_0 = 73.8\mathrm{km\,s^{-1}Mpc^{-1}}$, $\Omega_{\mathrm{m},0} = 0.271$, $\Omega_{\Lambda,0} = 0.729$, and $\sigma_8 = 0.799$.

6.2. Method

6.2.1. The Υ statistics interpreted as M_{ap}

In B10 two new estimators were introduced, one in terms of the projected galaxy correlation function ω_{p}, and one in terms of the differential surface mass density $\Delta\Sigma$ around galaxies, as measured from the tangential shear component γ_{t}. Those estimators are being simultaneously analysed in order to recover information about the dark matter distribution. In this chapter, we will generalise these estimators, but instead of ω_{p} and $\Delta\Sigma$ we will use the angular correlation function $\omega(\vartheta)$ and the tangential shear $\gamma_{\mathrm{t}}(\vartheta)$ around (foreground) galaxies. These quantities can be obtained from large photometric lensing surveys for which no spectroscopic redshift information is available. When using only photometric redshifts, measuring ω_{p} is not sensible. Nevertheless, for this proof of concept study, we will later make use of a spectroscopically selected galaxy sample, because current photometric surveys still are very heterogeneous in terms of photometry. This introduces systematics in the clustering measurement, which will change with future surveys.

The estimator introduced by B10 in case of the tangential shear γ_{t} is[2]

$$\hat{\Upsilon}(\vartheta, \vartheta_{\mathrm{min}}) = \gamma_{\mathrm{t}}(\vartheta) - \left(\frac{\vartheta_{\mathrm{min}}}{\vartheta}\right)^2 \gamma_{\mathrm{t}}(\vartheta_{\mathrm{min}}) \, , \tag{6.1}$$

where ϑ_{min} is the scale below which small-scale information is suppressed. There are two features in the definition of $\hat{\Upsilon}(\vartheta, \vartheta_{\mathrm{min}})$ which require attention. First, it is a continuous function of the scale ϑ; in any analysis, this angular scale needs to be discretised when comparing measurements with theoretical predictions, and it is unclear how this discretisation is optimised, as a balance between enough points to include all relevant cosmological information on the one hand, and to limit the number of points for manageable sizes of covariances on the other hand. A second feature is the occurrence of $\gamma_{\mathrm{t}}(\vartheta_{\mathrm{min}})$ for every ϑ in $\hat{\Upsilon}$, which means that any uncertainty in this quantity will affect $\hat{\Upsilon}(\vartheta, \vartheta_{\mathrm{min}})$ at all scales ϑ in a similar way. Furthermore, as the tangential shear at a fixed angular separation cannot be measured, but must be averaged over a finite interval, this can introduce systematics in the measurement of $\gamma_{\mathrm{t}}(\vartheta_{\mathrm{min}})$, and thus the $\hat{\Upsilon}(\vartheta, \vartheta_{\mathrm{min}})$. In fact, Mandelbaum et al. (2013) determined $\gamma_{\mathrm{t}}(\vartheta_{\mathrm{min}})$ by a power-law fit of the tangential shear (more precisely, of $\Delta\Sigma$) over a finite interval bracketing both sides of the minimum scale.

---

[2] As mentioned before, B10 actually define Υ in terms of $\Delta\Sigma$. To be consistent throughout the paper, we use γ_{t}. Thus we denote the B10 statistics in terms of γ_{t} as $\hat{\Upsilon}$.

Here we address both issues, by first relating the $\hat{\Upsilon}$-statistic to the aperture mass (Schneider, 1996), which is defined as

$$M_{\rm ap} = \int_{\phi_{\rm min}}^{\phi_{\rm max}} {\rm d}\phi\, \phi\, \mathcal{U}(\phi)\, \kappa(\phi)\ , \tag{6.2}$$

where $\kappa(\phi)$ is the convergence, azimuthally averaged over polar angle and over the foreground galaxy population, $\mathcal{U}$ is a compensated filter function, i.e.,

$$\int_{\phi_{\rm min}}^{\phi_{\rm max}} {\rm d}\phi\, \phi\, \mathcal{U}(\phi) = 0\ ; \tag{6.3}$$

and $\phi_{\rm min}$ and $\phi_{\rm max}$ the inner and outer scales on which the weight function is non-zero. The aperture mass can be expressed in terms of the azimuthally averaged tangential shear $\gamma_{\rm t}$, yielding

$$M_{\rm ap} = \int_{\phi_{\rm min}}^{\phi_{\rm max}} {\rm d}\phi\, \phi\, \mathcal{Q}(\phi)\, \gamma_{\rm t}(\phi)\ , \tag{6.4}$$

where $\mathcal{Q}$ is related to $\mathcal{U}$ via

$$\mathcal{Q}(\phi) = \frac{2}{\phi^2} \int_0^{\phi} {\rm d}\phi'\, \phi'\, \mathcal{U}(\phi') - \mathcal{U}(\phi)\ . \tag{6.5}$$

For every value of ϑ we can interpret $\hat{\Upsilon}$ as an aperture mass. Indeed, comparing Eq. (6.4) with Eq. (6.1), we see immediately that $\hat{\Upsilon}(\vartheta, \vartheta_{\rm min})$ is a special case of $M_{\rm ap}$ if we set $\phi_{\rm min} = \vartheta_{\rm min}$, $\phi_{\rm max} = \vartheta$, and

$$\mathcal{Q}(\phi) = +\frac{1}{\phi}\delta_{\rm D}(\phi - \vartheta) - \frac{\vartheta_{\rm min}}{\vartheta^2}\delta_{\rm D}(\phi - \vartheta_{\rm min})\ , \tag{6.6}$$

where $\delta_{\rm D}$ is the Dirac delta function. Inverting Eq. (6.5), we find

$$\mathcal{U}(\phi) = -\mathcal{Q}(\phi) + 2\int_{\phi}^{\infty} {\rm d}\phi' \frac{\mathcal{Q}(\phi')}{\phi'}\ , \tag{6.7}$$

which yields

$$\mathcal{U}(\phi) = -\frac{1}{\phi}\delta_{\rm D}(\phi - \vartheta) + \frac{\vartheta_{\rm min}}{\vartheta^2}\delta_{\rm D}(\phi - \vartheta_{\rm min}) + \frac{2}{\vartheta^2}\left[\mathcal{H}(\vartheta - \phi) - \mathcal{H}(\vartheta_{\rm min} - \phi)\right]\ , \tag{6.8}$$

where $\mathcal{H}$ is the Heaviside step function. This equation shows that the $\hat{\Upsilon}$-statistics is indeed insensitive to $\kappa(\vartheta)$ on scales $\vartheta < \vartheta_{\rm min}$, and thus allows the exclusion of small scales where theoretical predictions are believed to be uncertain.

6.2.2. Measuring Υ by using a set of orthogonal functions

The filter functions $\mathcal{U}$ and $\mathcal{Q}$ of the aperture mass depend on the scale ϑ of $\hat{\Upsilon}$. Instead of using a continuum of scales ϑ, we can define a complete set of compensated filter functions $\mathcal{U}_n$ over the range of scales $\vartheta_{\rm min} \leq \vartheta \leq \vartheta_{\rm max}$, i.e., each filter function satisfies

$$\int_{\vartheta_{\rm min}}^{\vartheta_{\rm max}} {\rm d}\vartheta\, \vartheta\, \mathcal{U}_n(\vartheta) = 0\ . \tag{6.9}$$

The completeness ensures that the corresponding set of aperture masses contains the full information contained in $\hat{\Upsilon}(\vartheta, \vartheta_{\rm min})$ for $\vartheta_{\rm min} \leq \vartheta \leq \vartheta_{\rm max}$. In fact, we expect that most of the information is included in only the first few elements of this set, whereas the remaining ones contain essentially only noise. Working with a few numbers, instead of a continuous function, will ease the analysis, in particular the generation of covariances, due to the associated data compression, while keeping the essential features of $\hat{\Upsilon}$, i.e., suppression of small-scale influence. We choose the filter functions to be orthogonal, i.e.,

$$\int_{\vartheta_{\rm min}}^{\vartheta_{\rm max}} {\rm d}\vartheta\, \mathcal{U}_n(\vartheta)\, \mathcal{U}_m(\vartheta) = 0 \quad \text{for} \quad m \neq n\ . \tag{6.10}$$

The Legendre polynomials $\mathcal{P}_n$ form a complete orthogonal set of functions on $[-1, 1]$, which we can use to find a set of suitable filter functions. For this to work we define the transformation used in Schneider, Eifler & Krause (2010)

$$x = \frac{2(\vartheta - \bar{\vartheta})}{\Delta\vartheta}\ , \tag{6.11}$$

with $\Delta\vartheta = \vartheta_{\rm max} - \vartheta_{\rm min}$, $\bar{\vartheta} = (\vartheta_{\rm min} + \vartheta_{\rm max})/2$ and ${\rm d}\vartheta = \frac{\Delta\vartheta}{2}{\rm d}x$. This maps the interval $[\vartheta_{\rm min}, \vartheta_{\rm max}]$ onto $[-1, 1]$. Setting

$$\mathcal{U}_n(\vartheta) = \frac{1}{(\Delta\vartheta)^2} u_n\left(\frac{2(\vartheta - \bar{\vartheta})}{\Delta\vartheta}\right)\ , \tag{6.12}$$

this transforms the compensation and orthogonality conditions into

$$\int_{-1}^{1} {\rm d}x \left(\frac{x\Delta\vartheta}{2} + \bar{\vartheta}\right) u_n(x) = 0 \tag{6.13}$$

and

$$\int_{-1}^{1} {\rm d}x\, u_n(x)\, u_m(x) = \delta_{nm}\ , \tag{6.14}$$

where in the latter case we fixed the normalisation of the filter functions. The Legendre polynomials can be defined via the recurrence relation

$$\mathcal{P}_{n+1}(x) = \frac{1}{n+1}\left[(2n+1)\, x\, \mathcal{P}_n(x) - n\, \mathcal{P}_{n-1}(x)\right]\ , \tag{6.15}$$

with $\mathcal{P}_0(x) = 1$ and $\mathcal{P}_1(x) = x$. We will first try to find dimensionless filters $u_n(x)$ which are proportional to the $\mathcal{P}_n(x)$; these can then be transformed into the $\mathcal{U}_n(\vartheta)$ according to Eq. (6.12).

The first function to fulfil our two conditions is a first-order polynomial of the form $u_1(x) = a_1 x + a_0$, where the two coefficients a_i are determined from the two conditions, to yield

$$u_1(x) = \frac{3Gx - 1}{\sqrt{2(1+3G^2)}} \; , \tag{6.16}$$

where we defined $G = 2\bar{\vartheta}/\Delta\vartheta$. Since

$$\int_{-1}^{1} \mathrm{d}x \, \mathcal{P}_n(x) \, x^m = 0 \tag{6.17}$$

for $m < n$ and because the Legendre polynomials are orthogonal we can choose for $n \geq 2$ the filter functions

$$u_n(x) = \sqrt{\frac{2n+1}{2}} \, \mathcal{P}_n(x) \mathcal{H}(1 - x^2) \; , \tag{6.18}$$

which has the correct normalisation, and we explicitly included the finite interval of support for the u_n. Using Eq. (6.12), we then find

$$\mathcal{U}_n(\vartheta) = \frac{1}{(\Delta\vartheta)^2} u_n(x) = \frac{1}{(\Delta\vartheta)^2} \sqrt{\frac{2n+1}{2}} \mathcal{P}_n \left(\frac{2(\vartheta - \bar{\vartheta})}{\Delta\vartheta} \right) \mathcal{H}(\vartheta - \vartheta_{\mathrm{min}}) \mathcal{H}(\vartheta_{\mathrm{max}} - \vartheta) \; , \tag{6.19}$$

for $n \geq 2$ and

$$\mathcal{U}_1(\vartheta) = \frac{1}{(\Delta\vartheta)^2} \frac{3G \left(\frac{2(\vartheta - \bar{\vartheta})}{\Delta\vartheta} \right) - 1}{\sqrt{2(1+3G^2)}} \mathcal{H}(\vartheta - \vartheta_{\mathrm{min}}) \mathcal{H}(\vartheta_{\mathrm{max}} - \vartheta) \; . \tag{6.20}$$

The $\mathcal{Q}_n(\vartheta)$ follow immediately as

$$\mathcal{Q}_n(\vartheta) = \frac{2}{\vartheta^2} \int_0^{\vartheta} \mathrm{d}\vartheta' \, \vartheta' \, \mathcal{U}_n(\vartheta') - \mathcal{U}_n(\vartheta) \; . \tag{6.21}$$

The final estimators for galaxy-galaxy lensing then become

$$\Upsilon_{\mathrm{gm}}(n) = \int_{\vartheta_{\mathrm{min}}}^{\vartheta_{\mathrm{max}}} \mathrm{d}\vartheta \, \vartheta \;\, \mathcal{Q}_n(\vartheta) \, \gamma_{\mathrm{t}}(\vartheta) \; . \tag{6.22}$$

Since we want to compare the clustering of galaxies with the galaxy-galaxy lensing signal, to learn about the biasing of galaxies and the correlation coefficient between the galaxies and the underlying matter distribution, we define integrals of the galaxy angular correlation function that have the same angular dependence as the filter functions for the convergence κ, i.e.,

$$\Upsilon_{\mathrm{gg}}(n) = \int_{\vartheta_{\mathrm{min}}}^{\vartheta_{\mathrm{max}}} \mathrm{d}\vartheta \, \vartheta \; \mathcal{U}_n(\vartheta) \, \omega(\vartheta) \; . \tag{6.23}$$

Note that the clustering signal will be measured using the lens sample from galaxy-galaxy lensing in order to probe the same density field. During our analysis we will make use of only the first three orders of the filter functions; for our dataset, those should contain all relevant information. The corresponding filter functions for $\vartheta_{\mathrm{min}} = 3\,\mathrm{arcmin}$ and $\vartheta_{\mathrm{max}} = 20\,\mathrm{arcmin}$ are displayed in Fig. 6.1 and Fig. 6.2.

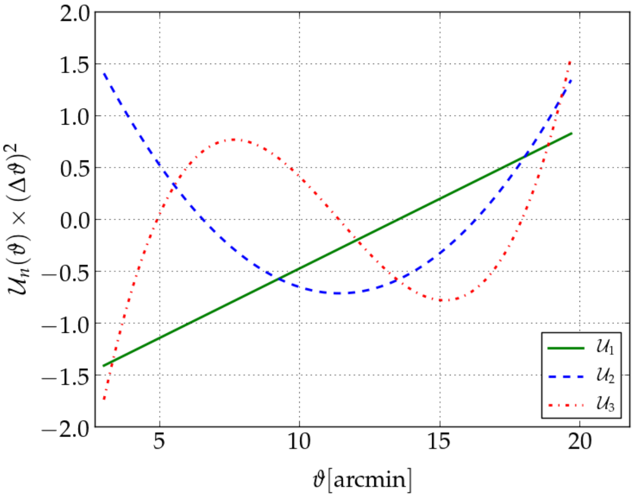

Figure 6.1.: Filter functions $\mathcal{U}_n(\vartheta)$ for clustering for $\vartheta_{\min} = 3\,\text{arcmin}$ and $\vartheta_{\max} = 20\,\text{arcmin}$.

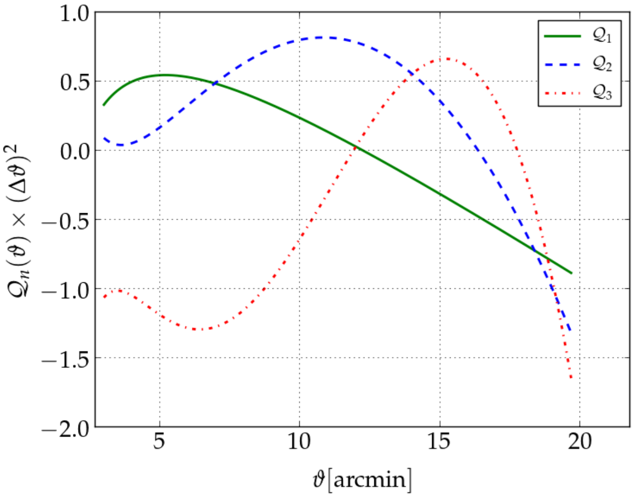

Figure 6.2.: Filter functions $\mathcal{Q}_n(\vartheta)$ for lensing for $\vartheta_{\min} = 3\,\text{arcmin}$ and $\vartheta_{\max} = 20\,\text{arcmin}$.

6.2.3. Connecting observables to theory

In order to constrain cosmological parameters or to measure the bias factor, we need to know how the observables $\Upsilon_{\rm ij}(n)$ are connected to well predictable theoretical quantities like the three dimensional dark matter power spectrum $\mathcal{P}_{3D}(k,w)$, where k is the comoving wavenumber and w the comoving distance, characterising the cosmic epoch. This is now shown for the case where the lens sample has a rather broad redshift distribution as for increasingly small distributions the following approximation diverges and is not valid any more.

The angular correlation function of galaxies is related to $\mathcal{P}_{3D}$ through (Hoekstra et al., 2002a)

$$\omega(\vartheta) = \frac{1}{2\pi}\int \mathrm{d}w \, \left(\frac{p_{\mathrm{l}w}(w)}{f_k(w)}\right)^2 \int \mathrm{d}\ell \, \ell \, \hat{b}^2(\ell,z)\mathcal{P}_{3D}\left(\frac{\ell}{f_k(w)};w\right)\mathrm{J}_0(\ell\vartheta)\;, \tag{6.24}$$

where $\hat{b}(\ell,z)$ is the galaxy bias as a function of angular wave number ℓ and redshift z, w the comoving distance, $f_k(w)$ the comoving angular diameter distance, $p_{\mathrm{l}w}(w)$ the lens probability distribution in terms of w, and J_0 the zeroth-order Bessel function of the first kind. Changing the order of integration and replacing the probability distribution with respect to w, $p_{\mathrm{l}w}(w)$, by the observable redshift distribution, using $p_{\mathrm{l}z}(z)\mathrm{d}z = p_{\mathrm{l}w}(w)\mathrm{d}w$, yields

$$\omega(\vartheta) = \frac{1}{2\pi}\int \mathrm{d}\ell \, \ell \, \mathrm{J}_0(\ell\vartheta)\int \mathrm{d}w \left(\frac{p_{\mathrm{l}z}(z)}{f_k(w)}\right)^2 \left(\frac{\mathrm{d}z}{\mathrm{d}w}\right)^2 \hat{b}^2(\ell,z)\mathcal{P}_{3D}\left(\frac{\ell}{f_k(w)};w\right)\;, \tag{6.25}$$

with

$$\frac{\mathrm{d}z}{\mathrm{d}w} = \frac{H_0\sqrt{(1+z)^2(1+z\Omega_{\mathrm{m},0})-z(2+z)\Omega_\Lambda}}{c}\;.$$

By inserting Eq. (6.25) into Eq. (6.23), we obtain an expression for $\Upsilon_{\rm gg}(n)$, which depends quadratically on the galaxy bias

$$\begin{aligned}\Upsilon_{\rm gg}(n) =& \frac{b^2}{2\pi}\int_{\vartheta_{\min}}^{\vartheta_{\max}} \mathrm{d}\vartheta \, \vartheta \, \mathcal{U}_n(\vartheta) \\ &\times \int \mathrm{d}\ell \, \ell \, \mathrm{J}_0(\ell\vartheta)\int \mathrm{d}w \left(\frac{p_{\mathrm{l}z}(z)}{f_k(w)}\right)^2 \left(\frac{\mathrm{d}z}{\mathrm{d}w}\right)^2 \mathcal{P}_{3D}\left(\frac{\ell}{f_k(w)};w\right)\;.\end{aligned} \tag{6.26}$$

Here we defined b as a weighted average of the bias $\hat{b}(\ell,z)$ over ℓ and z, where the weight is given by the factors in the integrals in Eq. (6.25). We point out that b still depends on the order n (due to the dependence of the angular weight function $\mathcal{U}_n$ on ϑ), which we do not write out explicitly[3]. The connection between $\mathcal{P}_{3D}$ and $\gamma_{\rm t}(\vartheta)$ has been shown to be (Kaiser 1992; Guzik & Seljak 2001)

$$\gamma_{\rm t}(\vartheta) = \frac{3\,\Omega_{\mathrm{m},0}}{4\pi}\left(\frac{H_0}{c}\right)^2 \int \mathrm{d}w \, \frac{g(w)p_{\mathrm{l}w}(w)}{a(w)f_k(w)}\int \mathrm{d}\ell \, \ell \, \hat{b}(\ell,z)\,\hat{r}(\ell,z)\mathcal{P}_{3D}\left(\frac{\ell}{f_k(w)};w\right)\mathrm{J}_2(\ell\vartheta)\;, \tag{6.27}$$

---

[3] When constraining b later on, we will actually constrain an average over n, ℓ, and z

where $\hat{r}$ is the cross-correlation coefficient, $a(w)$ the cosmic scale factor, and $g(w)$ is the mean of angular diameter distances (e.g., Hoekstra et al., 2002a)

$$g(w) = \int_{w}^{w_H} \mathrm{d}w' \, p_{\mathrm{s}w}(w') \frac{f_k(w'-w)}{f_k(w')} \; , \tag{6.28}$$

where $p_{\mathrm{s}w}(w)$ is the source distance probability distribution in terms of w. Again, by changing the order of integration, inserting the redshift probability distribution and inserting it into Eq. (6.22), one finds

$$\begin{aligned} \Upsilon_{\mathrm{gm}}(n) = & \frac{3\,\Omega_{\mathrm{m},0}}{4\pi} \left(\frac{H_0}{c}\right)^2 b\, r \int_{\vartheta_{\mathrm{min}}}^{\vartheta_{\mathrm{max}}} \mathrm{d}\vartheta \, \vartheta \; \mathcal{Q}_n(\vartheta) \\ & \times \int \mathrm{d}\ell \; \ell \; \mathrm{J}_2(\ell\vartheta) \int \mathrm{d}w \; \frac{g(w) p_{\mathrm{l}z}(z)}{a(w) f_k(w)} \frac{\mathrm{d}z}{\mathrm{d}w} \mathcal{P}_{3D}\left(\frac{\ell}{f_k(w)}; w\right) \; . \end{aligned} \tag{6.29}$$

As before, we use the weighted average of $\hat{b}$ and $\hat{r}$ over ℓ, z and ϑ. When measuring $\Upsilon_{\mathrm{gm}}(n)$ and $\Upsilon_{\mathrm{gg}}(n)$ from the data, we can simultaneously fit the models to both signals. In this way we can either

1. fix the cosmology and constrain b and r,
2. fix b and r and constrain the cosmology,
3. or constrain b, r, and the cosmology simultaneously.

The latter is possible by combining galaxy clustering and galaxy-galaxy lensing with a cosmic shear signal, weighted by the same kernel functions $\mathcal{U}_n(\vartheta)$. Since the scope of this work is to proof the concept we will use a fixed cosmology and constrain the galaxy bias b and the cross-correlation coefficient r.

6.3. Data Analysis

We keep the cosmology fixed and measure only the galaxy bias b and the cross-correlation coefficient r using the BOSS LOWZ sample as lenses and photometrically selected galaxies in the RCSLenS as sources.

6.3.1. Data sets

BOSS LOWZ

As lenses we use galaxies from BOSS (Eisenstein et al., 2011), namely the 10th Data Release (Ahn et al., 2014), which have measured spectroscopic redshifts. Of those galaxies we use only the LOWZ sample that consists of luminous red galaxies, photometrically selected to have $0.2 \lesssim z \lesssim 0.4$, which resulted in selecting also galaxies that have a slightly higher or lower spectroscopic redshift. Following the studies by Chuang et al. (2013) and Sánchez et al. (2013), we cut the LOWZ sample with $0.15 \leq z \leq 0.43$. This yields 9102 galaxies within the RCSLenS area from which we select the sources. For the lensing measurements we only use the BOSS galaxies that lie within the BOSS-RCSLenS overlap; however, for the clustering measurement, the whole LOWZ sample is used, which is spread over a much larger area and consists of 218 891 galaxies. In this way we can make use of the much better statistics arising from the larger sample. We will show in Section 6.3.4 that the signals measured for both samples are consistent with each other, which is why this is a valid approach. The BOSS and RCSLenS overlapping area is shown in Fig. 6.3. The summed $p_{\mathrm{l}z}(z)$ derived from spectroscopic redshifts of the lenses can be seen in Fig. 6.4. For the clustering measurements we make use of the weights, Θ, provided by the BOSS collaboration, which account for fibre collisions as explained in Anderson et al. (2014).

RCSLenS

RCSLenS (Hildebrandt et al. in prep.) is an analysis of the original Red Cluster Sequence Survey 2 data (RCS2; Gilbank et al. 2011) using the CFHTLenS pipeline (Hildebrandt et al. 2012; Heymans et al. 2012; Miller et al. 2013; Erben et al. 2013) for reducing the data and creating shape and photometry catalogues. The survey has been carried out using Megacam at CFHT and has only one exposure per band per pointing. It covers roughly 500 deg^2 in the g'-, r'-, i'- and z'-band and an additional 250 deg^2 with three or fewer band coverage. The r'-band is used as the lensing band with a 5σ point source limiting magnitude of $m_{\mathrm{lim}} = 24.3$ and a median seeing of 0.71 arcsec (Gilbank et al., 2011). Galaxy shapes are measured using `lensfit` (Miller et al., 2013). As described in Blake et al. (2015), we use the `lensfit` weights η and the BOSS weights Θ for the lensing analysis. We take both weights in order to use the same weighting scheme in the lensing as well as in the clustering analysis. For selecting source galaxies, we only use the six RCSLenS patches that have four band photometry and sufficient overlap with BOSS. Those are CDE0133, CDE0047, CDE1645, CDE2329, CDE1514, and CDE2143. This leaves us with about 230 deg^2 in area and 3.288.686 source galaxies. As sources we select all galaxies with a `lensfit` weight $\eta > 0$ that are between $r' = 19$ and $r' = 24$. The `BPZ` (Benítez, 2000) estimate of the summed $p_{\mathrm{s}z}(z)$ of the sources is displayed in Fig. 6.4. In order to find the the summed $p_{\mathrm{s}z}(z)$, we add up all individual $p_{\mathrm{s}z}(z)$ estimates of the source galaxies and renormalise.

Furthermore, we are aware that the shear measurements for RCSLenS suffer from a multiplicative as well as an additive bias so that

$$e_{\mathrm{obs}} = (1 + m)e_{\mathrm{true}} + c \, , \tag{6.30}$$

as explained for example in Miller et al. (2013). Here e_{obs} is the observed ellipticity of a galaxy image, e_{true} the intrinsic ellipticity, $1 + m$ the correction factor for the multiplicative bias (m-correction), and c is the correction for the additive bias (c-correction). We correct the measured shapes of galaxies for the multiplicative bias using the factor $(1+m)$ determined for every galaxy (for more details see e.g. Heymans et al. 2012 or Hildebrandt et al. in prep.). We apply the m correction as an ensemble correction in order to avoid correlations between the correction and the intrinsic shape of the galaxy (Miller et al., 2013)

$$\langle\gamma_{\rm t}^{\rm cal}(\vartheta)\rangle = \frac{\langle\gamma_{\rm t}(\vartheta)\rangle}{1+K(\vartheta)} \,, \tag{6.31}$$

where

$$1+K(\vartheta) = \frac{\sum \eta_i \Theta_j (1+m_i)}{\sum \eta_i \Theta_j} \,. \tag{6.32}$$

Here η_i denotes the `lensfit` weight of the ith source galaxy and Θ_j the BOSS weight of the jth lens galaxy. We do not apply an additive c-correction but subtract the $\gamma_{\rm t}$ signal around random points. The number of random points used depends on the patch size and differs between $\sim 100\,000$ and $\sim 180\,000$. The measured signal around random points is consistent with zero on scales below $30-40$ arcmin and rises out to larger scales, where for $\vartheta > 70$ arcmin it can reach an amplitude of a few times 10^{-4} for some patches. We subtract this signal for every patch separately as it would average out when combined from all patches. The signals are shown in Fig. 6.5. The patch with the strongest random signal is CDE0133, which is the smallest in area and thus contributes the least to the total signal. We note that it is not possible to judge if this will influence cosmic shear measurements on this data set, as such studies will make use of the c-correction, which should ideally account for these systematics. For the weighted average source density we find ~ 3.12 galaxies/arcmin^2 when using

$$n_{\rm eff} = \frac{1}{A_{\rm eff}} \frac{\left(\sum \eta_i\right)^2}{\sum (\eta_i)^2} \,, \tag{6.33}$$

as defined in Heymans et al. (2012), where $A_{\rm eff} = 229.55\,\deg^2$ is the total unmasked area. We use this definition to account for the fact that we use the `lensfit` weight in the analysis. The RCSLenS catalogues are also subject to a blinding scheme. In order to avoid confirmation bias, the galaxy ellipticities exist in four versions A, B, C, and D. One of them is the true measured one, whereas the rest have been changed by a small factor as described in Hildebrandt et al. (in prep.) and Kuijken et al. (2015). This analysis has been performed four times using the different ellipticity versions. After the manuscript will be finalised, we will contact Mathias Bartelmann, the external blinder, who will reveal which catalogue is the true one. We will then use the results of the true measured ellipticities only. After “unblinding”, no changes can be applied to the analysis. As we did not “unblind” ourselves already, we will present the results of this analysis for all four columns but only show the plots for the first one. For more information about RCSLenS and the data production process, we refer to Hildebrandt et al. (in prep.).

6.3.2. Mock catalogues

In order to find the covariance of the Υs, we make use of the simulations described in Harnois-Deraps & van Waerbeke (2015). Those have box sizes of $505\,h^{-1}$Mpc, 1536^3 particles each and are on 3072^3 grids, which are projected onto 12288^2 pixels. The light cones are then extracted from those onto 6000^2 pixels grids. The cosmology used is $\Omega_{\rm m,0} = 0.2905$, $\Omega_{\Lambda,0} = 0.7095$, $\sigma_8 = 0.826$, and $H_0 = 68.98\,{\rm km\,s^{-1}Mpc^{-1}}$. The slight difference to the cosmologies we use will

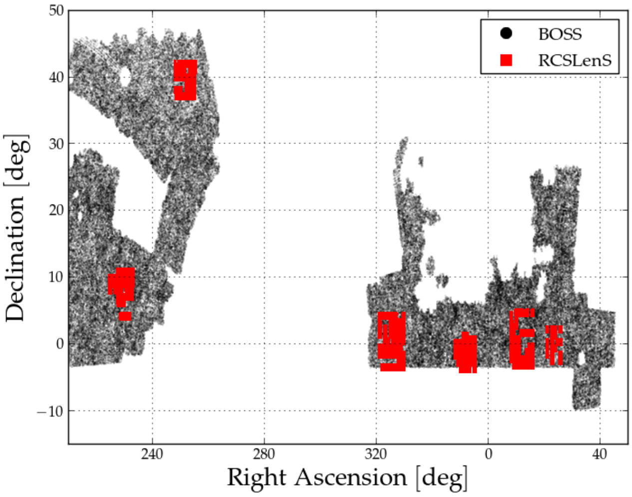

Figure 6.3.: RCSLenS patches that were used, and the galaxies from BOSS. The RCSLenS patches are non-contiguous because of the lack of four-band data, which is needed for photometric redshifts.

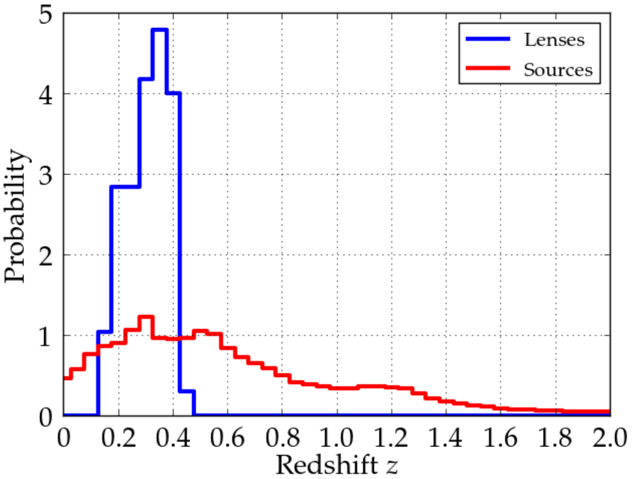

Figure 6.4.: $p_{\mathrm{l}z}(z)$ of lenses (blue) and $p_{\mathrm{s}z}(z)$ of sources (red). For the lenses we use the spectroscopic redshifts to estimate $p_{\mathrm{l}z}(z)$, whereas for the sources we make use of the stacked full $p(z)$ of every source galaxy, which is estimated by the photometric redshift code.

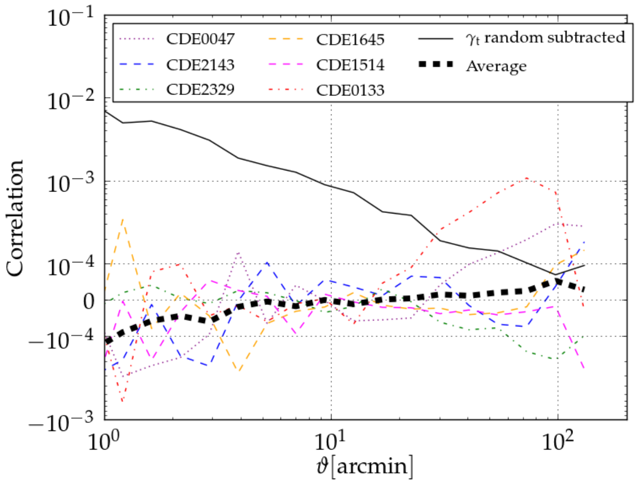

Figure 6.5.: We show the lensing signal around random points. The coloured lines show the signal for every patch, whereas the black dashed line shows the average. Furthermore, we display the measured signal of γ_t around BOSS LOWZ galaxies as the solid black line. The strongest signal corresponds to CDE0133, which is the smallest patch in the area we use, and thus it has the smallest impact on the total signal.

introduce a small systematic error in the covariance, which we will neglect in this study, where very high statistical precision is not the main goal.

Based on these simulations, we use a set of mock catalogues initially created for Choi et al. (in prep.) to match the properties of the RCSLenS sources and the BOSS LOWZ lenses. They specifically match the ellipticity and redshift distributions of RCSLenS and the clustering properties of the LOWZ sample. Those mocks are each $60\,\mathrm{deg}^2$ big. Using six of the mocks, we can create one mock survey, assuming that each of the six RCSLenS patches fits within the $60\,\mathrm{deg}^2$. Whenever the patches are too big, we use as much area as possible and scale the covariance accordingly by using the ratio of the area of the mock patch and the real patch. Furthermore, for the covariance estimation we are forced to use only the BOSS-RCSLenS overlap for the measurements of the clustering signal, whereas for the data we use the whole BOSS area. In order to account for this we rescale the clustering part of the covariance with the ratio of the two areas. Additionally, we set the cross-covariance part to 0, as the BOSS-RCSLenS overlap is just a small fraction of the whole BOSS area. This has been shown to be a valid approach by More et al. (2015), who conduct similar measurements with BOSS and the CFHTLenS catalogues. In the end we have 60 mock surveys, to which we apply the same masks as for the data set. For this we neglect that the mocks assume a flat sky, whereas the original survey data was observed on a sphere. Given the small extend of each patch, the resulting differences are clearly negligible compared to the statistical error of our measurements.

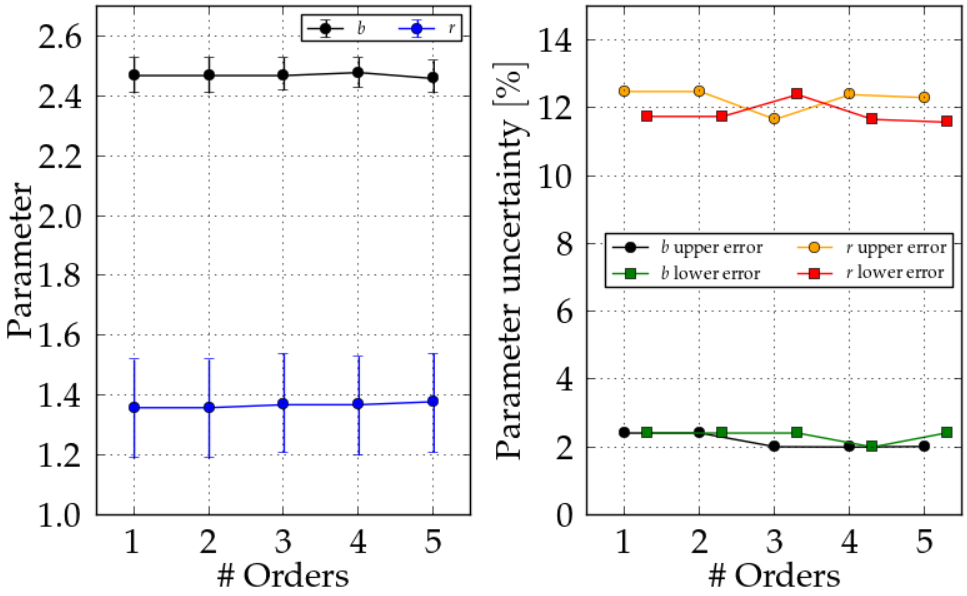

Figure 6.6.: *left:* We present the measured parameter values as a function of the number of used Υ-orders n for b and r. No significant difference in the values is visible, from which we conclude that the data compression is indeed working and only a few orders contain all information of the measured signals. *right:* This graphic shows the parameter uncertainty in per cent for b and r, again as a function of the used number of n. Here, we also do not find a significant difference, which again shows that the data compression of the $\Upsilon(n)$ is working.

6.3.3. Measuring two-point correlations

Before we can determine the $\Upsilon_{\mathrm{ij}}(n)$, we first need to measure the corresponding galaxy-galaxy lensing and galaxy clustering signals. We measure those in two intervals

1. $3' \leq \vartheta \leq 20'$,
2. $20' \leq \vartheta \leq 70'$

in 200 linear bins. As a cross-check we also determine these signals for a larger angular scale in larger logarithmic bins. The 200 linear bins will later be used for determining the Υ. For $\omega(\vartheta)$ we use the Landy-Szalay estimator (Landy & Szalay, 1993).

6.3.4. $\Upsilon_{\mathrm{gm}}(n)$ and $\Upsilon_{\mathrm{gg}}(n)$

We use $\gamma_{\mathrm{t}}(\vartheta)$ and $\omega(\vartheta)$ measured in the 200 linear bins and integrate them using Eq. (6.22) and Eq. (6.23) in order to find $\Upsilon_{\mathrm{gm}}(n)$ and $\Upsilon_{\mathrm{gg}}(n)$. Here we only compute the first three orders. At

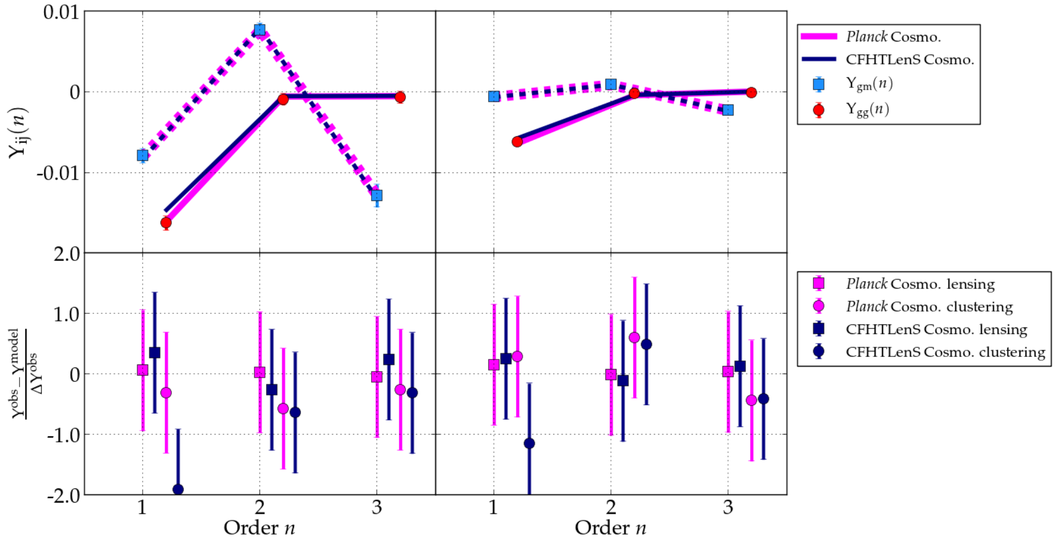

Figure 6.7.: In the top panels, we present the measured Υ_{gm} and Υ_{gg} and the best fit using a *Planck* cosmology or the CFHTLenS cosmology. The dark blue and magenta lines are the connections between the predicted data points using the *Planck* or the CFHTLenS cosmology. In the bottom panels we show the residuals $(\Upsilon^{\mathrm{obs}} - \Upsilon^{\mathrm{model}})/\Delta\Upsilon^{\mathrm{obs}}$. *left:* Measurements for the $3-20$ arcmin interval. *right:* Measurements for the $20-70$ arcmin interval.

Table 6.1.: Parameter estimates for galaxy bias b and cross-correlation coefficient r for the first ellipticity column. In case of the full sample, the second column indicates the cosmology used. For the samples used in Section 6.3.5, it indicates which subsample was used.

scale		b	r
$3' - 20'$	*Planck*	$2.47^{+0.06}_{-0.06}$	$1.37^{+0.15}_{-0.16}$
$3' - 20'$	CFHTLenS	$2.36^{+0.06}_{-0.05}$	$1.48^{+0.17}_{-0.17}$
$20' - 70'$	*Planck*	$2.37^{+0.08}_{-0.08}$	$1.04^{+0.25}_{-0.25}$
$20' - 70'$	CFHTLenS	$2.25^{+0.07}_{-0.08}$	$1.12^{+0.26}_{-0.27}$
$3' - 20'$	$0.15 < z < 0.3$	$2.69^{+0.06}_{-0.06}$	$1.39^{+0.21}_{-0.20}$
$3' - 20'$	$0.3 < z < 0.45$	$2.63^{+0.08}_{-0.08}$	$1.11^{+0.19}_{-0.19}$

the end of our analysis, we tested how the parameter constraints on b and r changed with the number of Υ orders used. We found no significant difference for up to 5 orders and decided to use 3 orders, which yields a sufficient number of data points for our analysis and still benefits from a low-dimensional covariance. The fact that we do not find a decrease of parameter uncertainty with increasing number of orders shows that the first few orders indeed contain all the relevant information, as anticipated before (see Fig. 6.6 for more details). The measured data points for both angular intervals are presented in Fig. 6.7. From the 60 mock realisations, we compute the $\Upsilon_{\rm gm}$ and $\Upsilon_{\rm gg}$ covariance matrix by measuring the signals on each mock survey while taking into account the correction factor from Hartlap, Simon & Schneider (2007). The correlation matrices for all measurements are shown in Fig. 6.8. Additionally, we show the mean signals for $\gamma_{\rm t}$ and ω measured in the mocks together with the real data in Fig. 6.9. The covariance matrix is then used for a maximum likelihood analysis, in which we simultaneously fit theoretical predictions to $\Upsilon_{\rm gm}$ and $\Upsilon_{\rm gg}$ with the galaxy bias b and the cross-correlation coefficient r as free parameters. We compute the predictions from Eq. (6.26) and Eq. (6.29) using the 3D matter power spectrum computed with `nicaea` (Kilbinger et al., 2009), which uses the recipe from Smith et al. (2003). The resulting likelihood contours are displayed in Fig. 6.10. We perform this fit twice using the *Planck* cosmology as well as the one from CFHTLenS, constrained in Heymans et al. (2013), to test for the dependence of the parameters on different cosmologies. The results are presented in Tables 6.1, 6.2, 6.3, and 6.4. For the maximum likelihood analysis we assume a Gaussian likelihood function.

The estimated values for b are slightly higher compared to the findings by Parejko et al. (2013), who determine the bias by fitting their projected clustering signal to HOD populated N-body simulations. Using their best fit model and the corresponding simulations they predict the bias for the LOWZ sample as a function of physical scale. For 3 Mpc, which corresponds to about 11 arcmin at a redshift of 0.3, this corresponds to a bias of about ~ 2.2, whereas for 12 Mpc (~ 45 arcmin) it corresponds to a bias of ~ 2.1. The discrepancy can for example be explained

Table 6.2.: Parameter estimates for galaxy bias b and cross-correlation coefficient r for the second ellipticity column. In case of the full sample, the second column indicates the cosmology used. For the samples used in Section 6.3.5, it indicates which subsample was used.

scale		b	r
$3' - 20'$	*Planck*	$2.47^{+0.06}_{-0.06}$	$1.55^{+0.16}_{-0.16}$
$3' - 20'$	CFHTLenS	$2.36^{+0.06}_{-0.05}$	$1.68^{+0.17}_{-0.17}$
$20' - 70'$	*Planck*	$2.37^{+0.08}_{-0.08}$	$1.17^{+0.25}_{-0.24}$
$20' - 70'$	CFHTLenS	$2.25^{+0.07}_{-0.08}$	$1.26^{+0.27}_{-0.27}$
$3' - 20'$	$0.15 < z < 0.3$	$2.69^{+0.06}_{-0.06}$	$1.58^{+0.20}_{-0.20}$
$3' - 20'$	$0.3 < z < 0.45$	$2.63^{+0.08}_{-0.08}$	$1.26^{+0.19}_{-0.19}$

Table 6.3.: Parameter estimates for galaxy bias b and cross-correlation coefficient r for the third ellipticity column. In case of the full sample, the second column indicates the cosmology used. For the samples used in Section 6.3.5, it indicates which subsample was used.

scale		b	r
$3' - 20'$	*Planck*	$2.47^{+0.06}_{-0.06}$	$1.42^{+0.16}_{-0.16}$
$3' - 20'$	CFHTLenS	$2.36^{+0.06}_{-0.05}$	$1.53^{+0.17}_{-0.17}$
$20' - 70'$	*Planck*	$2.37^{+0.08}_{-0.08}$	$1.08^{+0.25}_{-0.25}$
$20' - 70'$	CFHTLenS	$2.25^{+0.07}_{-0.08}$	$1.16^{+0.27}_{-0.27}$
$3' - 20'$	$0.15 < z < 0.3$	$2.69^{+0.06}_{-0.06}$	$1.45^{+0.20}_{-0.20}$
$3' - 20'$	$0.3 < z < 0.45$	$2.63^{+0.08}_{-0.08}$	$1.15^{+0.19}_{-0.19}$

Table 6.4.: Parameter estimates for galaxy bias b and cross-correlation coefficient r for the fourth ellipticity column. In case of the full sample, the second column indicates the cosmology used. For the samples used in Section 6.3.5, it indicates which subsample was used.

scale		b	r
$3' - 20'$	*Planck*	$2.47^{+0.06}_{-0.06}$	$1.60^{+0.16}_{-0.16}$
$3' - 20'$	CFHTLenS	$2.36^{+0.06}_{-0.05}$	$1.73^{+0.17}_{-0.17}$
$20' - 70'$	*Planck*	$2.37^{+0.08}_{-0.08}$	$1.21^{+0.25}_{-0.25}$
$20' - 70'$	CFHTLenS	$2.25^{+0.07}_{-0.08}$	$1.30^{+0.27}_{-0.27}$
$3' - 20'$	$0.15 < z < 0.3$	$2.69^{+0.06}_{-0.06}$	$1.63^{+0.20}_{-0.20}$
$3' - 20'$	$0.3 < z < 0.45$	$2.64^{+0.08}_{-0.08}$	$1.30^{+0.19}_{-0.19}$

by our approach of averaging over ℓ and z and the corresponding weight functions or by the strong difference in the two approaches of finding the bias. We would also expect r to be closer to unity on the smaller scales interval, where for both cosmologies it is about 3σ away from unity. On large scales, however, we find r to be close to unity. One should note that a measured $r > 1$ is possible, as has been discussed in B10. The values measured for different cosmologies differ by a few percent which is smaller than the parameter uncertainties from statistical error.

In Fig. 6.11 we show the measured signals for $\gamma_{\rm t}(\vartheta)$ and $\omega(\vartheta)$ for the whole sample as well as the two sub-samples from Section 6.3.5. We also scale the expected signals for both with the constrained values of b and r. Apparently, the data is consistent with constant values of b and r and the values for both parameters obtained from the fit to the Υs is consistent with the signals of the traditional correlation functions $\gamma_{\rm t}(\vartheta)$ and $\omega(\vartheta)$.

6.3.5. Sanity check: splitting up the LOWZ sample

As a sanity check we split up the lens sample in two sub-samples with $0.15 < z < 0.3$ and $0.3 < z < 0.43$. We then make the same measurements as before using the *Planck* cosmology and the $\vartheta \in [3', 20']$ interval. This yields two new estimates for b and for r. They are shown in Tables 6.1, 6.2, 6.3, and 6.4. The measured correlation functions are displayed in Fig. 6.11 and the likelihood contours in Fig. 6.10. We find that r becomes smaller for the higher redshift sample. We point out that all these differences are not statistically significant as all estimates are only a few σ away from each other. The measurements of the two sub-samples are consistent with all other measurements within a few σ.

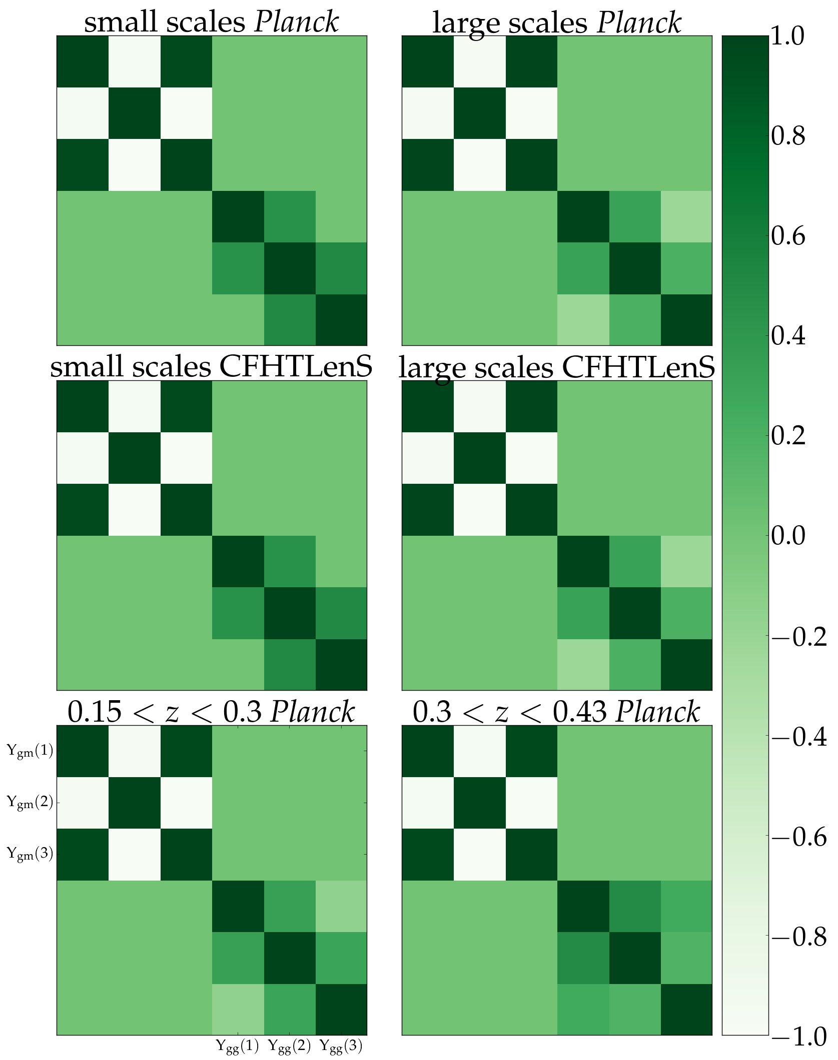

Figure 6.8.: We present the correlation matrices for $\Upsilon_{\rm gm}$ and $\Upsilon_{\rm gg}$ for all measurements. The top left part of the matrices corresponds to galaxy-galaxy lensing, the bottom right to galaxy clustering. The rest are cross-covariance, which we set to 0 as the area for the lensing measurement is only a small fraction of the clustering area, which makes those measurements basically independent. In the order left to right, top to bottom we show the matrix for the $3-20$ arcmin interval and the *Planck* cosmology, the $20-70$ arcmin interval and the *Planck* cosmology, the $3-20$ arcmin interval and the CFHTLenS cosmology, the $20-70$ arcmin interval and the CFHTLenS cosmology, the $3-20$ arcmin interval and the $0.15 < z < 0.3$ sample, and the $3-20$ arcmin interval and the $0.3 < z < 0.45$ sample.

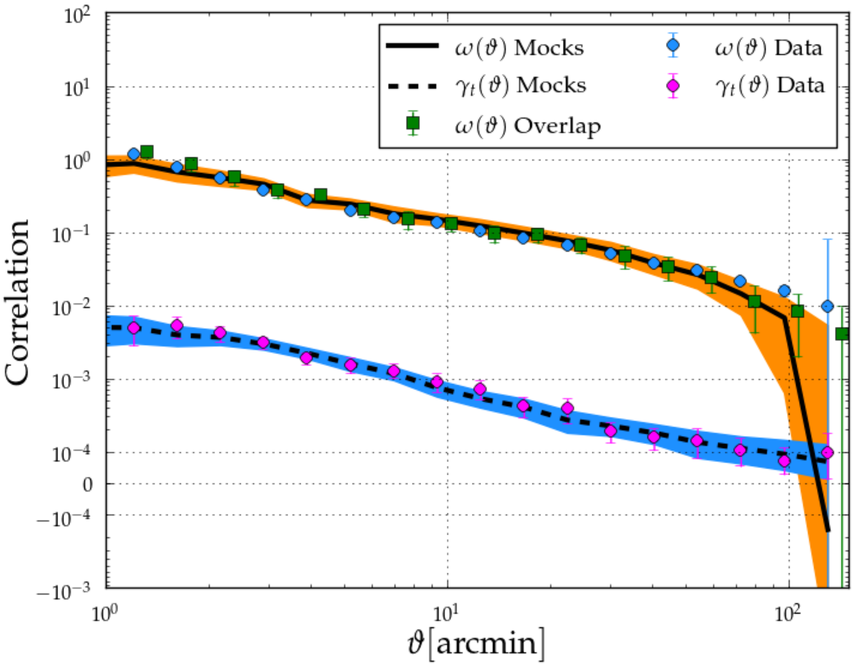

Figure 6.9.: Galaxy clustering and galaxy-galaxy lensing signals in the mocks. The black lines show the mean; spread is indicated by the blue and yellow shaded regions. We also show the measurement from the data as the blue and pink points. They are in good agreement with the mocks. Additionally, the clustering signal measured just for the BOSS-RCSLenS overlap is displayed as the green points. This is consistent with the signal from the whole LOWZ sample.

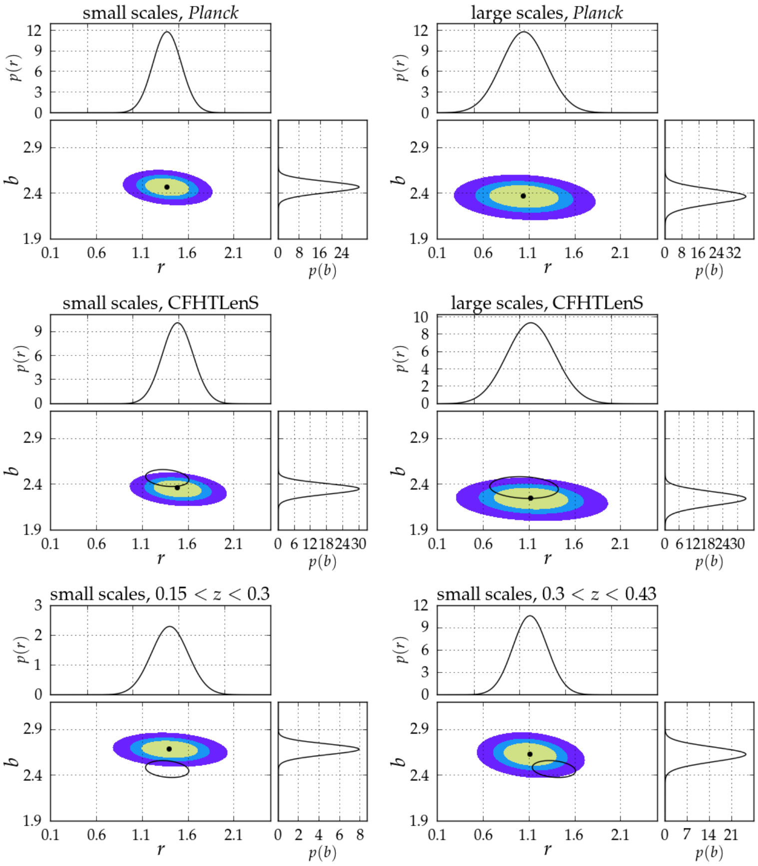

Figure 6.10.: We present the likelihood contours of the different measurements. The black ellipse, if shown, is the 1σ contour of the corresponding measurement with the *Planck* cosmology. *top left:* 1-, 2- and 3-σ likelihood contours of b and r of the fit to the $\Upsilon_{\rm gm}$ and $\Upsilon_{\rm gg}$ for the $3-20$ arcmin interval. We also show the marginalised likelihoods of b and r. *top right:* Likelihood contours for the $20-70$ arcmin interval. *middle left:* Likelihood contours for the $3-20$ arcmin interval and the Heymans et al. (2013) cosmology. *middle right:* Likelihood contours for the $20-70$ arcmin interval and the Heymans et al. (2013) cosmology. *bottom left:* Likelihood contours for the $3-20$ arcmin interval, the *Planck* cosmology and the $0.15 < z < 0.3$ sample. *bottom right:* Likelihood contours for the $3-20$ arcmin interval, the *Planck* cosmology and the $0.3 < z < 0.43$ sample.

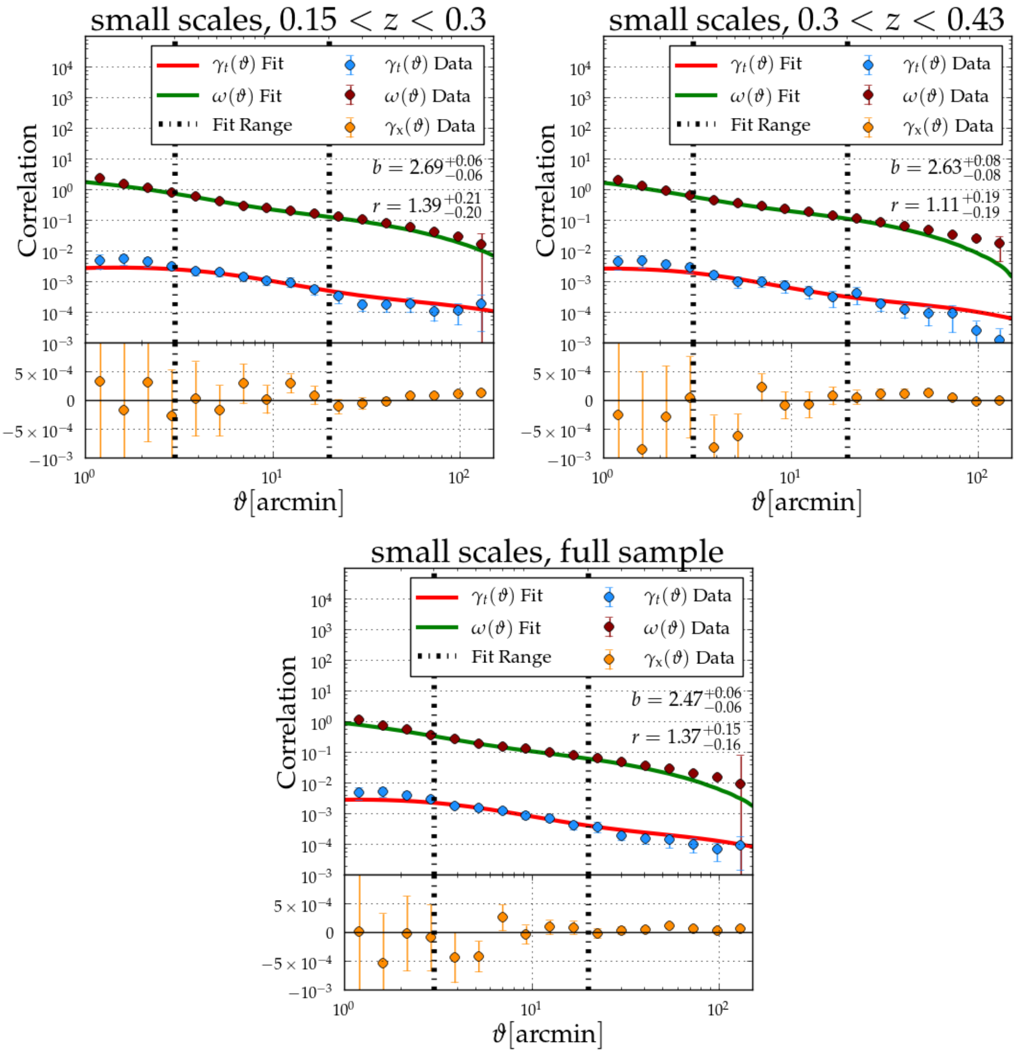

Figure 6.11.: Galaxy clustering and galaxy-galaxy lensing signals and the best fit lines for the $3 - 20$ arcmin interval, the *Planck* cosmology and the two sub samples from the sanity check, as well as the full sample. The best fit lines were fitted to the Υs, not the signals shown here. Within the fitting range, the estimated parameter values for b and r appear to be in excellent agreement with the data. Furthermore, we show the cross-shear γ_{x}, which is consistent with zero.

6.4. Discussion & Outlook

We introduced a new estimator for galaxy-clustering, Υ_{gg}, and for galaxy-galaxy lensing, Υ_{gm}. Those are generalisations of the methods introduced and tested in Baldauf et al. (2010) and Mandelbaum et al. (2013), respectively. The estimators are essentially a discretisation of the signal, which leads to great data compression and a lower dimensional covariance, while still eliminating small scale influences. Especially, the low dimension of the data covariance makes life easy when computing it since the number of mock realisations needed to find a good estimate of the covariance increases with the number of data points. We applied this method to data using the BOSS LOWZ sample as lenses and galaxies from the RCSLenS as sources. While fixing the cosmology, we performed a simultaneous fit to Υ_{gg} and Υ_{gm} with b and r as free parameters. For different angular scales as well as different assumed cosmologies, we find b slightly higher than the findings of Parejko et al. (2013), which is probably caused by our estimate being an average over many scales. On small angular scales, we find r to be considerably greater than unity, which is not expected at these scales, where r is usually found to converge to 1. On larger scales, however, we find r close to unity. Given already measured values for b and r, this method can even be used for cosmological studies. In these studies, it will be necessary to find out how many orders of Υ are sufficient to extract all cosmological information from the signal. As in this work, it was not possible to do so as all information is already contained in the first few orders, due to our simplified bias models. This might change in a cosmological analysis, where the data models will increase in complexity.

All things considered, the new estimators appear to be promising tools for large-scale structure studies, especially given their advantageous abilities concerning data compression and the dimension of the data covariance.

For this work we made use of the correlation codes `athena`[4] *and* `swot`[5] *(Coupon et al., 2012).*

---

[4] `http://www.cosmostat.org/athena.html`

[5] `https://github.com/jcoupon/swot`

Bibliography

Ahn C. P. et al., 2014, ApJS, 211, 17

Anderson L. et al., 2014, MNRAS, 439, 83

Bacon D. J., Refregier A. R., Ellis R. S., 2000, MNRAS, 318, 625

Baldauf T., Smith R. E., Seljak U., Mandelbaum R., 2010, Phys. Rev. D, 81, 063531

Bartelmann M., Schneider P., 2001, PhR, 340, 291

Benítez N., 2000, ApJ, 536, 571

Blake C. et al., 2012, MNRAS, 425, 405

Blake C. et al., 2015, ArXiv e-prints: 1507.03086

Chuang C.-H. et al., 2013, ArXiv e-prints: 1312.4889

Coupon J. et al., 2015, ArXiv e-prints: 1502.02867

Coupon J. et al., 2012, A&A, 542, A5

Eisenstein D. J. et al., 2011, AJ, 142, 72

Erben T. et al., 2013, MNRAS, 433, 2545

Eriksen M., Gaztanaga E., 2014, ArXiv e-prints: 1412.2208

Gilbank D. G., Gladders M. D., Yee H. K. C., Hsieh B. C., 2011, AJ, 141, 94

Guzik J., Seljak U., 2001, MNRAS, 321, 439

Harnois-Deraps J., van Waerbeke L., 2015, MNRAS, 450, 2857

Hartlap J., Simon P., Schneider P., 2007, A&A, 464, 399

Heymans C. et al., 2013, MNRAS, 432, 2433

Heymans C. et al., 2012, MNRAS, 427, 146

Hildebrandt H. et al., 2012, MNRAS, 421, 2355

Hinshaw G. et al., 2013, ApJS, 208, 19

Hoekstra H., van Waerbeke L., Gladders M. D., Mellier Y., Yee H. K. C., 2002a, ApJ, 577, 604

Hoekstra H., Yee H. K. C., Gladders M. D., Barrientos L. F., Hall P. B., Infante L., 2002b, ApJ, 572, 55

Ivezic Z. et al., 2008, ArXiv e-prints: 0805.2366

Kaiser N., 1984, ApJ, 284, L9

Kaiser N., 1992, ApJ, 388, 272

Kilbinger M. et al., 2009, A&A, 497, 677

Kitching T. D. et al., 2012, MNRAS, 423, 3163

Kuijken K. et al., 2015, ArXiv e-prints: 1507.00738

Landy S. D., Szalay A. S., 1993, ApJ, 412, 64

Laureijs R. et al., 2011, ArXiv e-prints: 1110.3193

Leauthaud A., Tinker J., Behroozi P. S., Busha M. T., Wechsler R. H., 2011, ApJ, 738, 45

Mandelbaum R. et al., 2015, MNRAS, 450, 2963

Mandelbaum R., Slosar A., Baldauf T., Seljak U., Hirata C. M., Nakajima R., Reyes R., Smith R. E., 2013, MNRAS, 432, 1544

Mantz A. B., Allen S. W., Morris R. G., Rapetti D. A., Applegate D. E., Kelly P. L., von der Linden A., Schmidt R. W., 2014, MNRAS, 440, 2077

Miller L. et al., 2013, MNRAS, 429, 2858

More S., Miyatake H., Mandelbaum R., Takada M., Spergel D. N., Brownstein J. R., Schneider D. P., 2015, ApJ, 806, 2

Parejko J. K. et al., 2013, MNRAS, 429, 98

Perlmutter S. et al., 1999, ApJ, 517, 565

Planck Collaboration et al., 2015, ArXiv e-prints: 1502.01589

Riess A. G. et al., 1998, AJ, 116, 1009

Sánchez A. G. et al., 2013, MNRAS, 433, 1202

Schneider P., 1996, MNRAS, 283, 837

Schneider P., Eifler T., Krause E., 2010, A&A, 520, A116

Schneider P., van Waerbeke L., Jain B., Kruse G., 1998, MNRAS, 296, 873

Schrabback T. et al., 2010, A&A, 516, A63

Smith R. E. et al., 2003, MNRAS, 341, 1311

Spergel D. et al., 2015, ArXiv e-prints: 1503.03757

van Uitert E., Hoekstra H., Schrabback T., Gilbank D. G., Gladders M. D., Yee H. K. C., 2012, A&A, 545, A71

van Uitert E., Hoekstra H., Velander M., Gilbank D. G., Gladders M. D., Yee H. K. C., 2011, A&A, 534, A14

Van Waerbeke L. et al., 2001, A&A, 374, 757

Velander M. et al., 2014, MNRAS, 437, 2111

Vikhlinin A. et al., 2009, ApJ, 692, 1060

CHAPTER 7

Conclusions & Outlook

After a proper introduction to modern cosmology, weak gravitational lensing and galaxy clusters we investigated a few aspects of observational cosmology in this work.

In Chapter 4, we introduced the problem of CCD crosstalk in CCD cameras, which are now used at every professional telescope in the world. This re-localisation of flux between different pixels or even chips is a serious problem for photometric measurements. It needs to be corrected for. We discussed the case of OmegaCAM at the VST, where several of the 32 chips interchange flux and suggested a correction scheme. This scheme is capable of correcting the flux in most of the pixels involved in the crosstalk interaction and flags the remaining as not usable for object detection and subsequent measurements. The approach has been implemented by the author and is now included in the THELI data reduction pipeline, which is part of the KiDS pipeline described in Kuijken et al. (2015). As cameras will become even larger, more chips will be used and consequently more electronics. The problem of crosstalk will remain and become more important. Thus it is important to have fully developed and tested tools in place to build on for future surveys. This is as important for the kind of crosstalk discussed in this work as well as other kinds.

Chapter 5 is concerned with high-redshift galaxy clusters that are possibly among the most massive in the Universe. By assuming a certain cosmology, one can predict the largest galaxy cluster mass as a function of redshift. So by finding one ore more clusters that are more massive, we can conduct a relatively easy cosmology test. First, however, we need to find suitable massive cluster candidates. We conducted such a search by cross-correlating X-ray data from RASS and optical data from the SDSS. For this we specifically searched for one or more red galaxies that have a photometric redshift in the SDSS of $0.6 \lesssim z \lesssim 0.9$ and are within $50''$ of a source from the RASS faint source catalogue. The most promising candidates were then observed with the LBT and the WHT in the optical and the possibly most massive or highest redshift ones with CARMA in the radio. From the optical data we confirmed or rejected candidates and estimated photometric redshifts and richness and for a sub-sample also spectroscopic redshifts. Using the Redshift information and a scaling relation we measured Y_{SZ} from the CARMA data and used it to find M_{500}. For the clusters that have mass estimates, we can conduct a cosmology test suggested in Mortonson, Hu & Huterer (2011). We found no tension with ΛCDM for single cluster masses. Furthermore, we could identify many interesting high-redshift galaxy clusters, that for example show strong lensing features or are suspects for cool cores. For some of these objects, weak lensing and X-ray studies are in preparation. A possible extension to this study would be to test if the whole sample is in tension with the standard cosmology and not only single clusters. Additionally, it is possible to run a similar search in the southern hemisphere once the catalogues of the next generation surveys like ATLAS, KiDS, or DES are public.

After using galaxy clusters as a cosmology probe in Chapter 5, we went on to large scale structure probes as tools in cosmology in Chapter 6. Those tools are for example two-point correlations of different observables. An important one is the shear-shear correlation, or cosmic shear, which can be used to recover information of the dark matter distribution. Although a promising probe, it requires very careful data handling and can suffer from strong systematics. Instead of using cosmic shear, we introduced new estimators for galaxy clustering and galaxy-galaxy lensing that, when combined, contain the same information as cosmic shear, but have different, if not smaller, systematics. These new estimators, $\Upsilon_{\mathrm{gm}}(n)$ and $\Upsilon_{\mathrm{gg}}(n)$, are generalisations of a method introduced in Baldauf et al. (2010) and are based on the aperture mass formalism. The Υs are an integrated measure, which effectively discretises the signals. Due to the discretisation, we achieve great data compression, which, depending on the measurements, can reduce the size of the final data vector by a factor of ~ 5 or more. This also helps in determining the data covariance, which is needed for parameter estimates. Furthermore, we can keep the beneficial properties of the Baldauf et al. (2010) estimators that eliminate small scale influences in the signal. As a proof of concept we apply the new estimators to data from BOSS for the lenses and from RCSLenS for the sources and constrain the galaxy bias b and the cross-correlation coefficient r. The results are in rough agreement with earlier studies. These new estimators can also be used for constraining cosmological parameters and could for example be applied to the Kilo Degree Survey or Euclid.

To summarise, we presented a technical problem and a correction for it as well as two of the many ways to do cosmology. Galaxy clusters as cosmological tools will become more and more important within the next few years. As already mentioned, it will become easier to find massive high-redshift clusters in the southern hemisphere, as new wide area surveys will become public soon. Furthermore, the *eRosita* satellite will map the whole sky in the X-ray, which will help to find many more clusters and will allow a similar search for high-redshift ones as has been done in this work. Combining it with KiDS or DES, it might even be possible to push this to higher redshifts. Also, the large scale structure probes will find even more interest in the future. Especially the combination of clustering and lensing is a promising approach. Ideal testing grounds for these methods are the next generation lensing surveys like KiDS or DES. These surveys will most likely not revolutionise cosmology, but are in general a great preparation for the even larger surveys like LSST and *Euclid*, which will actually have the statistical power and a sufficient data quality to constrain the dark energy equation of state and shed some light onto the true nature of dark energy.

Bibliography

Baldauf T., Smith R. E., Seljak U., Mandelbaum R., 2010, Phys. Rev. D, 81, 063531

Kuijken K. et al., 2015, ArXiv e-prints: 1507.00738

Mortonson M. J., Hu W., Huterer D., 2011, Phys. Rev. D, 83, 023015

Danksagungen

Bei den folgenden Personen und Institutionen möchte ich mich für ihre Unterstützung beim Erstellen dieser Arbeit bedanken:

- bei Peter, der das alles hier erst ermöglicht hat
- bei allen Mitgliedern meines Prüfungskomitees
- bei der IMPRS for Astronomy and Astrophysics und dem TRR 33 -The Dark Universe der DFG, ohne deren Finanzierung meine Promotion nicht möglich gewesen wäre
- bei Thomas, Tim und Hendrik
- bei Chris, Martin, Doug und Reiko
- bei Ellen
- bei Sandra, Alberto, Dominik und allen anderen Freunden und Kollegen im AIfA, die mir im Laufe der letzten drei Jahre geholfen haben
- bei allen Menschen mit denen ich auch außerhalb des AIfA in diversen Kollaborationen zusammen gearbeitet habe
- bei Kerstin
- bei meiner Familie
- und zu guter Letzt natürlich bei Caro

CHAPTER A

Summary

Chapter 1: Cosmology

In this chapter, we introduce the reader to the basic concepts of cosmological physics. We start at Einstein's theory of general relativity and the homogeneous and isotropic solutions of Einstein's field equation, that can be used to describe the Universe on large scales. Furthermore, we introduce the concept of distances in expanding cosmologies and describe the thermal history of the Universe. At the end of the chapter, we summarise the cosmological standard model and give a brief description of structure formation in the Universe.

Chapter 2: Gravitational Lensing

Chapter 2 describes the basic concepts of gravitational lensing, a major tool for cosmology. We derive the lens equation and introduce the concepts of shear, convergence and magnification as well as strong-, weak-, and micro lensing. Furthermore, we summarise the many applications of gravitational lensing within and outside cosmology.

Chapter 3: Clusters of Galaxies

Clusters of galaxies are important parts of our Universe and subject to many cosmological studies. As such, their composition as well as several ways of detecting them are described in this chapter. Additionally, we introduce different concepts of estimating the masses of galaxy clusters and two approaches to use clusters as tools for cosmology.

Chapter 4: Correcting for CCD-Crosstalk in OmegaCAM@VST

Chapter 4 is concerned with a correction for the CCD crosstalk in OmegaCAM at the VST. In the beginning, we introduce the concepts of CCD cameras and crosstalk. We then describe the crosstalk between three different chips observed at OmegaCAM. This is followed by explaining the suggested approach for correction and a description of its implementation.

Chapter 5: Optical & Sunyaev-Zel'dovich Observations of a New Sample of Distant Rich Galaxy Clusters in the ROSAT All Sky Survey

As mentioned in Chapter 3, massive high redshift galaxy clusters provide an interesting test for cosmology. This chapter, which has been published in *Monthly Notices of the Royal Astronomical Society*, describes the search for those massive clusters. By combining X-ray data from the *ROSAT* All Sky Survey and optical data from the Sloan Digital Sky Survey, we create a list of rich cluster candidates that have a suspected redshift of $0.6 \leq z \leq 0.9$. Using follow-up observations in the optical, we confirm 44 new galaxy clusters, estimate their red sequence redshifts and their richness. For a sub sample of 21 clusters, we use radio observations from the Combined Array for Research in Millimeter Astronomy in order to detect the SZ signal. We detect 11 of those and estimate their mass M_{200}. Using these mass estimates as well as some already known masses, we check for tension with the cosmological standard model and find none.

Chapter 6: A new Estimator for Galaxy-Matter Correlations

We introduce new discrete estimators for galaxy-galaxy lensing and galaxy clustering within the aperture mass formalism. Those estimators provide great data compression and thus lead to a low dimensional data covariance. We test them by measuring the galaxy bias b and the cross-correlation coefficient r for BOSS LOWZ galaxies using lensing data from RCSLenS.

Chapter 7: Conclusions & Outlook

In this chapter we briefly summarise the most important scientific results of this thesis and give a brief outlook.